Transport and Tunneling Studies of Oxide Superconductors

by

Gabriel Briceño

B.S. (University of California at Los Angeles) 1985
M.S. (University of California at Berkeley) 1988

A dissertation submitted in partial satisfaction of the requirements for the degree of

DOCTOR OF PHILOSOPHY

in

PHYSICS

in the

GRADUATE DIVISION

of the

UNIVERSITY of CALIFORNIA at BERKELEY

Committee in charge:

Professor Alex Zettl, Chair
Professor Marvin L. Cohen
Professor Neil Bartlett

1994

The dissertation of Gabriel Briceño is approved:

Alex Zettl 3/2/94
Chair Date

Marvin L. Cohen 3/8/94
Date

Neil Bartlett 3/29/94
Date

University of California at Berkeley

1994

Transport and Tunneling Studies of Oxide Superconductors

Copyright 1994

by

Gabriel Briceño

Abstract

Transport and Tunneling Studies of Oxide Superconductors.

by

Gabriel Briceño

Doctor of Philosophy in Physics

University of California at Berkeley

Professor Alex Zettl, Chair

This thesis work consists mainly of using tunneling and transport measurement techniques to examine the physical properties of the high T_c oxide superconducting material $Bi_2Sr_2CaCu_2O_8$. In an effort to probe the underlying superconducting mechanism in this material, I conducted studies to determine its tunneling density of states, mobility and charge carrier density, sign of the charge carrier, anisotropic magnetoresistance and thermal magnetoconductivity. The purpose of this research has been three-fold. First, I have set out to measure fundamental superconducting parameters of this high T_c oxide, such as the energy gap and electron-phonon coupling strength. Second, I have attempted to characterize the normal state by measuring basic electron and phonon transport properties. Third, I have investigated how the novel magnetic properties of these material are manifested in its magnetotransport characteristics.

Alex Zettl

To María, Rose and Gabrielito with love

List of Figures v

Acknowledgments vii

Vita ix

Chapter 1 Introduction 1

1.1 General Introduction 1

1.2 $Bi_2Sr_2CaCu_2O_8$ crystal structure and preparation. 4

Chapter 2 Energy Gap Anisotropy 8

2.1 Introduction 8

2.2 Tunneling apparatus and technique 12

2.3 Experiment and analysis 14

Chapter 3 Hall Resistance and Mobility. .....

3.1 Introduction 28

3.2 Hall effect technique 29

3.3 Resistivity and Hall coefficient 33

Chapter 4 c-axis Magnetoresistance 44

4.1 Introduction 44

4.2 c-axis magnetoresistance with H||c 47

4.3 c-axis magnetoresistance with H^c. 53

Chapter 5 Thermal Magnetoconductivity 62

5.1 Introduction 62

5.2 Thermal conductivity of $Bi_2Sr_2CaCu_2O_8$ in the mixed state 64

Appendix A 80

List of Figures

Figure 1.1 Crystal structure of the BSCCO family 3

Figure 1.2 Annealing cycles for $Bi_2Sr_2CaCu_2O_8$ 5

Figure 2.1 Ideal tunneling I-V characteristics 11

Figure 2.2 Differential screw tunneling probe 13

Figure 2.3 Current bridge schematics 15

Figure 2.4 SIN tunneling into ab-plane of $Bi_2Sr_2CaCu_2O_8$ 18

Figure 2.5 Temperature dependence of Δ_{ab} in $Bi_2Sr_2CaCu_2O_8$ 19

Figure 2.6 SIS tunneling along ab-plane in $Bi_2Sr_2CaCu_2O_8$ 20

Figure 2.7 SIS c-axis into ab-plane tunneling in $Bi_2Sr_2CaCu_2O_8$ 22

Figure 2.8 SIN tunneling into the c-axis of $Bi_2Sr_2CaCu_2O_8$ 24

Figure 3.1 Hall effect current source schematics 31

Figure 3.2 Block diagram of Hall effect setup 32

Figure 3.3 $R_H(T)$and $\rho_{ab}(T)$ for ab-plane of $Bi_2Sr_2CaCu_2O_8$ 34

Figure 3.4 Linear fits of $1/R_H$ vs. T 37

Figure 3.5 μ_H for ab-plane of $Bi_2Sr_2CaCu_2O_8$ 39

Figure 4.1 Resistive transition $\rho_c(T, \mathbf{H}\|\mathbf{c})$ of $Bi_2Sr_2CaCu_2O_8$ 48

Figure 4.2 Theoretical fitts to data of Fig. 4.1 51

Figure 4.3 Resistive transition $\rho_c(T, \mathbf{H}\perp\mathbf{c})$ of $Bi_2Sr_2CaCu_2O_8$ 54

Figure 4.4 Current dependence of the resistive transition $\rho_c(T, \mathbf{H}\perp\mathbf{c})$ 55

Figure 4.5 c-axis I-V characteristics for $\mathbf{H}\perp\mathbf{c}$ 57

Figure 5.1 $\kappa_{ab}(T)$ and $\rho_{ab}(T)$ of $Bi_2Sr_2CaCu_2O_8$ in H=0 66

Figure 5.2 Theoretical fit of $\kappa_{ab}(T)$ 69

Figure 5.3 $\kappa_{ab}(T)$ of $Bi_2Sr_2CaCu_2O_8$ in $\mathbf{H}\|\mathbf{c}$ and $\mathbf{H}\perp\mathbf{c}$ 71

Figure 5.4 Magnetic field dependence of κ_{ab} for $\mathbf{H}\perp\mathbf{c}$ 72

Figure 5.5 Experimental and theoretical fits to $\kappa_{ab}(\mathbf{H}\|\mathbf{c})$ 74

Figure 5.6 Electron and phonon contributions to $\kappa_{ab}(T)$ below T_c.....76

Acknowledgments

I would like to acknowledge the help and support that I have received throughout my career. First I thank my parents and my aunt Bruny who always encourage me to reach to the top of any discipline I wanted to pursue. Next I acknowledge my wife María for her love, patience and support.

I would like to thank Professor Alex Zettl for giving me the opportunity to work in his group. Alex has been more than a thesis advisor to me, he has been a friend and a role model that has shaped my career. I also thank Professor Marvin Cohen who, as a collaborator, helped to interpret our experimental results, and as a professor provided me with a great teaching style to follow.

The work described in this thesis would not have been completed without the collaboration with others. Mike Crommie introduced me to the world of high temperature superconductors by teaching me how to perform tunneling density of states measurements. We later on collaborated in the measurement of magnetoresistance in the same materials. He was always there to discuss and show me how to experimentally obtain various fundamental parameters in this material. Mike Hundley taught me the ac-five-probe Hall effect technique. Phil Parilla showed me the way into the Macintosh computer world, but it was Bill Vareka who has been a great computer advisor, for which I will always thank him. Xiao-Dong Xiang implemented a great number of new experimental techniques to our lab, it seems that no experiment is impossible to him. X-D is a great friend and I always enjoyed working with him. I also want to thank Brian Burk always reminding me that we should pay attention to the smallest detail in order for an experiment to work. Nassreen Chopra, Mike Fuhrer, Phil Collins, Jim Hone, Ian Parker, Jian Gou Hou, Storrs Hoen, Bill Creager and Angelika Behrooz made the lab a pleasant environment to work in.

I thank professor Dick Packard for making the transition from UCLA to Cal possible. I enjoyed working in his group, but Mike Crommie talked me into joining the Zettl group.

Finally I acknowledge the Ford Foundation for providing financial support during 1991-1992. They are making a difference by providing minorities with an opportunity to develop their potential to its maximum.

Vita

February 23, 1960	Born in Tizimín,Yucatán, México
April 1981 to June 1985	B.S. in Physics and Mathematics at the U. of California at Los Angeles
August 1985 to May 1988	M.S. in Physics at the U. of California at Berkeley
August 1985 to May 1994	Teaching and research assistant, Department of Physics, U. of California at Berkeley

Publications

1. A. Zettl, A. Behrooz, G. Briceño, W.N.Creager, M.F Crommie, S. Hoen and P. Pinsukanjana. Anisotropic transport in Y-Ba-Cu-O and Bi-Sr-Ca-Cu-O. In Mechanisms of High Temperature Superconductivity, H. Kamimura and A. Oshiyama, eds. (Spring Verlag, NewYork, 1988) P. 249.

2. G. Briceño and A. Zettl. Tunneling spectroscopy in $Bi_2Sr_2CaCu_2O_8$: is the energy gap anisotropic? Solid State Communications 70, 1055 (1989).

3. G. Briceño and A. Zettl. Variable Hall coefficient in $Bi_2Sr_2CaCu_2O_{8-x}$ across the metal-insulator transition. Phys. Rev. B40, 11352 (1989).

4. M.F. Crommie, G. Briceño and A. Zettl. Transport and tunneling in $Bi_2Sr_2CaCu_2O_{8-x}$. Physica C162-164, 1397 (1989).

5. G. Briceño, M.F. Crommie and A. Zettl. Giant out-of-plane magnetoresistance in Bi-Sr-Ca-Cu-O: A new dissipation mechanism in copper-oxide superconductors? Phys. Rev. Lett. 66, 2164 (1991).

6. X.-D. Xiang, J.G. Hou, G. Briceño, W.A. Vareka, R. Mostovoy, A. Zettl, Vincent H. Crespi, Marvin L. Cohen. Synthesis and Electronic Transport of Single Crystal K_3C_{60}. Science 256, 1190 (1992).

7. M.F. Crommie, G. Briceño and A. Zettl. In-plane vortex-lattice depinning in a layered superconductor. Phys. Rev. B. 45, 13148 (1992).

Vita

February 23, 1960	Born in Tizimín,Yucatán, México
April 1981 to June 1985	B.S. in Physics and Mathematics at the U. of California at Los Angeles
August 1985 to May 1988	M.S. in Physics at the U. of ICalifornia at Berkeley
August 1985 to May 1994	Teaching and research assistant, Department of Physics, U. of California at Berkeley

Publications

1. A. Zettl, A. Behrooz, G. Briceño, W.N.Creager, M.F Crommie, S. Hoen and P. Pinsukanjana. Anisotropic transport in Y-Ba-Cu-O and Bi-Sr-Ca-Cu-O. In Mechanisms of High Temperature Superconductivity, H. Kamimura and A. Oshiyama, eds. (Spring Verlag, NewYork, 1988) P. 249.

2. G. Briceño and A. Zettl. Tunneling spectroscopy in $Bi_2Sr_2CaCu_2O_8$: is the energy gap anisotropic? Solid State Communications 70, 1055 (1989).

3. G. Briceño and A. Zettl. Variable Hall coefficient in $Bi_2Sr_2CaCu_2O_{8-x}$ across the metal-insulator transition. Phys. Rev. B40, 11352 (1989).

4. M.F. Crommie, G. Briceño and A. Zettl. Transport and tunneling in $Bi_2Sr_2CaCu_2O_{8-x}$. Physica C162-164, 1397 (1989).

5. G. Briceño, M.F. Crommie and A. Zettl. Giant out-of-plane magnetoresistance in Bi-Sr-Ca-Cu-O: A new dissipation mechanism in copper-oxide superconductors? Phys. Rev. Lett. 66, 2164 (1991).

6. X.-D. Xiang, J.G. Hou, G. Briceño, W.A. Vareka, R. Mostovoy, A. Zettl, Vincent H. Crespi, Marvin L. Cohen. Synthesis and Electronic Transport of Single Crystal K_3C_{60}. Science 256, 1190 (1992).

7. M.F. Crommie, G. Briceño and A. Zettl. In-plane vortex-lattice depinning in a layered superconductor. Phys. Rev. B. 45, 13148 (1992).

8. Q.H Lam, C.D. Jeffries, A. Behrooz, G. Briceño and A. Zettl. The complex permeability and harmonic generation of a $Bi_2Sr_2CaCu_2O_{8-y}$ crystal: measurements and models. Journal of magnetism and magnetic materials 115, 197 (1992).

9. J.G. Hou, Vincent H. Crespi, X.-D. Xiang, W.A. Vareka, G. Briceño, A. Zettl, Marvin L. Cohen. Determination of Superconducting and Normal State Parameters of Single Crystal K_3C_{60}. Solid State Communications 86, 643 (1993).

10. G. Briceño, M.F. Crommie and A. Zettl. Out of plane current trransport in $Bi_2Sr_2CaCu_2O_8$ in the mixed state. Physica C 204, 389 (1993).

11. S.K. Gupta, P. Berdahl, R.E. Russo, G. Briceño and A. Zettl. Pulse I-V characteristics measurement to study the dissipation mechanism in epitaxial $YBa_2Cu_3O_x$ in thin films at high current densities. Physica C 206, 335 (1993).

Chapter 1

Introduction

1.1 General Introduction.

Research into superconductivity has been going on since 1911 when H. Kamerlingh Onnes[1] discovered tha. the resistance of Hg discontinuously disappeared at 4.2K. Other single element metals have also been found to superconduct, with Nb exhibiting the highest transition temperature (T_c=9.5K). Many alloys, including the interesting binary metal-metalloid with a cubic A15 structure, such as V_3Si, Nb_3Sn, and Nb_3Ge, also exhibit superconducticity. The highest T_c known in the 1970's was a member of this family (Nb_3Ge with T_c=23.2 K). However, a new family of superconductors, known as High Temperature SuperConductors (HTSC),[2] was discovered in 198[illegible] A member of this new class of superconductors has the highest transition temperature up to date (a Hg-based cuprate with T_c~135K, and a T_c~164K under externally applied pressure).[3]

In 1933, the discovery of perfect diamagnetism in a superconductor by W. Meissner and R. Ochsenfeld showed that superconductivity is a reversible thermodynamic phenomenon. This discovery induced Fritz and Heinz London to the development of the phenomenological two-fluid model[4] that explained the diamagnetism in terms of surface currents that only allowed the magnetic field to penetrate a distance λ. In 1953 A. B. Pippard, based on the empirical dependence of λ on the mean free path of the electrons, extended the London model to a nonlocal phenomenological theory,[5] in which the current density at a point depended on the integral of the vector potential over a region surrounding the point. It was not until 1957 that a microscopic theory of superconductivity was proposed by J. Bardeen, L. N. Cooper and J. R. Schieffer[6] (the

so-called BCS theory). The BCS theory, with the extensions of Eliashberg[7] and McMillan[8] to include strong coupling, has been very successful in explaining the properties of what are known as conventional superconductors (e.g. single element and A15 superconductors). However, many properties of the HTSC, such as tunneling and photoemission, have eluded an explanation within the BCS theory. Other theories with new mechanisms or modifications of the BCS theory (e.g., hole superconductivity[9]) have been proposed to explain the properties of the HTSC; however, no consensus has been reached yet.

The HTSC's are believed to owe their superconductivity to the presence of CuO_2 sheets, common to the structure of all these materials. These compounds are of a layered nature with one or several CuO_2 sheets per unit cell separated from each other by a layer of a single element, usually an alkaline earth or a lanthanide; the sets of CuO_2 sheets are in turn separated by one or more different atomic layers, usually oxides. The layered nature of the HTSC gives rise to anisotropy between their in-plane and out-of-plane properties. We have studied this anisotropy by transport and tunneling measurements, which allowed us to carefully probe its effect in the normal and superconducting properties of the HTSC.

In the rest of this chapter I will discuss structural properties and the crystal growing technique of a particular member of the HTSC: $Bi_2Sr_2CaCu_2O_8$. This HTSC compound was the subject of this research. I will continue, in chapter 2, by discussing the anisotropic tunneling density of states of this compound in the superconducting state. In chapter 3 I will discuss one of the normal state properties of this compound: its Hall resistance. Chapter 4 will be devoted to the investigation of the c-axis resistivity of $Bi_2Sr_2CaCu_2O_8$ in the presence of magnetic field, and its dependence on the field orientation with respect to the c-axis. Finally, in chapter 5, I will present experimental measurements of the thermal conductivity along the ab-plane in the normal and the superconducting states, with and without a magnetic field oriented parallel or

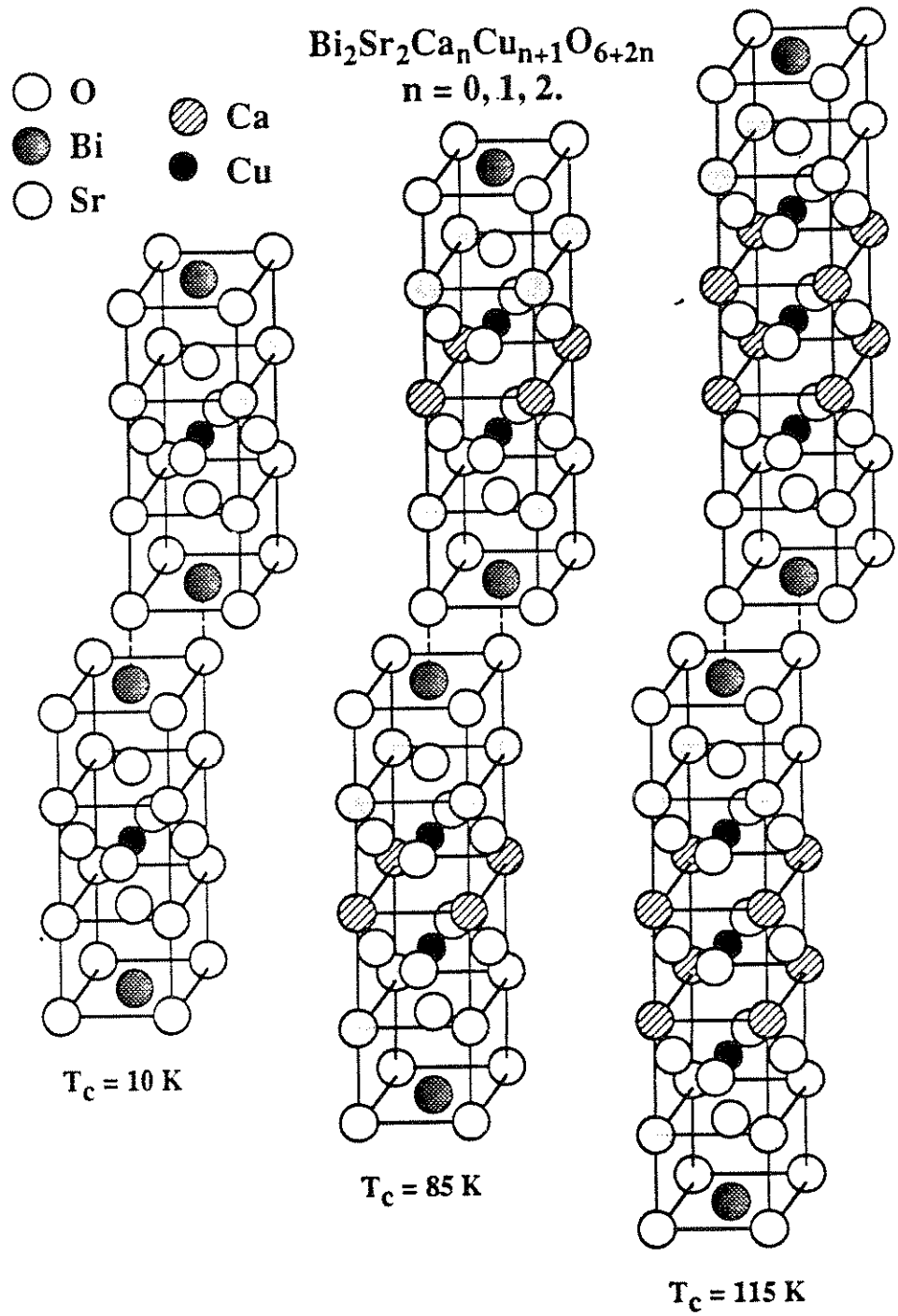

Figure 1.1 The crystal structure of the BSCCO family members and their respective superconducting transition temperatures.

perpendicular to the c-axis. In each chapter, I will discuss in detail the technique used, the interpretation of our measurements and their implication (if any) on applicable theories.

1.2 $Bi_2Sr_2CaCu_2O_8$ crystal structure and preparation.

The high T_c superconductor $Bi_2Sr_2CaCu_2O_8$ was discovered in 1988 by Maeda *et al.*,[10] It is one of the members of a family of high T_c superconductors known as the BSCCO-family, which consists of three members with a stoichiometry given by $Bi_2Sr_2Ca_nCu_{(1+n)}O_{(6+2n)}$ with n = 0, 1, or 2. They are usually referred to as Bi-2201, Bi-2212, and Bi-2223 for n = 0, 1, and 2, respectively. Figure 1.1 shows the crystal structures for these three compounds along with their associated T_c's. These materials exhibit orthorhombic symmetry. The unit cell dimensions for the Bi- 2212 compound are |**a**| =5.3995 Å, |**b**| = 5.4572 Å and |**c**| = 30.7236 Å, with **a** and **b** perpendicular to each other and directed along the planar bismuth-oxygen bonds. The separation of the BiO planes from each other accounts for about 20% of the c-axis dimension, which is a result of the weak bonding between them. This gives the materials a morphology very similar to mica; they cleave very easily along the BiO plane.

We synthesized large single crystals of the Bi-2212 compound with the help of Paul Pinsukanjana, using the following procedure:

i) A mixture of stoichiometry $Bi_{48}Sr_{29}Ca_{20}Cu_{34}O_x$ was prepared using dehydrated Bi_2O_3, $SrCO_3$, $CaCO_3$ and CuO.

ii) The mixture was ground by hand using an agate mortar and pestle and some acetone, or by placing the mixture in a plastic bottle with some zirconia stones and acetone and placing the bottle in a rotating unit for ~10 hours.

iii) The mixture was then placed in a beaker and was dried up using a hot plate at about 40°C.

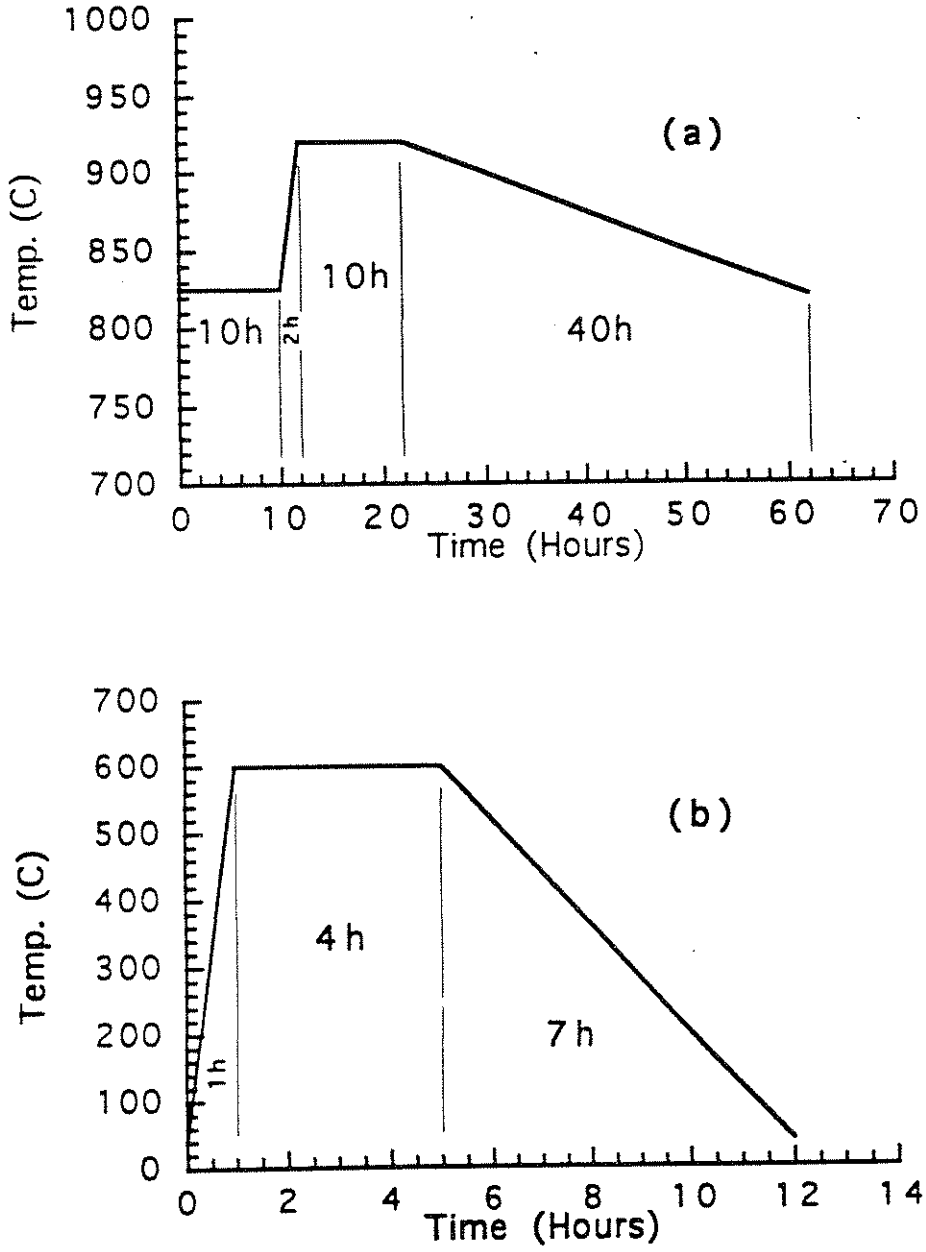

Figure 1.2 (a) Anneal cycle (in flowing oxygen) used to grow single crystals of $Bi_2Sr_2CaCu_2O_8$. (b) Anneal cycle (in flowing oxygen) used to make good silver electric contact pads on this material.

iv) The mixture was poured into a gold lined crucible and baked in flowing oxygen (210 ml/min) using the anneal cycle shown in Fig. 1.2(a).

v) The gold lining was peeled off from the melt to obtain the crystals.

The purpose of the 10 hour at 825°C part of the baking cycle was calcination, i.e., getting rid of the carbon from the carbonates in the mixture. Once the cycle was completed, the melt was broken using surgical scalpels to free stacks of crystals. The single crystals were obtained by using Scotch tape to peel them from the stack. The crystals were then cut to desired geometries and dimensions depending on the experiment. If electric contact pads were needed on the crystals, silver paint was used to make them and the crystal was subjected to the anneal cycle in Fig. 1.2(b) while oxygen was flowing (210 ml/min) through the furnace. This yielded contact pads with a resistance of ~2Ω or less.

References:

1. H. K. Onnes, Commun. Phys. Lab. U. Leiden **124C**, (1911).
2. J. G. Bednorz and K. A. Muller, Z. Phys. B **64**, 189 (1986).
3. C. W. Chu, L. Gao, F. Chen, *et al.*, Nature **365**, 323 (1993).
4. H. London and F. London, Proc. Roy. Soc. Lon., Ser. A **149**, 71 (1935).
5. A. B. Pippard, Proc. Roy. Soc. Lon., Ser. A **216**, 547 (1953).
6. J. Bardeen, L. N. Cooper and J. R. Schrieffer, Phys. Rev. **108**, 1175 (1957).
7. G. M. Eliashberg, Sov. Phys. JETP **111**, 696 (1960).
8. W. L. McMillan, Phys. Rev. **167**, 331 (1968).
9. F. Marsiglio and J. E. Hirsch, Physica C **162-164**, 591 (1989).
10. H. Maeda, Y. Tanaka, M. Fukutumi, *et al.*, Jpn. J. Appl. Phys. **27**, L209 (1988).

Chapter 2

Energy Gap Anisotropy

2.1 Introduction

One of the consequences of quantum mechanics is that the probability $|\psi|^2$ of finding a conduction electron a distance d outside a metal even at low temperatures is not zero, but depends on the metal's work function ϕ through an exponential law $|\psi|^2 \sim \exp(-2\kappa d)$, with $\kappa \approx (2m/\hbar^2)^{1/2}\,\phi^{1/2}$. This allows measurable electrical currents to tunnel between two conductors separated by a thin insulator. Low-energy spectroscopy information of the elementary excitations of the metals can be extracted from careful measurement of the current-voltage (I-V) characteristic of the tunneling arrangement. Giaever[1] discovered in 1960 that if one of the metals is a superconductor, the differential conductance (dI/dV) of the normal-metal-insulator-superconductor (NIS) tunneling sandwich shows the energy gap and the density-of-states peak predicted by the Bardeen, Cooper, and Schrieffer (BCS) theory[2] of superconductivity.

If one considers a thin insulator sandwiched between two conductors, the tunneling current from the left conductor to the right conductor can be written as

$$I_{L\to R} = A \int_{-\infty}^{\infty} |T|^2 N_L(E)\, f(E)\, N_R(E+eV)\, [1-f(E+eV)]\, dE \qquad (2.1)$$

where A is a constant of proportionality, T is assumed to be a constant tunneling-matrix element, V is the applied voltage, i.e., eV is the difference in chemical potential across the junction. The density of states is represented by N(E), and $f(E)$ is the Fermi function. The factors $N_L f$ and $N_R(1-f)$ give the number of occupied states on the left and available

states on the right in unit energy interval respectively. By substracting the current from the right conductor to the left conductor, one finds that the net current is given by

$$I = A\,|T|^2 \int_{-\infty}^{\infty} N_L(E)\, N_R(E+eV)\, [f(E)-f(E+eV)]\, dE \qquad (2.2)$$

In the case of a normal-metal the density of states can be modeled as a continuous distribution of independent-particle energy states with density N(0). This allows to simplify Eq. (2.2) in the case where both conductors are normal metals (NIN) to the following expression

$$I_{nn} = A\,|T|^2\, N_L(0)\, N_R(0)\, eV \equiv V/R_{nn} \qquad (2.3)$$

which gives the expected ohmic relation.

In the case of a superconductor, the BCS theory predicts a density of states which can be modeled as

$$\frac{N_s(E)}{N_n(0)} = \mathrm{Re}\left\{\frac{|E|}{(E^2-\Delta^2)^{1/2}}\right\}, \qquad (2.4)$$

which is known as the "semiconductor model".

If one (SIN) or both metals (SIS) in the junction are superconductors, Eq. (2.2) can now be simplified to the following expressions

$$I_{ns} = \frac{G_{nn}}{e}\int_{\infty}^{\infty} \mathrm{Re}\left\{\frac{|E|}{[E^2-\Delta_L^2]^{1/2}}\right\} [f(E)-f(E+eV)]\, dE, \text{ and}$$

$$I_{ss} = \frac{G_{nn}}{e}\int_{-\infty}^{\infty} \mathrm{Re}\left\{\frac{|E|}{[E^2-\Delta_L^2]^{1/2}}\right\} \mathrm{Re}\left\{\frac{|E+eV|}{[(E+eV)^2-\Delta_R^2]^{1/2}}\right\} [f(E)-f(E+eV)]\, dE \qquad (2.5)$$

respectively, where $G_{nn}\equiv 1/R_{nn}$ is the "normal" conductance of the junction, i.e., the conductance of the junction if both electrodes were normal metals.

Figure (2.1) illustrates the current-voltage characteristics and their origins in the semiconductor model for the NIN, SIN and SIS cases. In the SIN case, the current below $eV=\Delta$ is due to electrons that are thermally excited above the Fermi energy in the normal metal and of holes in the filled states in the superconductor. At $eV=\Delta$ the current has a sharp rise, which at low temperatures defines Δ very accurately and can be compared with the BCS theory prediction of $2\Delta=3.53\ k_BT_c$. Aluminum with a transition temperature of 1.18K has been found[3] to agree very well with this prediction ($2\Delta_{Al}=3.53\ k_BT_c$). Hoewever, the ratio $2\Delta/k_BT_c$ for lead[4] (T_c=7.196K) is 4.67, about 30% greater than the BCS prediction. Other superconducting materials, such as Hg (T_c=4.15 and $2\Delta/k_BT_c$=4.61, Ref. 5) and $Pb_{0.7}Bi_{0.3}$ (T_c=8.45 and $2\Delta/k_BT_c$=4.86, Ref. 6) also exhibit some "excess" in their energy gaps. A large energy gap has been found to be evidence of a strong electron-phonon coupling in a superconductor.

In the SIS case no tunneling current is expected below $eV=\Delta_L+\Delta_R$, where an abrupt rise occurrs, at T=0K. However, at finite temperature an additional thermally activated cusp occurrs at $eV=|\Delta_L-\Delta_R|$, with a negative resistance region above this point. This SIS can be used to determine both superconducting energy gaps from structures in the I-V characteristics arising from the sum and the difference of the two gap energies. In the case when both superconductors are made of the same material only the sharp rise at $eV=2\Delta$ is observed. The semiconductor model overlooks the possibility of condensed pairs tunneling through the insulating barrier and giving rise to a supercurrent $I_J(V=0)$ as

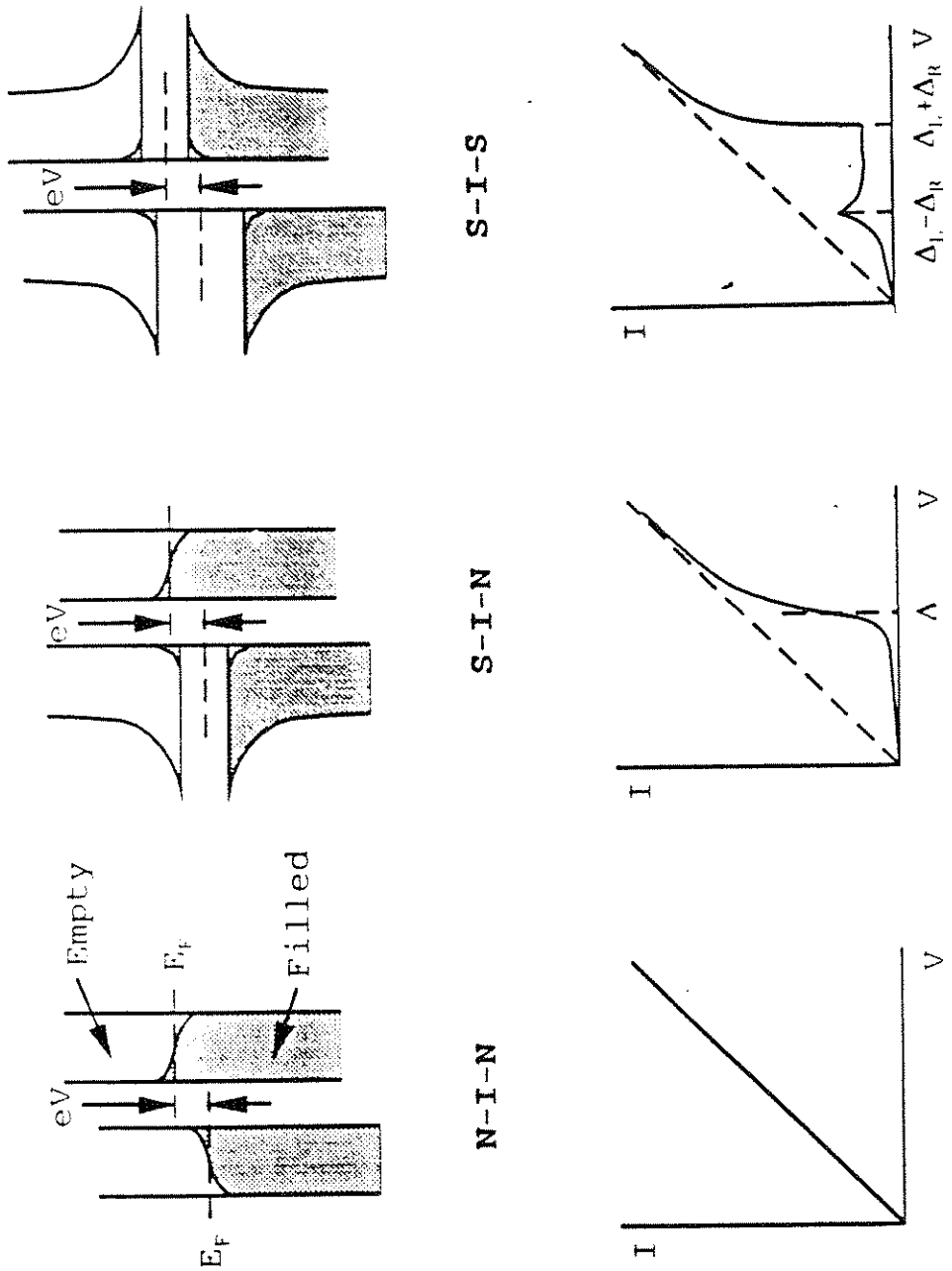

Figure 2.1 The sketches represent the three basic tunneling configurations (NIN, SIN and SIS) with their respective ideal I-V characteristics.

predicted by Josephson[7] in 1962.

2.2 Tunneling apparatus and technique

The most common technique of junction fabrication consists of successive evaporation of crossing film strips using masks, and exposing the first metal surface to air or pure oxygen to produce an oxide barrier. However, due to the complex structure of the high T_c oxides, their high annealing temperature and their short coherence length, point contact and break junction techniques were chosen to determine the superconducting gap of $Bi_2Sr_2CaCu_2O_8$.

Figure 2.2 shows our probe similar in design to that described by Levinstein and Kunzler[8]. Our differential screw apparatus allowed the breaking of single crystals or approaching of a metal tip to the superconducting oxide. The differential screw was designed to move at a rate of ≈0.1μm/degree, with a total traveling length of ≈2mm. When the single crystal break junction technique was used, the ends of the sample were glued to a beryllium-copper substrate using stycast epoxy. One end of the substrate was in turn glued to a sample holder with the same epoxy, and the other end was pushed using a copper hook at the end of the differential screw until the crystal was broken. The differential screw was then adjusted to obtain optimal I-V characteristics. The stycast epoxy was used for its good thermal conductivity and good electrical insulating properties to provide good thermal grounding of the samples and to prevent electrical contact between the sample and the beryllium-copper substrate.

Although ideal I-V characteristics contain enough information to extract an accurate value of the superconducting energy gap, plotting the differential resistance, dV/dI, versus V makes the changes in the junction resistance more apparent and allows a clearer identification of the gap, even in non-ideal situations. Figure 2.3 shows the circuit of a

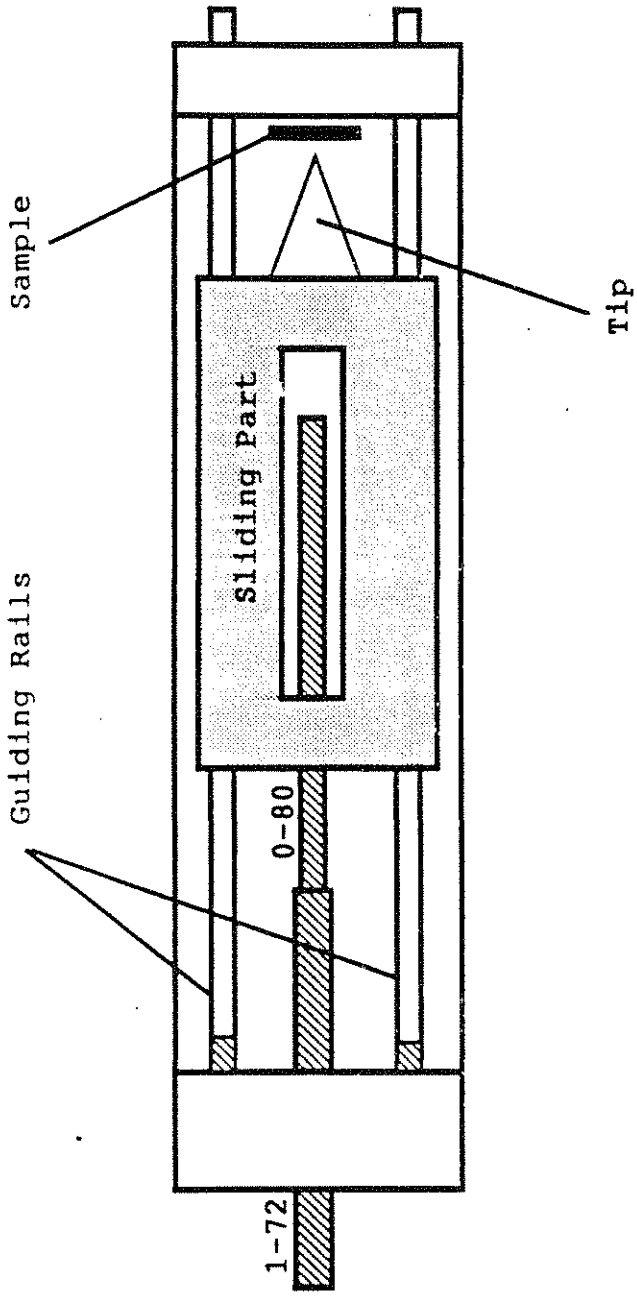

Figure 2.2 A top view of the differential screw tunneling probe used make the point contact and break junctions described in section 2.3.

current bridge that was used to measure such dV/dI-V characteristics. The resistances R1 and R2 were set to $\approx 10 \times \mathrm{Max}(R_{junction})$ to effectively act as current limiters. A Hewlett-Packard XY-recorder was used to measure the I-V and dV/dI-V characteristics. A triangular voltage wave of ≈0.05-0.005 Hz was applied to the DC input to sweep the bias current in both cases. In the case of an I-V, the current through the sample was inferred from measurement of the voltage across R2, and the voltage across the sample was measured directly with a high input impedance Keithley voltmeter. A small sinusoidal signal (≈80-115 Hz) was applied to the AC input to measure the differential resistance of the junction. This signal was adjusted to about 0.1-0.25mV across the sample (Lock-in input A), while biased at its maximum resistance. Keeping the same bias, a decade resistance and capacitance was adjusted to read the same voltage across the lock-in input B. This allowed the optimal sensitivity, since the lock-in amplifier was operated in the A-B mode during the measurement. The AC voltage across the junction (dV) changed as the bias voltage was varied; however, the voltage across the decade resistance and the AC current through the junction remained constant and the output of the lock-in amplifier translated into a change in the differential resistance of the junction. The dV/dI scale was calibrated by fixing the bias and recording the lock-in output while changing the decade resistance in steps by a known amount.

2.3 Experiment and analysis

Some of the most fundamental characteristics of the "high-T_c" oxide superconductors have not yet been experimentally determined with good reliability. One such feature is the superconducting energy gap, Δ. Of the traditional methods used to determine Δ, one of the most direct is electron tunneling spectroscopy, which can in

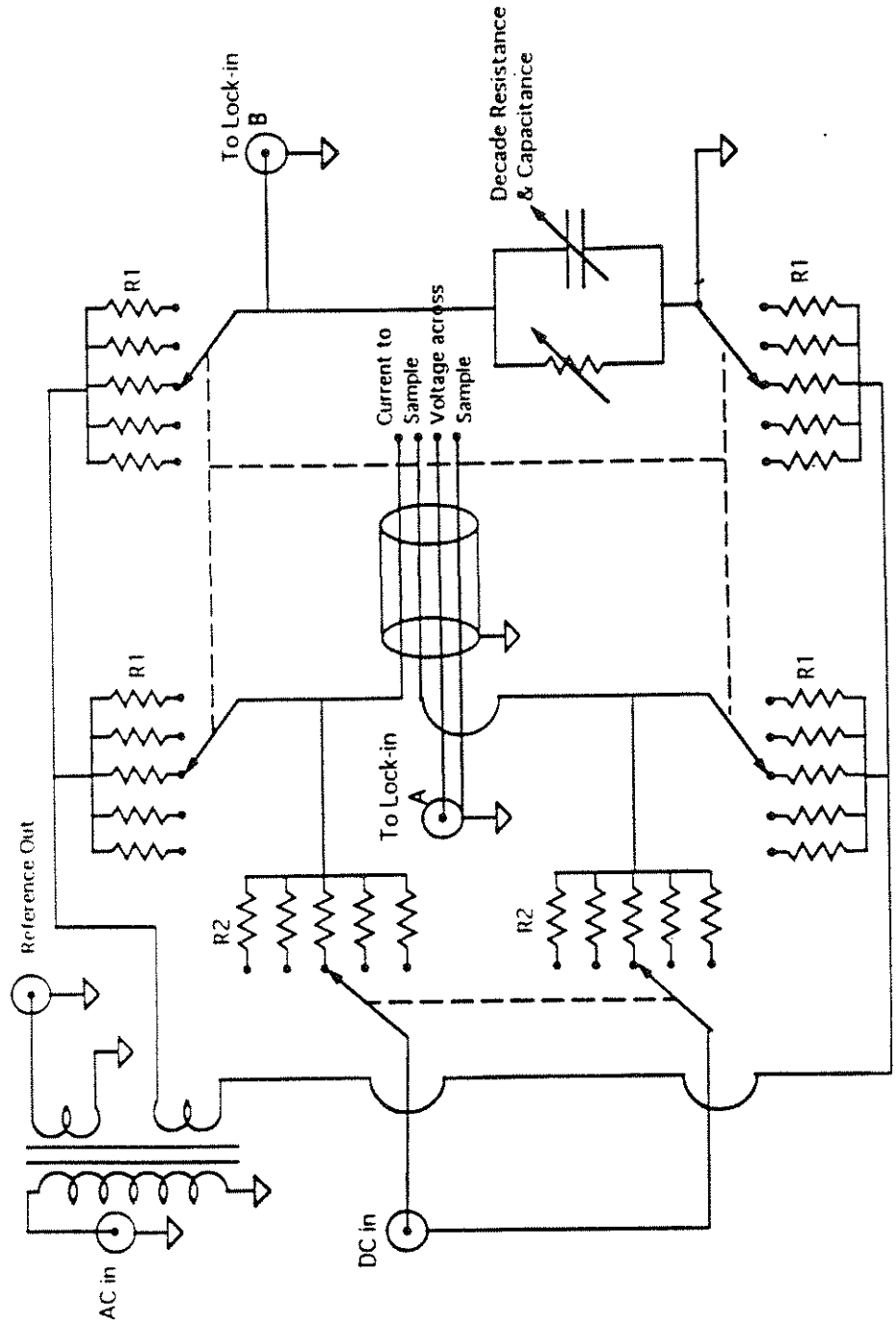

Figure 2.3 The schematics of the current bridge used to measure the I-V and dV/dI-V characteristics of the junctions.

principle also determine gap anisotropy in single crystal specimens. Although many tunneling studies have been performed on high-T_c oxides, the magnitudes of the reported gaps have been inconsistent. In Y-Ba-Cu-O, for example, reported[9-17] tunnel gap values range from $2\Delta_o/k_BT_c$~3 to ~13, while for Bi-Sr-Ca-Cu-O the reported[17-24] gap ratios range from 4.5 to 10. Measurements of an anisotropy in the a-b plane gap structure in a single crystal using angle resolved photoemission and tunneling has been reported[24,25]; however, those measurements disagree on the direction of maximum energy gap by a 45° angle. Much of the problem in performing and interpreting tunneling measurements is that it is a surface measurement, and often the surface is poorly characterized[14]. The high oxygen mobility together with a relatively short coherence length in high-T_c oxides makes these materials prone to poor tunnel junction formation.

We here report on tunneling measurements of the energy gap in single crystals of $Bi_2Sr_2CaCu_2O_8$, with emphasis on gap anisotropy between the a-b plane and the c-axis. To insure reliability of the results, different tunnel configurations have been utilized on well characterized samples with freshly exposed surfaces. Point contact tunneling was performed using superconductor-insulator-superconductor (SIS), superconductor-insulator-normal (SIN), and break-junction (SIS and Josephson) methods. Tunneling electrons were injected the into the a-b plane (Cu-O sheet direction) and c-axis directions. The results suggest a significant gap anisotropy, with $2\Delta_{ab}/k_BT_c \approx 6.2$ and $2\Delta_c/k_BT_c \approx 3.3$.

High purity single crystals of $Bi_2Sr_2CaCu_2O_8$ were prepared as described in section 1.2. The stoichiometry of the crystals was confirmed by SEM x-ray elemental analysis. After the initial synthesis, the crystals were carefully annealed in oxygen to insure homogeneous superconducting properties. The samples were characterized using dc magnetic susceptibility and electrical resistivity measurements, which indicated a bulk T_c=85K. Our tunneling probe operated as described in the previous section. All T=4.2K

measurements were performed with the sample immersed in liquid helium; higher temperature measurements were performed in a helium gas flow cryostat.

Figure 2.4 shows the dV/dI characteristics of an SIN junction at 4.2K, formed between a normal indium tip and a $Bi_2Sr_2CaCu_2O_8$ab plane "edge" exposed by cleanly breaking a crystal along a plane parallel to the c-axis. The direction of electron tunneling is presumably along the a-b plane. At low bias voltages, unusual structure is observed in dV/dI; this structure was not always reproducible and its origin is unknown. However, a reproducible feature is observed close to ±20mV. We associate this feature with the superconducting energy gap. If we take the local conductivity maximum as the value of the gap, then Δ_{ab}=22.5meV at 4.2K. The SIN tunneling experiment described in Fig. 2.4 was repeated at selected temperatures, and the gap feature was found to vary smoothly with temperature. Figure 2.5 shows the position of the local differential conductivity maximum as a function of temperature. The solid line is the BCS gap, fit to the T = 4.2 K and T = 76 K data points. The fit suggests $\Delta_{ab}(T=0)$ = 22.5 meV and T_c = 85.4 K, where the relation $\Delta(T)/\Delta(0)=1.74[1-T/T_c]^{1/2}$ was used near T_c. The tunneling determined "local" transition temperature T_c = 85.4 K is in excellent agreement with the bulk T_c = 85 K for this particular crystal, consistent with high sample homogeneity. With T_c=85K, we find $2\Delta_{ab}(T=0)/k_BT_c = 6.2 \pm 0.3$.

To confirm the above value of Δ_{ab} and to further test the reliability of SIS tunnel junctions formed using $Bi_2Sr_2CaCu_2O_8$ crystal "edges", we formed a break junction across the a-b plane of a single crystal as described in the previous section. The junction was formed and measured at 4.2 K to insure pristine crystal surfaces. The inset to Fig. 2.6 shows the junction configuration. The separation distance between superconductors in the break region could be adjusted from outside the cryostat, and the I-V characteristics could be reversibly changed from "Josephson like" to non-supercurrent SIS like. Figure 2.6 shows a typical I-V curve in the Josephson regime. The junction is highly hysteric at

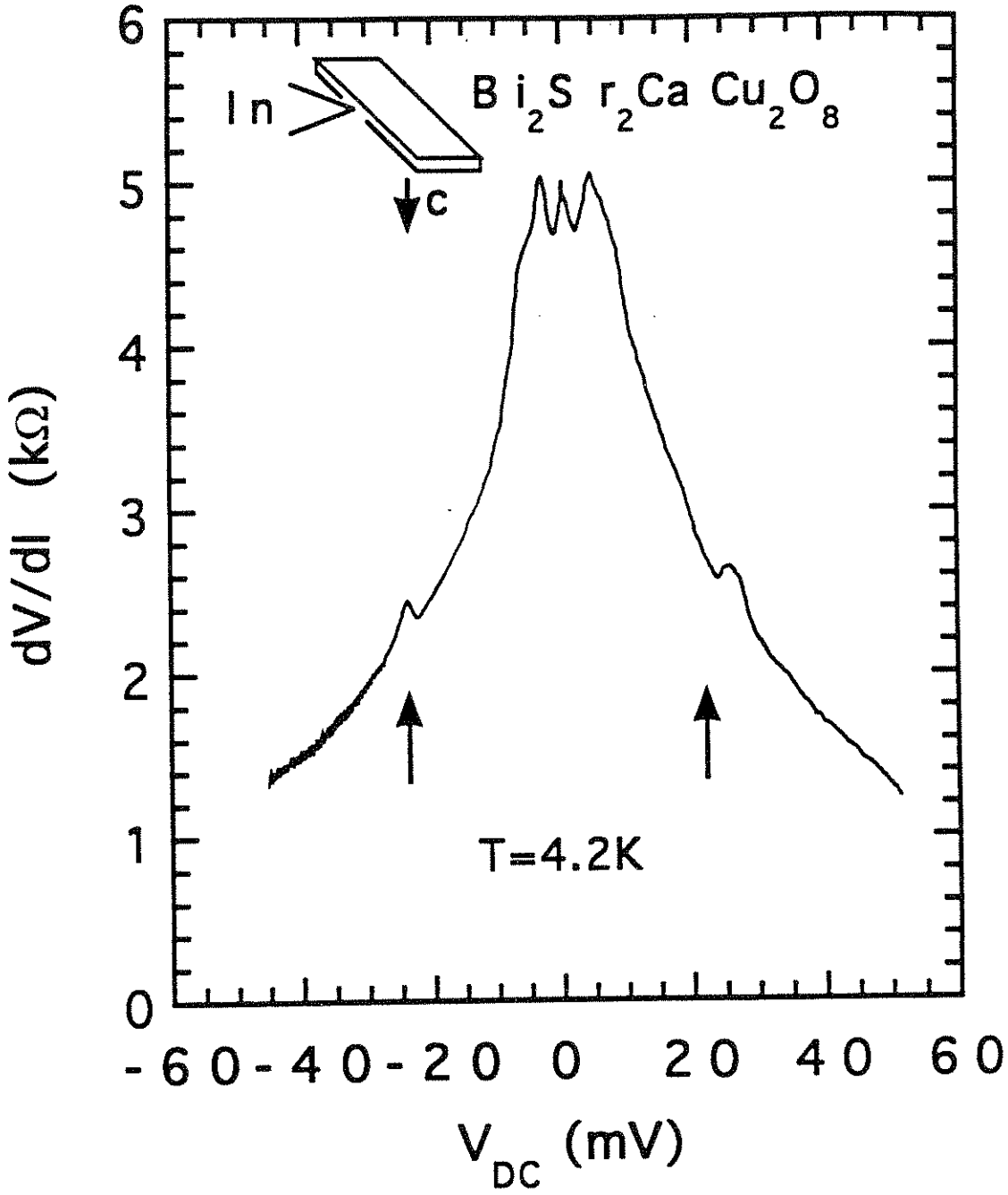

Figure 2.4 SIN tunneling into the a-b plane of $Bi_2Sr_2CaCu_2O_8$. The arrows identify Δ_{ab}.

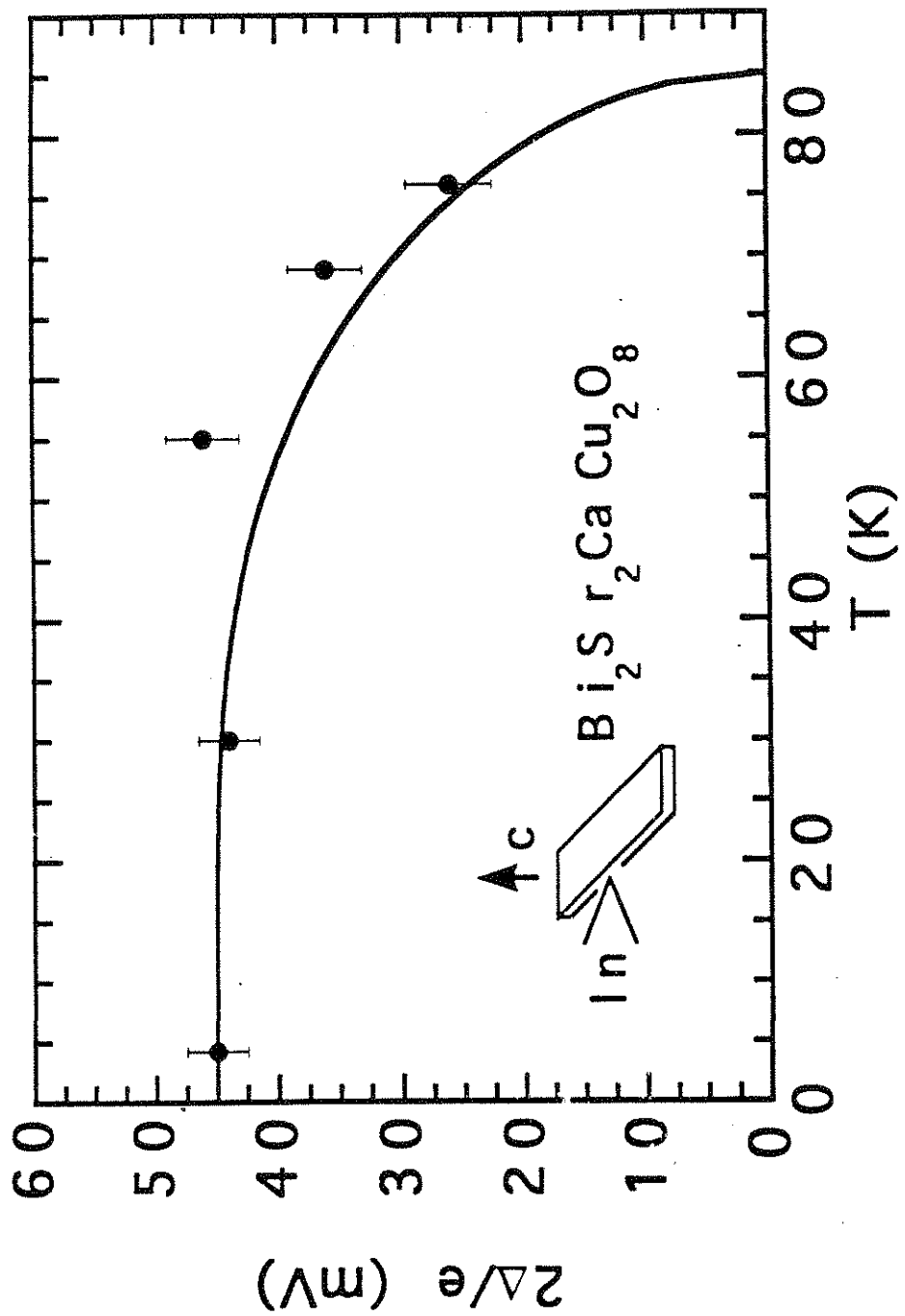

Figure 2.5 The temperature dependence of Δ_{ab}; the solid line is the BCS gap temperature behavior.

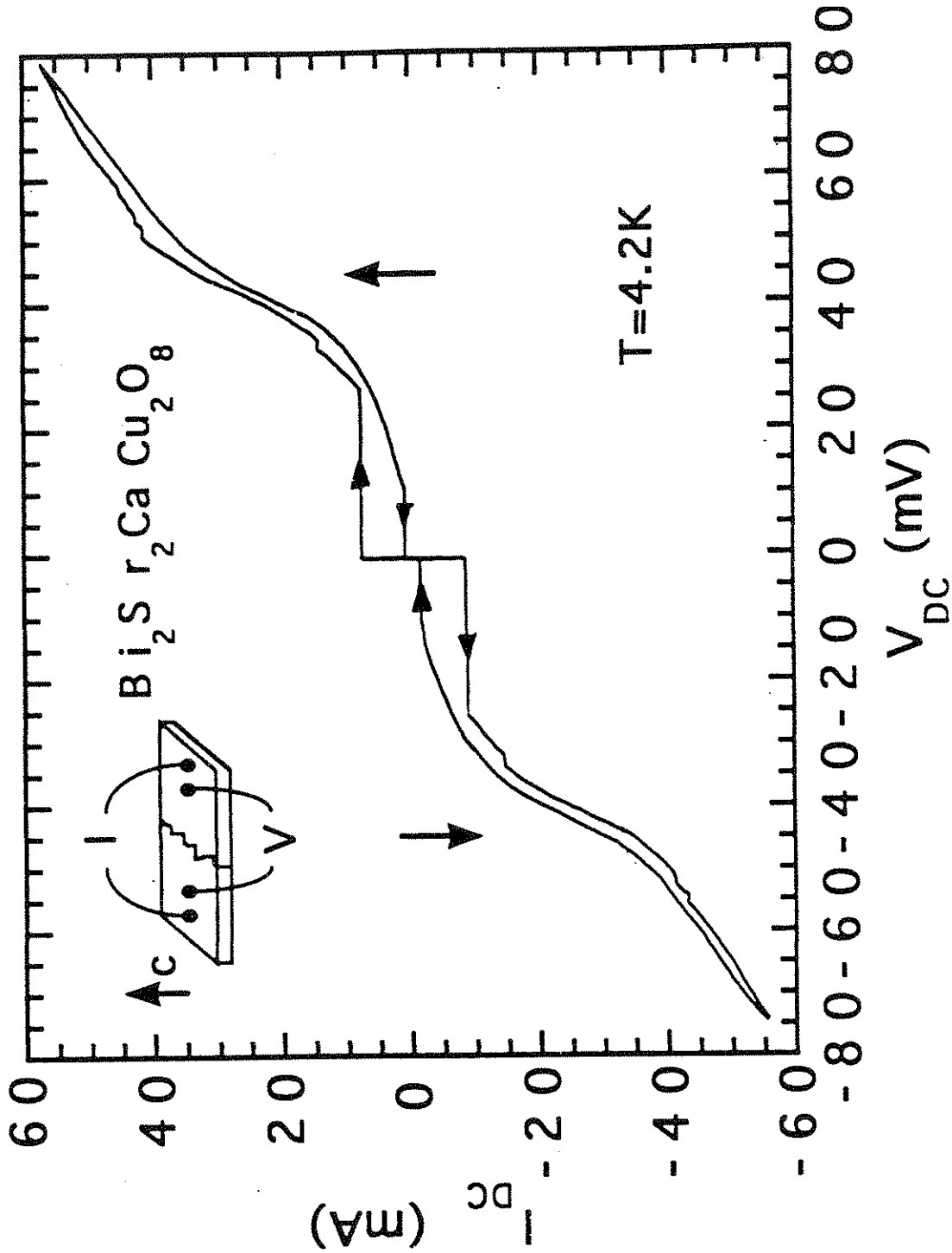

Figure 2.6 I-V characteristics of a-b plane Josephson-like break junction in $Bi_2Sr_2CaCu_2O_8$. The arrows identify the maximum slope at $2\Delta_{ab}$=45meV.

low voltages, but the maximum slope occurs reproducibly near ±45mV. If this value is taken as $2\Delta_{ab}$, we find Δ_{ab}=22.5 meV, in accord with the SIN results.

To explore the energy gap structure along the c-axis, we employed a "differential" tunneling configuration, as shown in the inset of Fig. 2.7. Well characterized $Bi_2Sr_2CaCu_2O_8$ crystals were mounted and cleaved such that tunneling would take place from the ab-plane direction of one crystal into the c-axis direction of another crystal. The junction is thus of the S_{ab}-I-S_c type, where the subscripts refer to potentially different values of the energy gap. Figure 2.7 shows the I-V and dV/dI characteristics of the differential tunnel junction. dV/dI shows two distinct features, which we identify as corresponding to the sum and differences of the energy gaps in the ab-plane and c-axis directions. Again taking the local maximum in the differential conductance as the relevant energy, we find $\Delta_{ab} + \Delta_c = 35$ meV and $\Delta_{ab} - \Delta_c = 11$ meV. Solving for Δ_{ab} and Δ_c gives $\Delta_{ab} = 23$ meV and $\Delta_c = 12$ meV. The value for Δ_{ab} is in good agreement with that determined above, 22.5 meV. Again with $T_c = 85$ K, we find $2\Delta_c/k_BT_c = 3.3 \pm 0.3$. These measurements suggest an energy gap anisotropy in $Bi_2Sr_2CaCu_2O_8$ at low temperatures of about a factor of 2.

The features described above are characteristic of the majority of our tunneling measurements for numerous $Bi_2Sr_2CaCu_2O_8$ crystals, employing different break junction configurations and different normal-metal and superconducting tunnel electrodes. In some cases, however, sharp multiple-peak "charging" structures, similar to those reported by van Bentum *et al.*,[9] were observed which obscured the smaller magnitude gap structure. On occasion we also observed evidence for two independent gap structures in a given I-V trace for a particular tunneling direction. For example, in one break tunnel junction we observed at 4.2 K local conductivity maxima at 25 mV and 46.2 mV. Interpreting these features in terms of SIS tunneling implies gap values of 12.5 meV and 23.1 meV. The

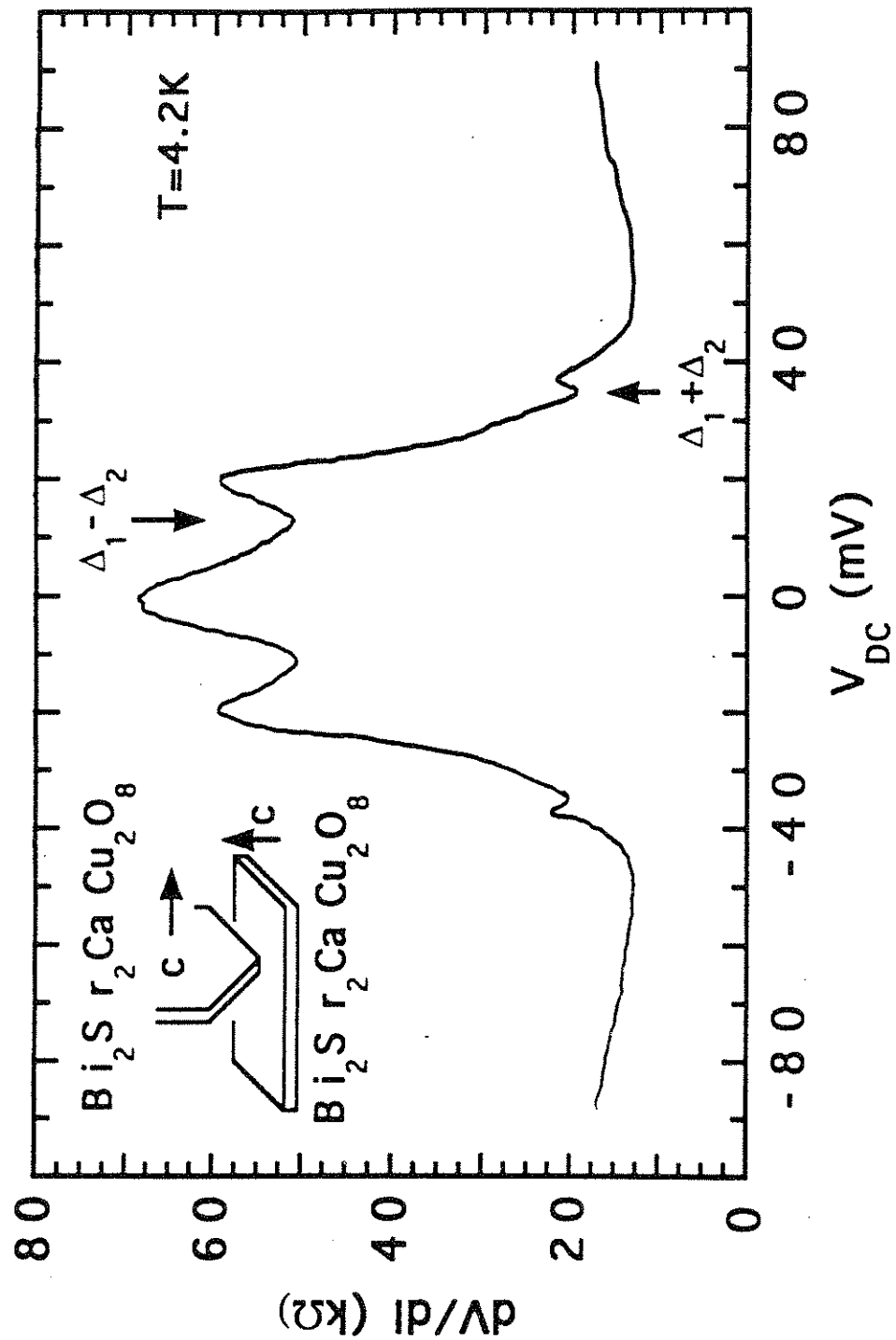

Figure 2.7 "Differential" SIS tunneling between two orthogonal $Bi_2Sr_2CaCu_2O_8$ crystals. The vertical arrows identify the sum and difference gaps, $\Delta_{ab}+\Delta_c$ and $\Delta_{ab}-\Delta_c$.

lower value corresponds well to the previously identified Δ_c, while the larger value is close to Δ_{ab}.

Figure 2.8 shows similar "double gap" features in a point contact SIN measurement made by tunneling from a normal Pt/Rh tip into the c-axis direction of a freshly cleaved $Bi_2Sr_2CaCu_2O_8$ crystal. Here structure is observed at 12 mV and 20 mV. The former value again corresponds to our assumed Δ_c, while the later value is comparable to (but slightly less than) Δ_{ab}. One possible interpretation of such data is that for some junctions the tunnel current is not always confined to a single junction, and different junctions may (because of steps in the cleavage planes) correspond to tunneling into different crystal directions. There also exists the possibility that for certain junction configurations the tunnel current in a highly anisotropic system is non-ballistic, and that for different bias voltages the tunnel current independently probes different crystal directions. Alternatively, the gap parameter in $Bi_2Sr_2CaCu_2O_8$ may be modulated along the c-axis direction and essentially double-valued along this direction (see below).

Our measurements show that in the a-b plane, $2\Delta_{ab}/k_BT_c$≈6-7. This a-b plane value is in accord with several previous tunneling measurements, and is also consistent with the maximum energy gap determined by recent high resolution photoemission studies[25] where it was found $2\Delta/k_BT_c$=6.2. The observed ratios are far in excess of the expected BCS result[2] (for weak coupling $2\Delta/k_BT_c$=3.53) and are also in excess of the ratios determined for conventional strong-coupled superconductors ($2\Delta/k_BT_c$≈4~5). On the other hand, the gap magnitude determined for the c-axis in $Bi_2Sr_2CaCu_2O_8$ is in accord with the BCS prediction.

From the extreme structural and electrical anisotropy[26] of $Bi_2Sr_2CaCu_2O_8$, it is not unreasonable to expect some energy gap anisotropy. One (highly oversimplified) picture of $Bi_2Sr_2CaCu_2O_8$ might be one of highly conducting Cu-O layer complexes

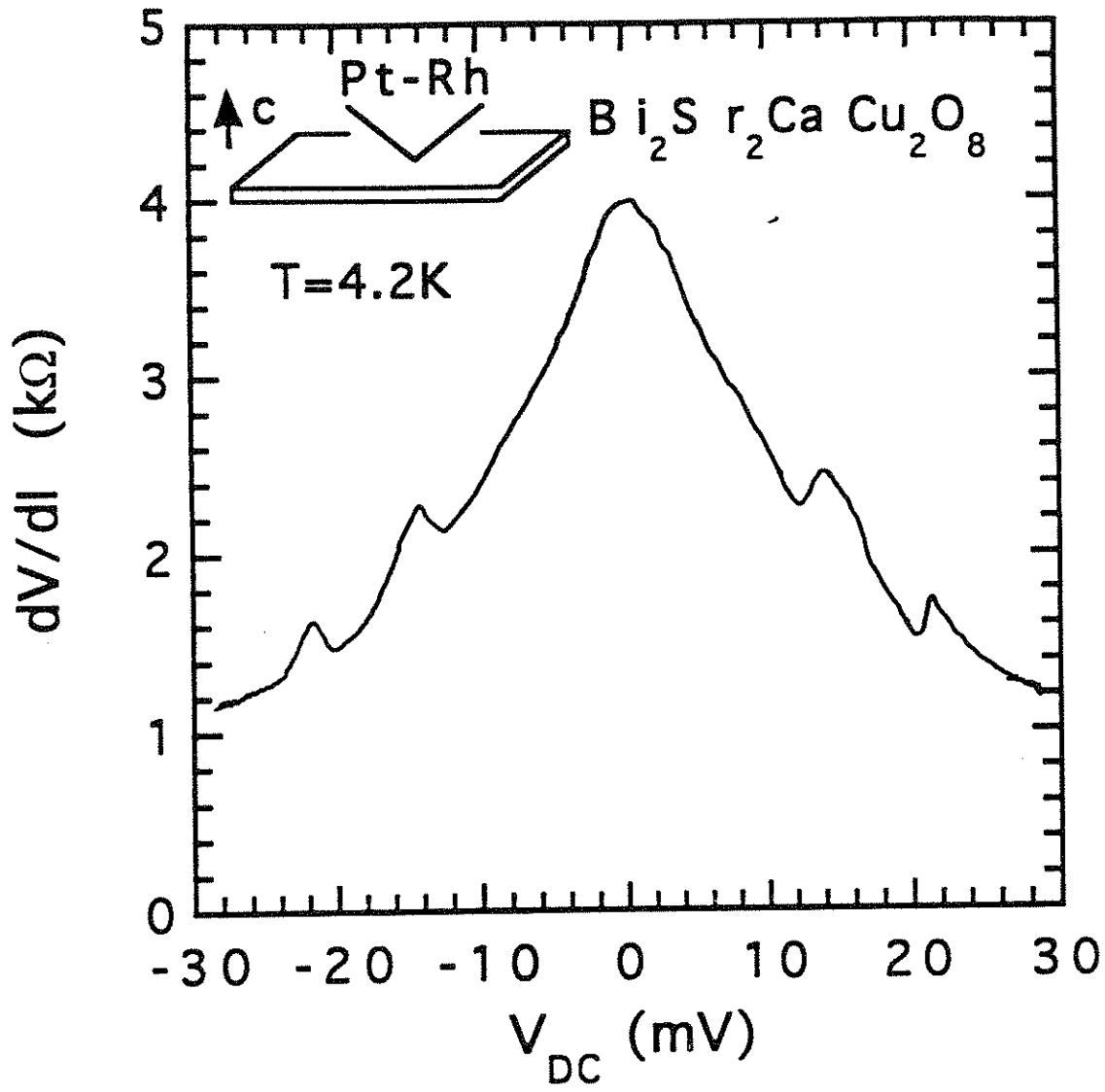

Figure 2.8 SIN tunneling into the c-axis of $Bi_2Sr_2CaCu_2O_8$. Two gap structures are observed.

separated by "insulating" Bi-O layers. In the superconducting state, the Bi-O layers are superconducting, but the superconductivity is "weaker" there. The situation is somewhat analogous to a reduced order parameter by the proximity effect. Such an argument would suggest an order parameter constant in the a-b plane, but a gap value modulated along the c-axis direction. Since $Bi_2Sr_2CaCu_2O_8$ is known to cleave along the Bi-O layers, a c-axis tunneling measurement would invariably extract the reduced gap value near the surface. High voltage current injection well above the surface gap energy may then probe the secondary gap structure of the underlying Cu-O plane complex, consistent with the double gap structure seen in Fig. 2.7. This inequivalency of the layers in this material is supported by the theoretical work of Theodorakis[27], and more recent experimental evidence that this material consists of weakly Josephson-coupled layers along the c-axis.[28]

The above description suggests a strong correlation between normal state electrical anisotropy and gap anisotropy. In $YBa_2Cu_3O_7$, the normal state electrical anisotropy[29] is significantly less than that[26] in $Bi_2Sr_2CaCu_2O_8$. Although reliable single crystal anisotropic tunneling data do not exist for $YBa_2Cu_3O_7$, Tsai *et al.*,[17] have performed tunnelling into clean edges of preferentially oriented films, and find $2\Delta_{ab}/k_BT_c$=6.1 and $2\Delta_c/k_BT_c$=3.6. Hence the implied gap anisotropy in that material is comparable to that suggested for $Bi_2Sr_2CaCu_2O_8$. An important question is thus whether or not the gap anisotropy is a direct manifestation of the Cu-O plane structure and relatively independent of other structural and electronic details of the material.

In conclusion, tunneling measurements into different crystal directions of $Bi_2Sr_2CaCu_2O_8$ suggest that the energy gap may be anisotropic by about a factor of two, being larger in the a-b plane direction. The temperature dependence of Δ agrees well with the BCS curve (or mean field theory in general), but the largest gap value is $2\Delta_{ab}/k_BT_c$=6.3, a ratio significantly greater than that expected from BCS theory.

References:

1. I. Giaever, Phys. Rev. Lett. **5**, 147 (1960).
2. J. Bardeen, L. N. Cooper and J. R. Schrieffer, Phys. Rev. **108**, 1175 (1957).
3. B. L. Blackford and R. H. March, Can. J. Phys. **46**, 141 (1968).
4. W. L. McMillan and J. M. Rowell, Phys. Rev. Lett. **14**, 108 (1965).
5. W. N. Hubin and D. M. Ginsberg, Phys. Rev. **188**, 716 (1969).
6. R. C. Dynes and J. M. Rowell, Phys. Rev. B **11**, 1884 (1975).
7. B. D. Josephson, Phys. Lett. **1**, 251 (1962).
8. H. J. Levinstein and J. E. Kunzler, Phys. Lett. **20**, 581 (1966).
9. P. J. M. van Bentum, L. E. C. van de Leemput, L. W. M. Schreurs, *et al.*, Phys. Rev. B **36**, 843 (1987).
10. J. Moreland, J. W. Ekin, L. F. Goodrich, *et al.*, Phys. Rev. B **35**, 8856 (1987).
11. J. R. Kirtley, R. T. Collins, Z. Schlesinger, *et al.*, Phys. Rev. B **35**, 8846 (1987).
12. M. D. Kirk, D. P. E. Smith, D. B. Mitzi, *et al.*, Phys. Rev. B **35**, 8850 (1987).
13. I. Iguchi, S. Narumi, Y. Kasai, *et al.*, Physica B & C **148B+C**, 322 (1987).
14. A. Edgar, C. J. Adkins and S. J. Chandler, J. Phys. C **20**, L1009 (1987).
15. M. F. Crommie, L. C. Bourne, A. Zettl, *et al.*, , (1987).
16. M. Sera, S. Shamoto and M. Sato, Solid State Commun. **65**, 997 (1988).
17. J. S. Tsai, I. Takeuchi, J. Fujita, *et al.*, Physica C **157**, 537 (1989).
18. S. Vieira, M. A. Ramos, M. Vallet-Regí, *et al.*, Phys. Rev. B **38**, 9295 (1988).

19. C. Yingfei, T. Hongjie, Z. Shiping, *et al.*, Mod. Phys. Lett. B **2**, 903 (1988).

20. M. Lee, D. B. Mitzi, A. Kapitulnik, *et al.*, Phys. Rev. B **39**, 801 (1989).

21. A. Zettl, A. Behrooz, G. Briceño, *et al.*, in *Mechanisms of High Temperature Superconductivity*, H. Kamimura and A. Oshiyama, Eds. (Spring Verlag, Berlin, 1988), pp. 249.

22. N. A. Tulina, S. V. Zaitsev, M. P. Kulakov, *et al.*, Physica C **171**, 103 (1990).

23. M. H. Jiang, C. A. Ventrice, K. J. Scoles, *et al.*, Physica C **183**, 39 (1991).

24. J. Kane, Q. Chen, K.-W. Ng, *et al.*, Phys. Rev. Lett. **72**, 128 (1994).

25. Z.-X. Shen, D. S. Dessau, B. O. Wells, *et al.*, Phys. Rev. Lett. **70**, 1553 (1993).

26. S. Martin, A. T. Fiory, R. M. Fleming, *et al.*, Phys. Rev. Lett. **60**, 2194 (1988).

27. S. Theodorakis and Z. Tesanovic, Phys. Lett. A **132**, 372 (1988).

28. R. Kleiner, F. Steinmeyer, G. Kunkel, *et al.*, Phys. Rev. Lett. **68**, 2394 (1992).

29. S. W. Tozer, A. W. Klienasser, T. Penny, *et al.*, Phys. Rev. Lett. **59**, 1768 (1987).

Chapter 3

Hall Resistance and Mobility.

3.1 Introduction

In several new classes of CuO_2 based superconducting oxides, the normal state is characterized by either hole or electron carriers in low concentration, with moderate to severe structural and electrical anisotropy. The transport properties are often very different from those expected for a simple metal, and are sensitive to chemical doping (in particular oxygen). It has been demonstrated[1] that a metal-"insulator" transition can be induced by changing the oxygen configuration of $Bi_2Sr_2CaCu_2O_{8-x}$ (i.e., the actual oxygen content with possible associated defect structure). The term insulator here refers to a nonmetalic state where the electrical resistivity increases with decreasing temperature, similar to semiconducting behavior. Both the resistivity and the thermoelectric power obey simple empirical expressions, which also apply to other high T_c superconductors.[1,2]

One of the most useful transport probes to characterize a novel system is the Hall effect, since it provides information on the carrier density, as well as the sign of the carriers. In a normal metal, where the carrier energy levels can be described by conventional band theory, the transport properties due to external fields and/or temperature gradients can be explained in terms of the Bloch-Boltzmann transport theory. The conductivity tensor is then given by

$$\vec{\sigma} = \frac{1}{4\pi^3} \frac{q^2 \tau}{\hbar} \int \frac{v_k \, v_k \, dS_F}{v_k} \quad , \tag{3.1}$$

where q is the charge of the carrier, τ is the energy and wave-vector independent relaxation time for the carriers, and the integral is over the Fermi surface. The Hall coefficient is given by

$$R_H = \frac{q\,\tau}{m\,c}\,\rho_o \qquad (3.2)$$

where ρ_o is the ordinary resistivity of the material. In the case of a free electron gas these transport coefficients reduce to $\sigma = nq^2\tau/m$ and $R_H = 1/nqc$, respectively.

3.2 Hall effect technique

A uniform current distribution and a perfect alignment of two transverse voltage contacts across a sample are enough to measure a transverse voltage (Hall voltage) in a magnetic field. However, in reality no such perfect conditions exist and the measurement of a transverse voltage requires a way of compensating for the misalignment of the transverse voltage leads. This is usually accomplished by using three transverse voltage contacts (two on the same side with the third more or less across their midpoint) and two contacts for a uniform current. A voltage divider across the neighboring contacts can then be adjusted to null any "transverse" voltage across the sample with no applied magnetic field. The magnetic field is then applied allowing the measurement of the Hall voltage.

Another, not so conventional, way of compensating for the voltage contacts misalignment is to produce a nonuniform current through three leads in the sample and vary the current profile until not voltage is detected across the two opposite voltage leads. Following the suggestion of Friend and Bett[3] a three terminal AC current source was designed to produce such a nonuniform current through the sample and balance the misalignment voltage across the Hall effect contacts.

We used this second technique to measure the Hall effect in $Bi_2Sr_2CaCu_2O_{8-x}$. Figure 3.1 shows the schematics of the current source that we use in our measurements. It can be seen from Fig. 3.1(a) that since an operational amplifier has ideally infinite input impedance (no input current) and infinite gain (no voltage across its input leads) the total current $I_o=V_\beta/R$, $I_\alpha=V_\alpha/R$ and $I_\beta=I_o-I_\alpha$. The net current through the sample is determined by the amplitude of the AC input to the transformer and the value of the resistance R. By changing the voltage V_α, by means of the potentiometers attached to the secondary, we change both I_α and $I_\beta=I_o-I_\alpha$, as to keep I_o constant. The schematics of the amplifiers α and β are identical and is shown in Fig. 3.1(b).

In Fig. 3.2 we show the block diagram of our setup. An oscillator was used to generate a sinusoidal wave of frequency=200Hz that was used as the input to the current source described above. The net current through the sample was measured using a lock-in amplifier connected to a standard 1Ω resistor in series with the sample. The Hall voltage across the sample was detected with another lock-in amplifier. A PAR low noise transformer was used to match the impedance of the sample to that of the lock-in amplifier, and to amplify the signal by a factor of 100. We should point out that the connections from the sample to the transformer to the lock-in amplifier were shielded from outside radiation.

The ab-plane Hall effect was measured in several $Bi_2Sr_2CaCu_2O_8$ samples with the magnetic field oriented along the c-axis and the current **J**||**ab**-plane. The measurements where made with a homemade electromagnet capable of producing dc magnetic fields up to 2 T. The samples were mounted on a cold finger cooled with cold He gas flow. The Hall voltage was always measured for both polarities of the magnetic field to cancel out any spurious voltages and increased the sensitivity of the measurement.

The resistivity of the sample was measured by using the conventional four point collinear geometry.

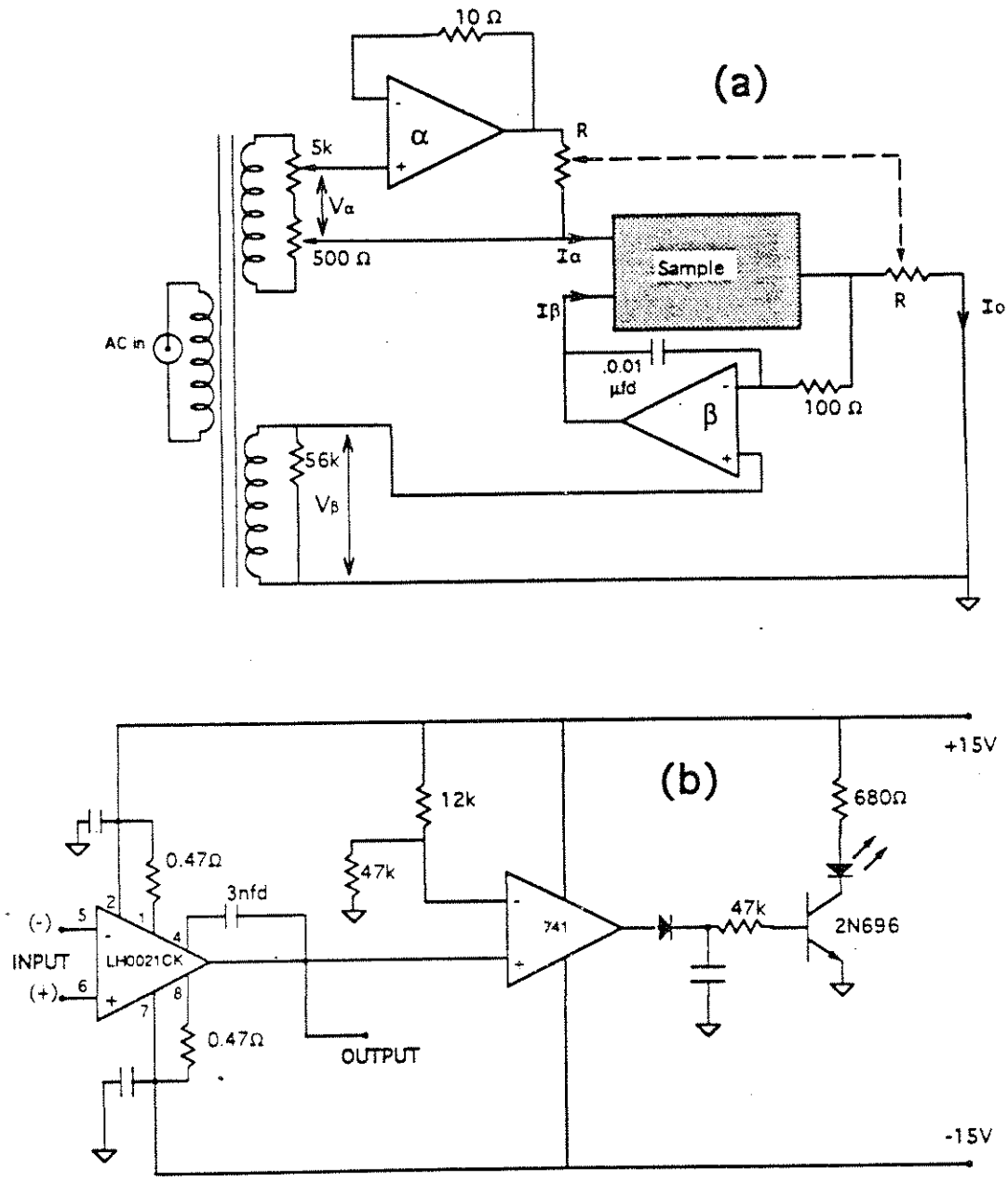

Figure 3.1 (a) Block diagram of the three-current dividing circuit for Hall effect measurement. (b) Circuit for the amplifiers α and β in (a), with overload indicated by the LED.

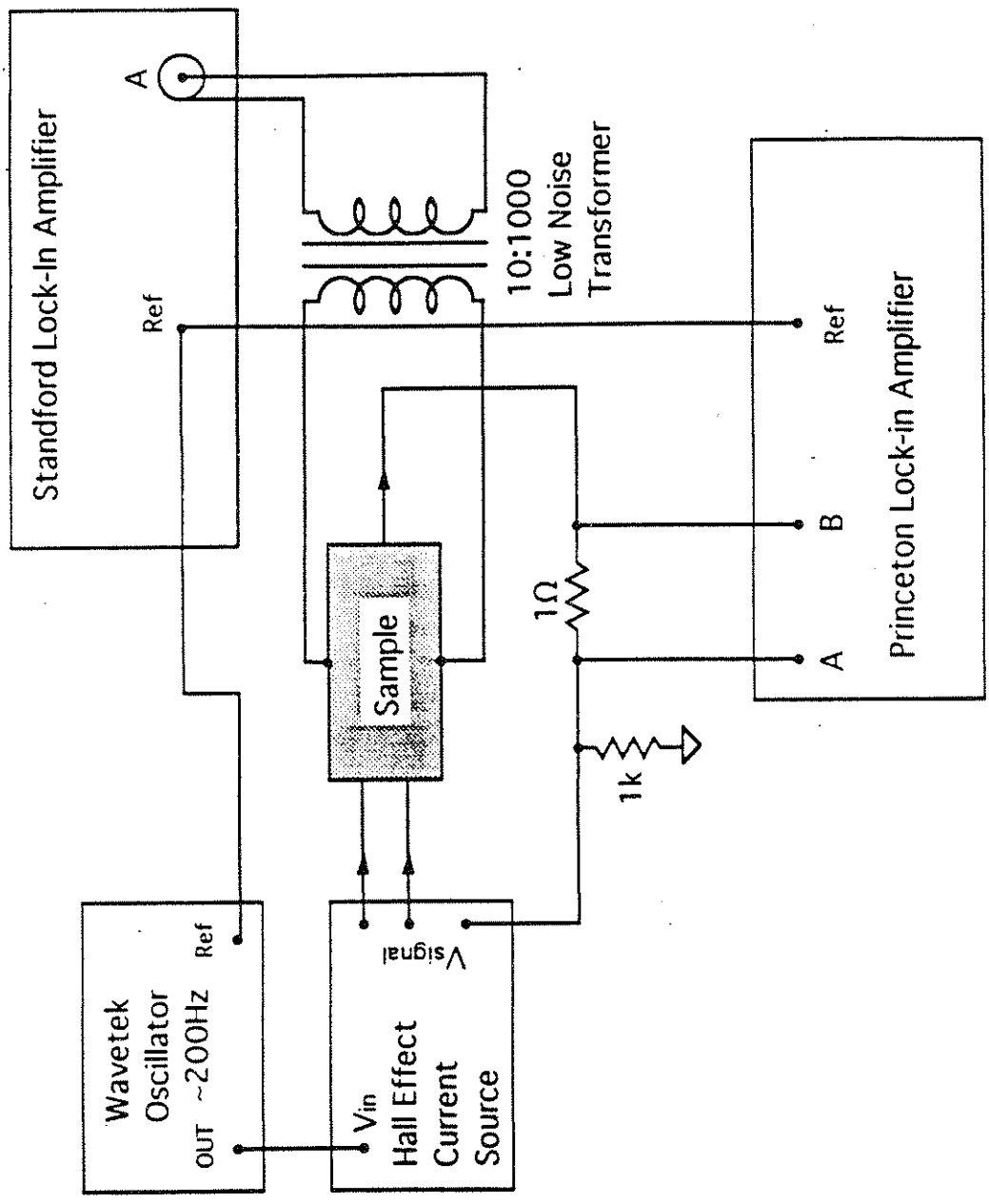

Figure 3.2 Bolck diagram of the setup used to measure the Hall effect. The diagram of the current source is shwon in Fig. 3.1.

3.3 Resistivity and Hall coefficient.

In this section I will discuss the simultaneous measurement of the ab-plane resistivity ρ_{ab} and the ab-plane Hall coefficient R_H of single crystal $Bi_2Sr_2CaCu_2O_{8-x}$. The temperature dependence of both R_H and ρ_{ab} follow simple functional forms, which remain intact as the sample is driven across the (loosely defined) metal-insulator transition by oxygen depletion. We use these transport coefficients to extract characteristic transport parameters, and compare our results to those predicted by various novel normal-state conduction mechanisms.

High purity single crystals of $Bi_2Sr_2CaCu_2O_{8-x}$ were grown from a mixture of Bi_2O_3, $SrCO_3$, $CaCO_3$, and CuO as described in section (1.2). The crystals were cleaved and cut into thin ab-plane sheets of typical dimensions 2.0 mm × 1.0 mm × 10μm, where the small dimension corresponds to the c-axis direction. The samples were optically smooth and shiny and had no major visible defects. The resistivity was measured using a modified linear four-probe contact configuration with fired-on silver paint contact pads, and the Hall voltage was obtained simultaneously using an ac current source and lock-in detection with a five-probe arrangement,[3] as described in the previous section. The magnetic field was oriented parallel to the c-axis, and hence the Lorentz force was in the ab-plane. R_H showed linearity in applied current up to 2.5 mA and applied magnetic field up to 15 kG, the maximum values applied.

Figure 3.3 shows the ab-plane resistivity and Hall coefficient of a particular $Bi_2Sr_2CaCu_2O_{8-x}$ crystal for four different oxygen configurations. The lower half of the figure shows the temperature-dependent resistivity. Curve A is for the crystal following an initial enriched oxygen atmosphere anneal (5 hours at 650°C, followed by a 12-hour ramp to 25°C, in 1-atm O_2 flow). The resistivity is linear and metallic before doping to zero at $T_c \approx 83$ K, and a room-temperature value of ≈ 480 μΩ-cm, typical in this material. Curves B-D are for the same crystal with successively lower oxygen concentration.

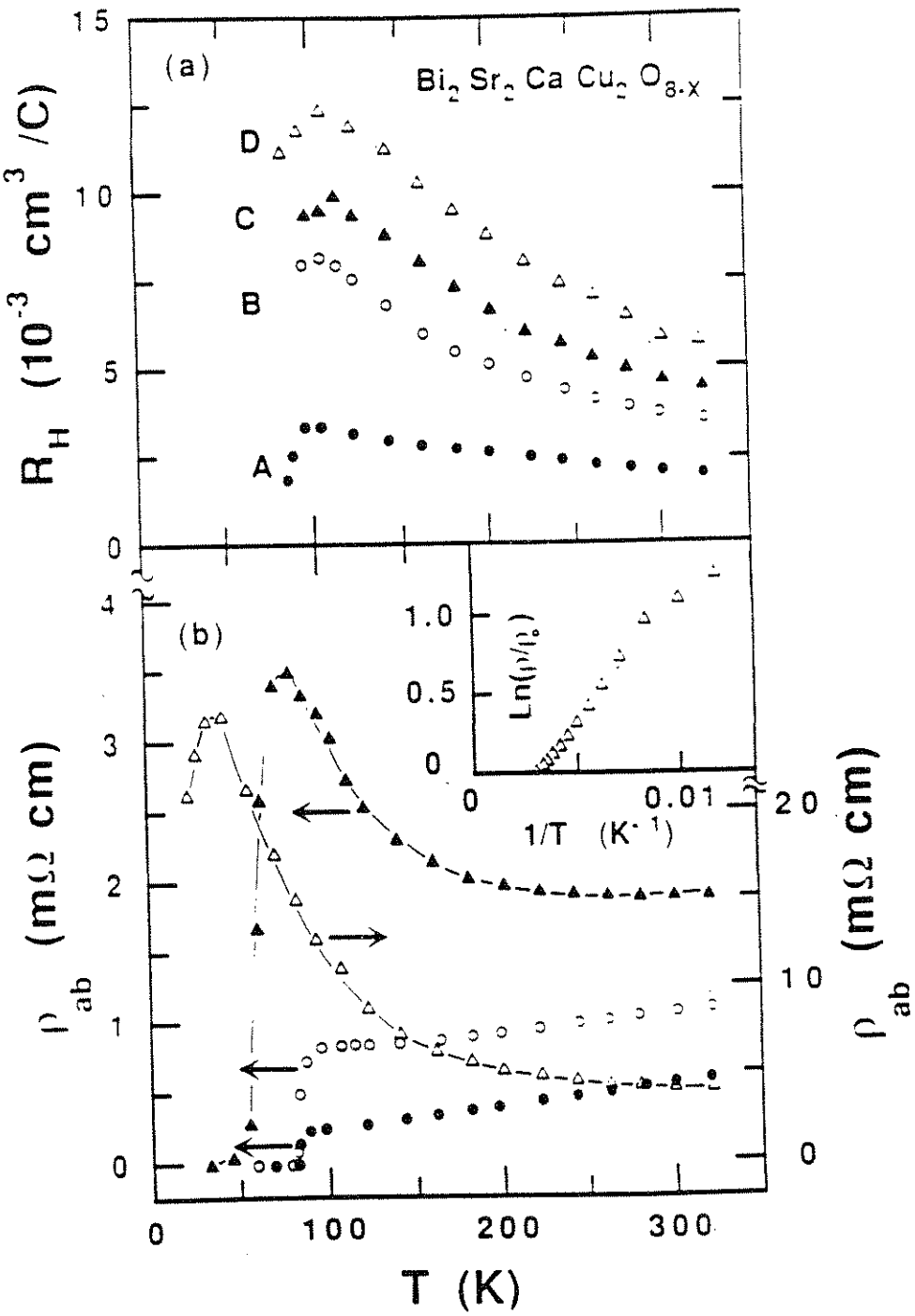

Figure 3.3. Hall coefficient and resistivity for ab-plane of $Bi_2Sr_2CaCu_2O_{8-x}$ single crystal for different oxygen configurations (see text). The resistivity changes from metallic to semiconductive behavior while R_H increases and becomes more temperature dependent.

Consistent with previous work,[1] oxygen depletion changes ρ_{ab} from metallic to insulator-like (or semiconductor-like), with a concomitant depression of T_c. The oxygen configuration of sample "B" was established the following low oxygen anneal cycle: 5 hours at 325°C, followed by a 12-hour ramp to 25°C, all at ~10 mTorr O_2. This treatment the room-temperature resistivity by a factor of 2, still showing metallic behavior down to ~130 K, where it becomes temperature independent before dropping to zero at $T_c \approx 81$ K. The same sample was subjected to another low oxygen anneal cycle (5 hours at 345°C, followed by a 12-hour ramp to 25°C, all at ~10 mTorr O_2), after which the resistivity (curve C) increased by a factor of 3 from the original high oxygen concentration state at room temperature. Here the ab-plane resistivity exhibits a semiconductive upturn starting at ~250 K and continuing down to $T_c \approx 62$ K. Once again, the sample was subjected to another low oxygen anneal cycle (5 hours at 375°C, followed by a 12-hour ramp to 25°C, all at ~10 mTorr O_2), after which the resistivity (curve D) showed a total increased by an order of magnitude with respect to sample "A", with semiconductor-like behavior observed between room temperature and $T_c \approx 25$ K. The inset shows the resistivity data of curve D replotted as $\ln\rho/\rho_o$ vs 1/T, where ρ_o is the room-temperature resistivity. Simply activated behavior is not observed, hence the resistivity differs quantitatively from true semiconducting behavior.

Figure 3.3 (a) shows the Hall coefficient (measured simultaneously with the resistivity), following the successive anneal cycles described above. The symbols correspond to those of the resistivity specimens, in Fig. 3.3 (b). For all oxygen configurations, the Hall coefficient grows as the temperature is decreased, down to about 100K below which superconducting fluctuation effects dominate. At fixed temperature, the general trend is that a decreased oxygen content increases the Hall coefficient. R_H shows an increase by a factor of 2.9 from the high oxygen anneal cycle (curve A) to the

extreme low oxygen anneal cycle (curve D) at room temperature. Using the expression $R_H=1/nec$, we find at room temperature an effective hole concentration $n=3.02\times10^{21}cm^{-3}$ for the high oxygen specimen (curve A), and $n=1.05\times10^{21}cm^{-3}$ for the low oxygen specimen (curve D). Normalized to the unit cell volume ($5.3995 \times 5.4572 \times 30.7236$ $Å^3$), this corresponds to $n_H=2.73$ and 0.951 holes per unit cell, for the high and low oxygen specimens, respectively.

The dramatic difference in the ab-plane resistivity and Hall coefficient observed in Fig. 3.3 for the different specimens of $Bi_2Sr_2CaCu_2O_{8-x}$ is directly related to oxygen configuration. Although we were not able to non-destructively determine the actual oxygen content of the different specimens within a resolution greater than $x=0\pm0.1$ (using weight loss and Rutherford backscattering), from previous studies[4,5] we estimate a value of $x\approx0.08$ after the extreme low oxygen anneal cycle. Structural single-crystal x-ray studies on similar crystals showed the presence of stacking faults, but no secondary phases (independent of the oxygen configuration).

Previous Hall effect measurements in $YBa_2Cu_3O_{7-\delta}$ (Refs. [6] and [7]) suggest a Hall number ($\sim1/R_H$) proportional to temperature T. A similar relation has been suggested for Bi-Sr-Ca-Cu-O and $Tl_2Ca_2Ba_2Cu_3O_x$ ceramics.[8] Figure 3.4 shows the inverse Hall coefficient $1/R_H$ plotted versus T for the four different oxygen configurations. The plot indicates, for all four specimens, good agreement with the expression

$$1/R_H = \gamma + \beta T \tag{3.3}$$

where γ and β are constants. As the oxygen deficiency is increased, the zero temperature offset γ is reduced from 0.2×10^3 C/cm^3 toward zero, and the slope β decreases from 0.920 C/cm^3K to 0.480 C/cm^3K.

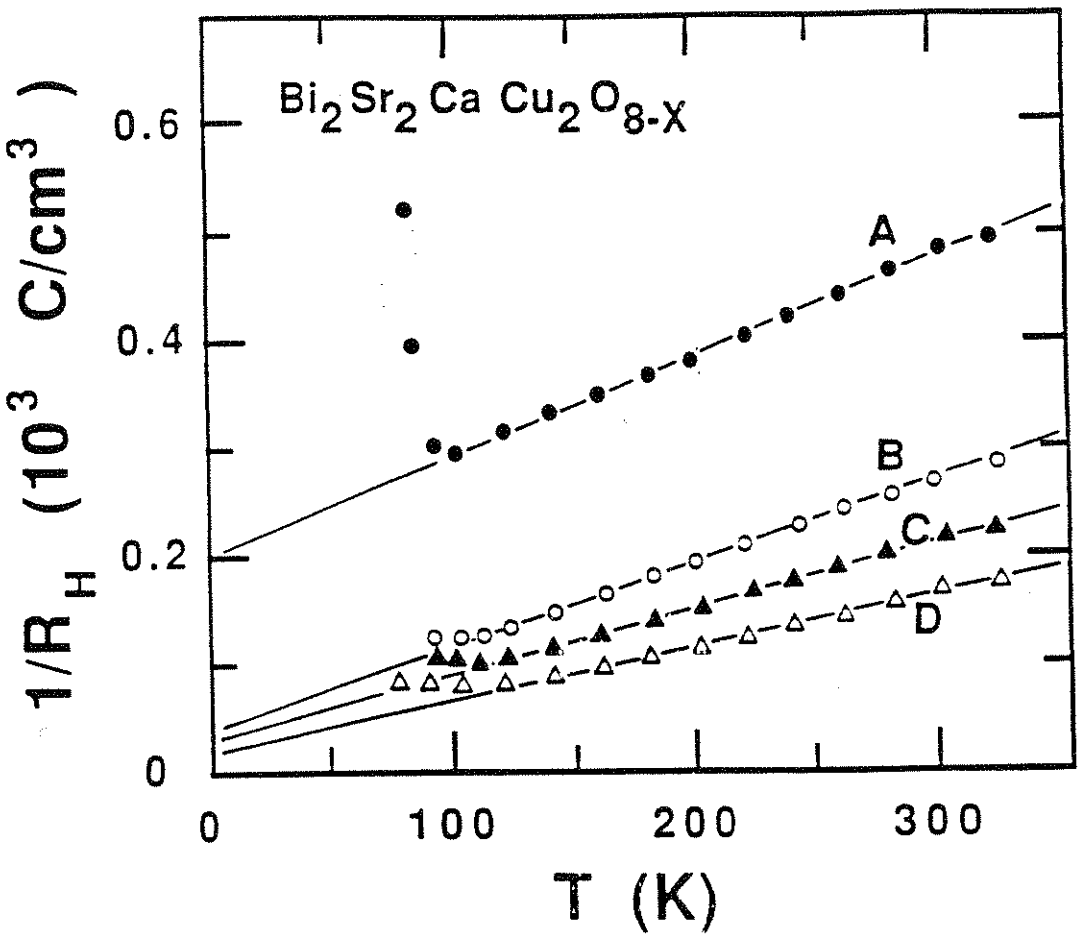

Figure 3.4. $1/R_H$ for ab-plane of $Bi_2Sr_2CaCu_2O_{8-x}$ showing good agreement with a linear fit (solid line) to the data above T_c for different oxygen configurations. The $1/R_H$ data can be converted to Hall number n_H(holes per unit cell) by multiplying by 5.63×10^{-3} cm^3/C.

Figure 3.5 shows the Hall mobility μ_H extracted from the Hall coefficient and ab-plane resistivity measurement for the four different oxygen configurations. We see that the Hall mobility decreases as oxygen is depleted from the sample and the specimen becomes more insulating. For high-oxygen (metallic) samples (curves A and B) the mobility is very temperature dependent (behaving roughly as 1/T), while for low oxygen content (curve D) μ_H appears to saturate and becomes roughly temperature independent. This decrease in temperature dependence of the Hall mobility as oxygen is removed coincides with what one might expect for a system undergoing increased localization

The resistivity and Hall data of Fig. 3.3, and Eq. (3.3) in particular, are not generally consistent with simple metallic (band) behavior. Nevertheless, we briefly examine the consequences of a simple metallic transport model which allows evaluation of characteristic fundamental parameters. The temperature dependent resistivity $\rho_{e\text{-}ph}(T) = m^*/ne^2\tau_{e\text{-}ph}(T)$ relates the carrier concentration n and scattering time $\tau_{e\text{-}ph}$. At sufficiently high temperature, $\tau_{e\text{-}ph}$ varies inversely with T and is related to the transport electron-phonon coupling parameter λ_{tr} by $h/2\pi\tau_{e\text{-}ph} = 2\pi\lambda_{tr}k_BT$. λ_{tr} is a good estimate of λ which determines T_c in the Eliashberg theory. The most metallic sample (curve A) in Fig. 3.3 has a resistivity slope 1.46 $\mu\Omega$-cm/K. Combining this with the room temperature $n = 3.02 \times 10^{21}$ cm^{-3}, we estimate $\tau_{e\text{-}ph} = 0.62\text{x}10^{-12}(m^*/m)T^{-1}$ (sec·K) and $\lambda_{tr}=1.95$ (m/m^*) for the high oxygen specimen. Within conventional BCS electron-phonon superconductor theory, an electron-phonon coupling parameter of this order is not unreasonable for the observed T_c of 85 K.

Numerous other transport models have been suggested for the high T_c oxides. Two-band models[9,10] are problematical in that the observed temperature dependence of R_H restricts too severely the band parameters,[11] and in a way inconsistent with pressure studies[12] (at least for $YBa_2Cu_3O_7$). Strong electron-electron interaction effects can lead to the opening of a soft coulomb gap at E_F,[13,14] with a resulting resistivity $\rho \sim \exp[T_o/T]^{1/2}$.

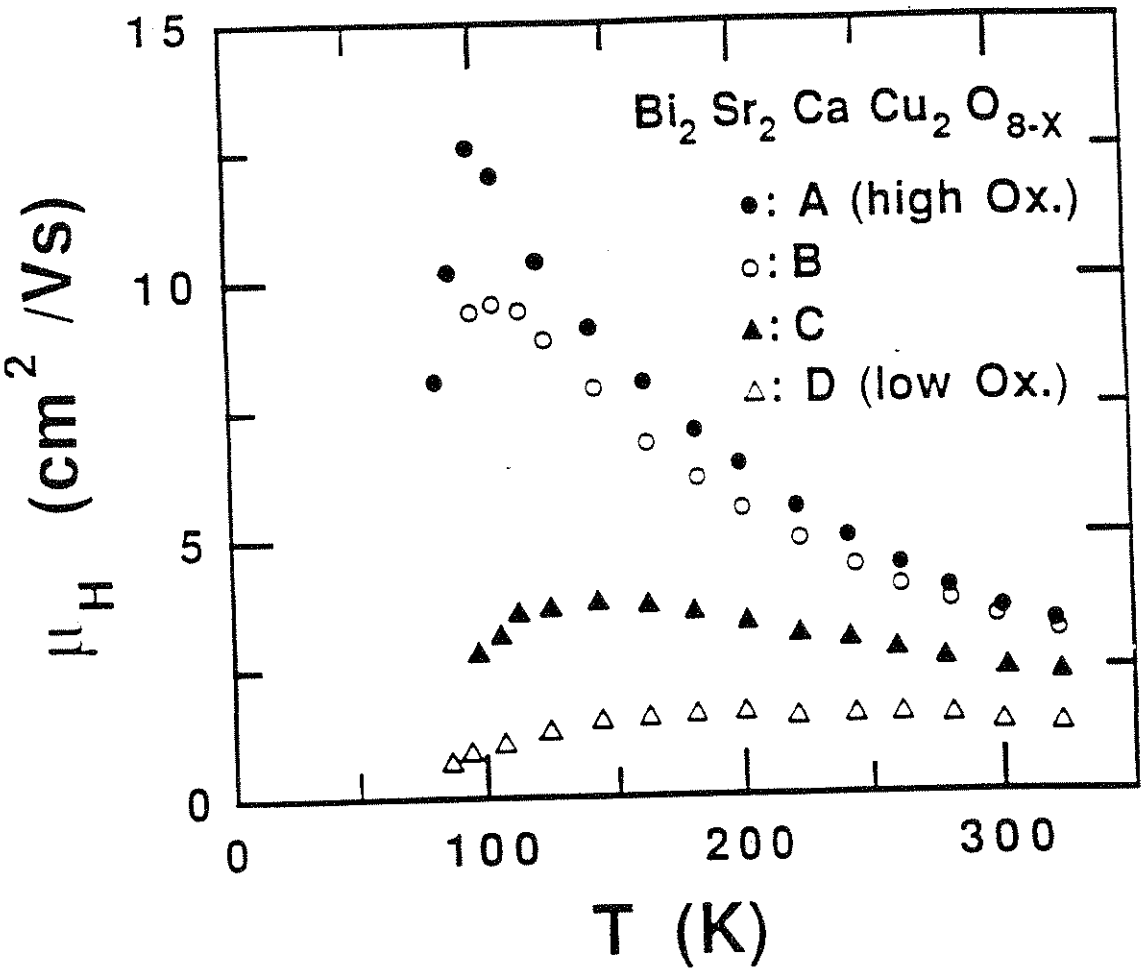

Figure 3.5. Hall mobility for ab-plane of $Bi_2Sr_2CaCu_2O_{8-x}$ crystals for different oxygen cofigurations. μ_H depends strongly on temperature for high oxygen annealed sample and becomes temperature independent after the low oxygen anneal cycle.

In two dimensions, additional disorder leads[15] to a scaling between the fractional increase in ρ and the fractional increase in R_H: $\delta R_H/R_H = 2\delta\rho/\rho$. At relatively low temperatures, curves C and D in Fig. 3.3 (b) do roughly follow such an exponential temperature dependence, but we fail to find a scaling with R_H. Hence, we rule out the coulomb gap behavior in this parameter range of $Bi_2Sr_2CaCu_2O_{8-x}$. Another model, used previously[16] to interpret resistivity and Hall data for insulating La_2CuO_4, is that of a doped semiconductor. However, the conductivity and Hall coefficient for this process are both simply activated, in contrast to our findings for $Bi_2Sr_2CaCu_2O_{8-x}$ here. We also note that the thermoelectric power of $Bi_2Sr_2CaCu_2O_{8-x}$ was shown previously[1] to obey the expression S=A+BT, with A and B constants (A depends on oxygen configuration). This expression is also obtained for small polaron hopping transport, and has been applied to the boron carbides.[17] However, the predicted Hall coefficient for polaron hopping is not consistent with Eq. (3.1) and the data of Fig. 3.3(a). Finally, Anderson[18] has proposed that the T^2 dependence of the $\cot(\theta_H)=\rho_{ab}/R_H$(ab-plane), measured by Ong *et al.*,[19] in Zn doped $YBa_2Cu_{3-x}Zn_xO_7$, is a strong evidence for the two-dimentional Luttinger liquid nature of the electron system in this class of materials. However, it is obvious that the $Bi_2Sr_2CaCu_2O_{8-x}$ system does not exhibit such temperature dependence, since $R_H \sim 1/T$ but ρ_{ab} goes from ~T to ~1/T as the oxygen configuration of the sample is depleted.

We have previously demonstrated that in $Bi_2Sr_2CaCu_2O_{8-x}$ (Ref. 1) and $YBa_2Cu_3O_{7-\delta}$ (Ref. 20) the resistivity closely follows the empirical expression

$$\rho(T) = \rho_0 T^{\alpha} \exp[\Delta/k_B T] \qquad (3.4)$$

where α is between 0.5 and 1.0. Combining Eqns. (3.3) and (3.4) yields a mobility consistent with Fig. 3.5. The physical justification of Eq. (3.4) is not clear, but it may

arise from a quantum percolation type transport as suggested by Phillips.[21] In this context, the activated term could arise from the difference in energy between the Fermi level and low lying extended states, while the T^{α} term comes from a temperature dependent mobility.

In conclusion, the resistivity and the Hall constant of $Bi_2Sr_2CaCu_2O_{8-x}$ are extremely sensitive to oxygen configuration. Our data are not consistent with a soft coulomb gap or the 2-D Luttinger liquid lectron system. The temperature dependence of these transport coefficients follow simple empirical expressions. The Hall constant for the magnetic field applied perpendicular to the Cu-O planes is *p* type with a 1/T behavior for different oxygen configurations. The decrease in temperature dependence of the Hall mobility (deduced from Fig. 3.5) as oxygen is removed suggests that the localization in the system is increasing. This unusual behavior has also been observed in other high T_c oxides suggesting that these expressions may be inherent to the high T_c superconductors.

References:

1. M. F. Crommie, A. Y. Liu, M. L. Cohen, *et al.*, Phys. Rev. B **41**, 2526 (1990).
2. M. F. Crommie, G. Briceño and A. Zettl, Physica C **162-164**, 1397 (1990).
3. R. H. Friend and N. Bett, J. Phys. E. **13**, 294 (1980).
4. J. M. Tarascon, V. L. Page, P. Barboux, *et al.*, Phys. Rev. B **37**, 9382 (1988).
5. J. M. Tarascon, W. R. McKinnon, P. Barboux, *et al.*, Phys. Rev. B **38**, 8885 (1988).
6. Y. Iye, T. Tamegai, T. Sakakibara, *et al.*, Physica C **153+155**, 26 (1988).
7. T. Penney, S. v. Molnar, D. Kaiser, *et al.*, Phys. Rev. B **38**, 2918 (1988).
8. J. Clayhold and N. P. Ong, Phys. Rev. B **38**, 7016 (1988).
9. D. M. Eagles, Physica C **153+155**, 701 (1988).
10. Y. Lu, Y. F. Yan, H. M. Duan, *et al.*, Phys. Rev. B **39**, 729 (1989).
11. M. W. Shafter, T. Penney and B. L. Olson, in *Novel Superconductivity*, S. A. Wolf and V. Z. Kresin, Eds. (Plenum, New York, 1987), pp. 771.
12. I. D. Parker and R. H. Friend, J. Phys. C **21**, L345 (1988).
13. A. L. Efros and B. I. Shklovskii, J. Phys. C **8**, L49 (1975).
14. P. Bernstein, J. Bok and A. Zylbersztejn, Solid State Commun. **70**, 271 (1989).
15. B. L. Altshuler, P. A. Lee, D. Khmel'nitzkii, *et al.*, Phys. Rev. B **22**, 5142 (1979).
16. N. W. Preyer, R. J. Birgeneau, C. Y. Chen, *et al.*, Phys. Rev. B **39**, 11563 (1989).
17. C. Wood and D. Emin, Phys. Rev. B **29**, 4582 (1984).

18. P. W. Anderson, Phys. Rev. Lett. **67**, 2092 (1991).

19. T. R. Chien, Z. Z. Wang and N. P. Ong, Phys. Rev. Lett. **67**, 2088 (1991).

20. M. F. Crommie, A. Y. Liu, A. Zettl, *et al.*, Phys. Rev. B **39**, 4231 (1989).

21. J. C. Phillips, *Physics of High-T_c Superconductors* (Academic, Boston, 1989).

Chapter 4

c-axis Magnetoresistance

4.1 Introduction

The Meissner effect, i.e. complete expulsion of a magnetic field, is a property that all superconductors exhibit at low magnetic fields. Superconductors exhibit perfect diamagnetism. When the magnetic field is increased in the Meissner phase two things can happen depending on the ratio, κ, of the characteristic magnetic field penetration length (London penetration depth, λ_L) and the characteristic length over which the wavefunction of the superconductor decays (coherence length, ξ). If κ is less than $1/\sqrt{2}$ (type I superconductor), the superconductor will be driven normal when the magnetic field is increased beyond a critical field $H_c(T)$, at which it is energetically more favorable to let the magnetic field completely penetrate the material than to continue the field expulsion. However, if the ratio is greater than $1/\sqrt{2}$ (type II superconductor), a solution to the macroscopic mean field Ginzburg-Landau equations[1] due to Abrikosov indicates that the magnetic field will partially penetrate the material, which remains a superconductor, when it is increased beyond a critical field $H_{c1}(T)$. The type-II superconductor allows the magnetic field to penetrate in small regions, of radius λ_L, and their centers, of radius ξ, are driven from superconducting to the normal state. Each small region (vortex) contains a quantum of magnetic flux $\Phi_0 = hc/2e = 2\times10^{-7}$ gauss cm^2. The vortices are arranged in a triangular lattice throughout the material, the so called Abrikosov flux lattice, with a separation between the normal cores given by $(\Phi_0/H)^{1/2}$. If the magnetic field is increased further, the whole material becomes normal when a second critical field, $H_{c2}(T)$, is surpassed. For fields H such that $H_{c1} < H < H_{c2}$ the superconductor is said to be in the vortex state, also known as the mixed state. Type-II superconductors tend to be alloys,

including all the oxide superconductors, or transition metals with high values of electrical resistivity in the normal state.

The transport properties of a type II superconductor in the mixed state can be very different than in the Meissner state. For example, if an electric current is passed through the superconductor in the mixed state the vortices feel a Lorentz force proportional to $\mathbf{J}\times\mathbf{H}$. This Lorentz force can give rise to dissipation of energy if the vortices are allowed to move. The motion of the vortices will generate an electric field along the direction of the current proportional to $\mathbf{v}\times\mathbf{H}$, where $\mathbf{v}$ is the velocity of the vortices. Usually, the vortices are pinned by defects in the material, i.e. regions where the amplitude of the superconducting wavefunction is smaller. However, if the local current is increased, i.e. the local Lorentz force is increased, depinning of a vortex will occur when a local critical current I_c is surpassed, provided such a current is less than the intrinsic Ginzburg-Landau critical depairing current. If the pinning force strength is more or less uniform throughout the material , all the vortices will move when the pinning force is overcome, giving rise to "flux flow" dissipation. According to the model of Bardeen and Stephen[2,3] dissipation occurs as a result of the transport current passing through the normal cores resulting in the superconductor manifesting a longitudinal resistivity given by,

$$\rho_f = \rho_n(T)\, H/H_{c2}(T) \qquad (4.1)$$

where $\rho_n(T)$ is the normal state resistivity. In the other extreme, the case of a wide distribution of pinning strengths, the flux creep model proposed by Anderson and Kim[4,5] describes the depinning of the vortices in terms of the Lorentz force and the thermal motion of the vortices. The flux creep model predicts a thermally activated resistivity given by

$$\rho_f \propto \exp(-U_{pin}/kT) \qquad (4.2)$$

where U_{pin} is an "average" of the pinning potential. Numerous studies have interpreted their results as evidence for both types of dissipation in the high T_c oxides for some orientations of field and current. For instance, Dover *et al.*,[6] explain their measurements of the ab-plane magnetoresistivity of $Bi_2Sr_2CaCu_2O_8$ at low fields in terms of flux flow, while Palstra *et al.*,[7] interpret the same kind of measurements in the same material, but in stronger magnetic fields, as a manifestation of thermally activated flux creep.

The above models of dissipation depend on the presence of a Lorentz force ($\sim \mathbf{J}\times\mathbf{H}$), which implies that the dissipation is proportional to $\sin^2\theta$, where θ is the angle between **H** and **J**. However, experimentally the dissipation in the high T_c oxides exhibits little (e.g.$YBa_2Cu_3O_7$)[8] or no dependence at all (e.g.$Bi_2Sr_2CaCu_2O_8$)[9] when both the current and the magnetic field are perpendicular to the copper oxide planes. To explain this behavior, P. H. Kes *et al.*,[10] have suggested, based on the intrinsic anisotropy of these layered materials, that the observed dissipation is due to the motion of "pancake vortices". These vortices are a result of the distortion of the conventional Abrikosov flux lines when a magnetic field is applied *perpendicular* to the CuO planes. Such a distortion is due to the anisotropies in the coherence length and the London penetration depth between the direction parallel to the CuO planes and perpendicular to them. A small misalignment of $\mathbf{H}\|ab$ gives rise to "pancake vortices"($\|c$) which would then interact with the transport current $\mathbf{J}\|ab$ via a Lorentz force to yield the θ independent dissipation. Some other models have been advanced to explain this effect, including curved flux lines[11], flux entanglement[12], thermodynamic fluctuations[9,13], and Josephson junction networks[14].

If one accepts that only the motion of the "pancake vortices" give rise to dissipation, then one is naturally led to inject the transport current along the c-axis

(creating a zero macroscopic Lorentz force on the vortices) and one does not expect to see any dissipation independent of the magnetic field direction. To observe this effect we measured several $Bi_2Sr_2CaCu_2O_8$ samples with various field orientations and the current J||c. The measurements where made in an American Magnetics superconducting solenoid capable of producing dc magnetic fields up to 8 T.

4.2 c-axis magnetoresistance with H||c.

We measured the c-axis dc electrical resistivity, $\rho_c(T,H)$, of single crystals of $Bi_2Sr_2CaCu_2O_8$ in magnetic fields up to 7T oriented parallel to the applied current. We find that when the magnetic field is oriented along the current direction (H||c, i.e. absence of a Lorentz force), the c-axis resistivity, $\rho_c(T,H||c)$, of $Bi_2Sr_2CaCu_2O_8$ exhibits a huge magnetoresistance at temperatures below $T_c(H=0)$. This phenomenon is manifested as an *apparent* severe depression of the superconducting onset temperature (≈30K at 7T) followed by a broadening of the resistive transition. This behavior is in sharp contrast to the well known ab-plane behavior, $\rho_{ab}(T,H||c)$, for which there is a strong depression of the zero resistivity point but the onset of superconductivity is hardly depressed[7].

High purity single crystals of $Bi_2Sr_2CaCu_2O_8$ with average dimensions of 1mm × 1mm × 0.01mm were prepared by standard methods[15]. Low resistance contact was made to the samples using fired on silver pads. The c-axis resistivity was measured using a concentric ring contact configuration[16] and nominal current density of 0.17 A/cm^2, unless otherwise noted. As an added check, $\rho_c(T,H=0)$ was also measured simultaneously with ρ_{ab} using a modified Montgomery contact configuration [17], with essentially the same results.

Figure 4.1(a) shows $\rho_c(T,H||c)$ for a $Bi_2Sr_2CaCu_2O_8$ crystal for selected magnetic fields 0T, 0.5T, 3.5T and 7T oriented parallel to the c-axis. In zero field, the resistive

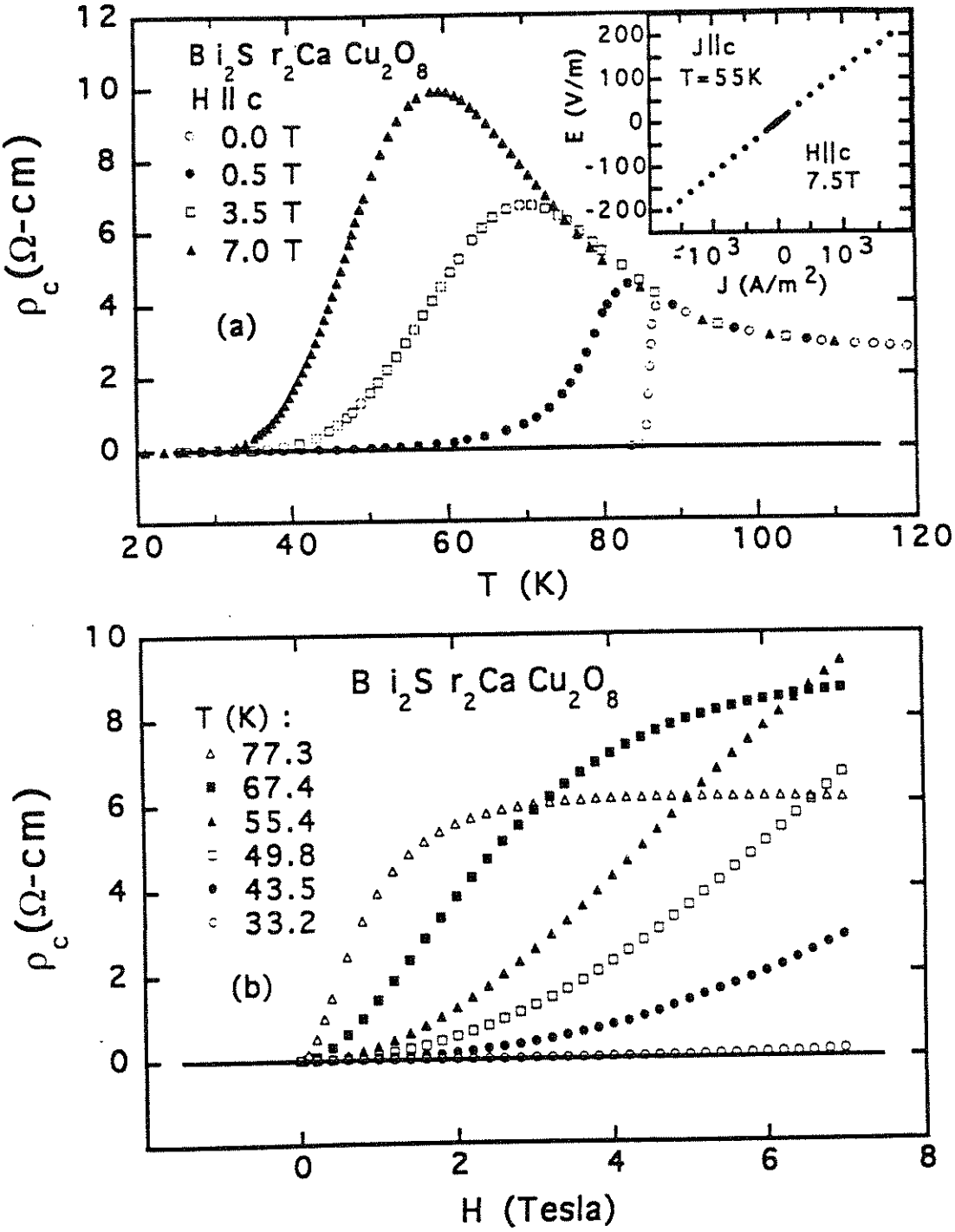

Figure 4.1 (a) The resistive transition $\rho_c(T,H\|c)$ of $Bi_2Sr_2CaCu_2O_8$ single crystal for various values of the field, and (b) $\rho_c(H)$ at selected temperatures for H||c up to 7.0T. The current density was 0.17 A/cm^2. The inset shows a typical I-V for this configuration.

transition is sharp with a midpoint T_c=85K and a width of ΔT_c<2K. The application of a magnetic field causes ρ_c(T,H=const.) to apparently continue its normal-state "semiconductor-like" behavior with a concomitant depression of the onset transition temperature, followed by a broad resistive transition. The temperature interval over which ρ_c(T,H=const.) continues its semiconductor-like trend increases as the magnetic field increases.

In the inset of Fig. 4.1(a) we show a typical current-voltage (I-V) characteristic for $Bi_2Sr_2CaCu_2O_8$. Experimentally, the I-V's are found to be linear at low current density and high temperature, though they deviate from linearity at the lowest temperatures and highest currents.

Figure 4.1(b) shows the magnetic field dependence of the out-of-plane resistivity, ρ_c(T=const., H||c), at selected temperatures, for magnetic field up to 7T. At low temperatures ρ_c exhibits positive curvature as it smoothly increases with magnetic field. At higher temperatures the slope of ρ_c(T=const., H||c) becomes steeper at low fields and its curvature is observed to become negative. At temperatures close to the zero field transition temperature, ρ_c(T=const., H||c) becomes independent of magnetic field at the highest fields tested, i.e. it exhibits saturation. We also note that high temperature and low temperature curves are found to cross over at a particular value of magnetic field; larger temperature differences between the curves lead to higher values of this "crossing" magnetic field.

The apparent depression of T_c displayed in Fig. 4.1(a) cannot simply be accounted by the suppression of superconductivity at H>H_{c2}(||c) since -$dH_{c2||}$/dT is 0.75 to 1.4 T/K obtained from ab-plane transport measurements[6,18]. The -$dH_{c2||}$/dT implied by Fig. 4.1(a) is ≈0.2 T/K.

Other mechanisms based upon a Lorentz force[16] are considered unlikely due to the geometry of this experiment. In Ref. 16 it was argued that the origin of the c-axis dissipation in this configuration is thermally activated phase slip across weak links threading the sample. Figs. 4.2(a)and 4.2(b) show the theoretical fits of the data shown in Fig. 4.1 to the expression for the resistivity of a weak link at finite temperature[16,19]:

$$\rho_c = \frac{\rho_n(T)}{\left\{ I_0\left(\frac{\hbar}{2e\,kT} \; J_c(0)\left[1-\frac{T}{T_c}\right]^{3/2} \; \frac{\Phi_0}{H} \right)\right\}^2} \quad . \tag{4.3}$$

Where I_0 is the zeroth order modified Bessel function. The normal resistivity has been approximated by the empirical expression[17]

$$\rho_n(T) = \rho_0 \quad T^{0.7} \quad e^{\Delta/k_B T} \tag{4.4}$$

Where ρ_0=0.00947Ω−cm and Δ/k_B=268.406K, and the critical current of a superconducting weak link of area $A=\Phi_0/H$ has been rewritten as

$$I_c = J_c\, A = J_c(0)\left(1-\frac{T}{T_c}\right)^{3/2} \; \frac{\Phi_0}{H} \tag{4.5},$$

where J_c is the intrinsic Ginzburg-Landau depairing critical current density. T_c=85K is assumed to be field independent.

With ρ_0 and Δ fixed by data taken at zero field (H=0T, T_c=85K), $J_c(0)$ becomes the only free fitting parameter for the data taken below T_c in the mixed state. The data are

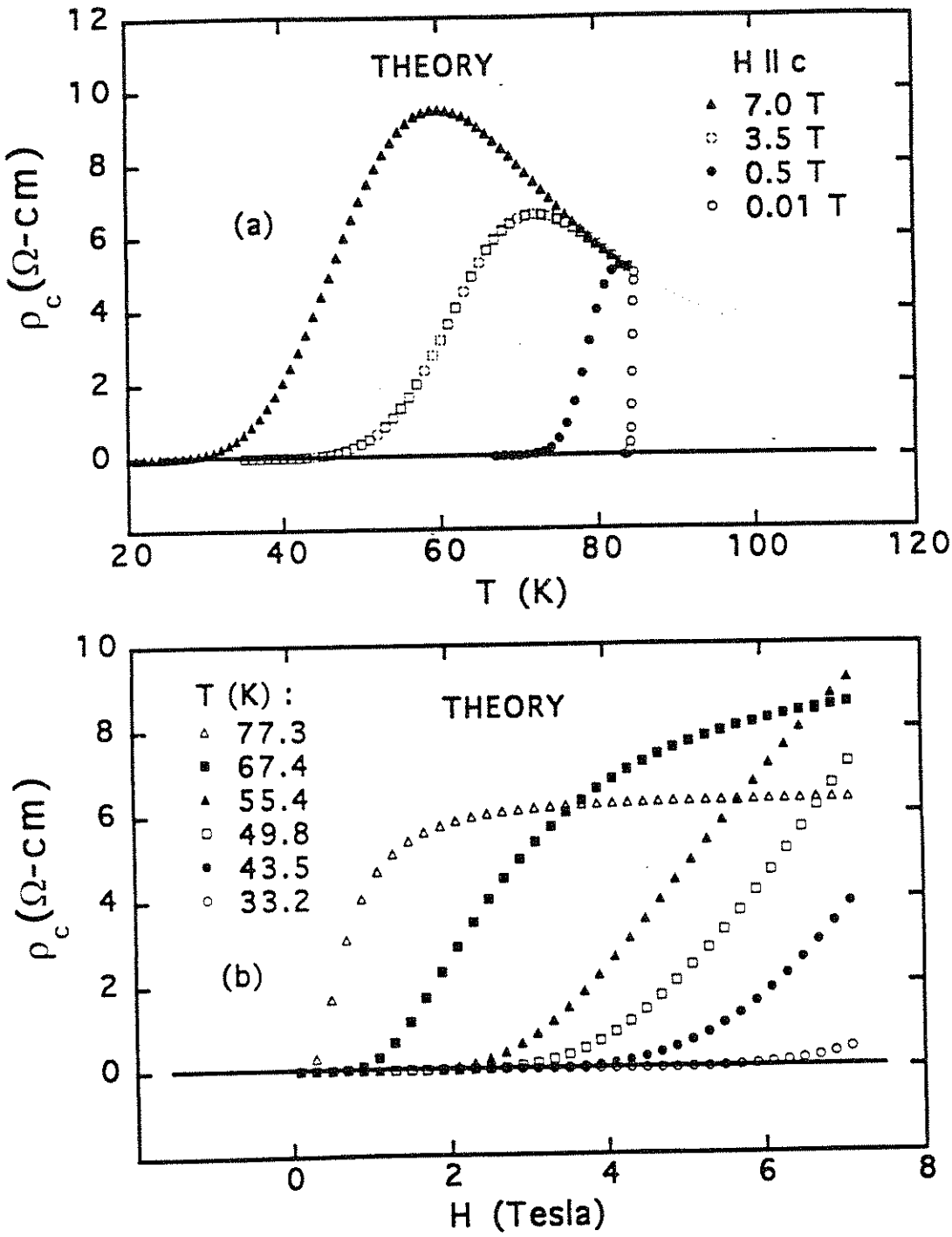

Figure 4.2 (a) Equation (5.3) fitted to $\rho_c(T<T_c,H\|c)$ data in Fig.5.1(a) with $J_c=5.08\times10^6$ A/cm^2 (see text). $\rho_n(T>T_c)$ is also shown. (b) Fitted $\rho_c(H)$ curves with the same parameters.

best fit with $J_c(0)=5.1\times10^6 A/cm^2$. As expected, our deduced value of the intrinsic *depairing* critical current density is significantly larger than the experimentally determined c-axis critical current density, $J_{c(exp)}(0)=4.7\times10^4 A/cm^2$ (Ref. 20). From our determined $J_c(0)$, we may extract the London penetration depth[1]

$$\lambda_c=\left(\frac{c\,\Phi_o}{12\pi^2\sqrt{3}\;\xi\;J_c(0)}\right)^{1/2} \qquad (4.6)$$

Combining $J_c(0)=5.1\times10^6 A/cm^2$ with $\xi=38\times10^{-4}$ μm (Ref. 20) we find $\lambda_L=0.72\mu m$. This value is intermediate to the two other values of the London penetration depth for $Bi_2Sr_2CaCu_2O_8$ reported in the literature: A. P. Malozemoff *et al.*,[21] find $\lambda_L=.3\text{-}.6\mu m$, while B. D. Biggs *et al.*,[20] report $\lambda_L=7\mu m$.

The theoretical curves in Fig. 4.2 are found to describe the apparent depression of T_c very well, and agree quantitatively with the experimental data at high fields and high temperatures. The extra dissipation observed experimentally at low temperature and low magnetic field may be due to sample inhomogeneities, not taken into account by the theory.

We also remark that other models[22,23] have been suggested to account for the $\rho_c(T,H\|c)$ behavior. R. Ikeda *et al.*,[22] proposed an order-parameter fluctuation theory that also gives reasonable fits[22] to a subset of our experimental data. More recently, K. E. Gray and D. H. Kim[23] modeled the c-axis conduction as a series stack of Josephson tunnel junctions. For a fixed magnetic field, this model provides a single explanation to the low temperature, broad transition and the high temperature "semiconducting-like" behavior with only two fitting parameters. However, the parameters are field dependent,

i. e. in order to fit the data of Fig. 4.1 (b) a continuous range of values are required for the parameters.

4.3 c-axis magnetoresistance with H⊥c.

In this section we report the measurement of the out-of-plane resistivity for magnetic field oriented perpendicular to the current direction, $\rho_c(T,\mathbf{H}\perp\mathbf{c})$, of the same $Bi_2Sr_2CaCu_2O_8$ crystal. and the functional form of $\rho_c(T,\mathbf{H}\perp\mathbf{c})$ is strongly dependent on the magnitude of the c-axis transport current.

The results of such a measurement are shown in Fig. 4.3 for magnetic fields 0T, 0.5T, 3.5T, and 7.0T. In the presence of a magnetic field, $\rho_c(T,\mathbf{H}\perp\mathbf{c})$ behaves similarly to $\rho_c(T,H\|c)$, i.e. it continues its semiconductor-like behavior for a few degrees below the $T_c(H=0)$, until it turns over and displays a broadened transition to zero resistivity. In fact, it is tempting to interpret $\rho_c(T,\mathbf{H}\perp\mathbf{c})$ as resulting from a slight misalignment of the magnetic field since $\rho_c(T,\mathbf{H}\perp\mathbf{c}=7.0T)$ closely resembles $\rho_c(T,H\|c=0.5T)$. As we demonstrate below, however, this is not the case.

To investigate a possible "scaling" of $\rho_c(T)$ curves for different H-field orientations, I-V characteristics were examined for the configuration ($\mathbf{H}\perp\mathbf{c}$, $\mathbf{J}\|\mathbf{c}$,i.e., $\mathbf{H}\perp\mathbf{J}$). Figure 4.4 shows the broadening of the resistive transition for various current densities ranging from 1.7×10^{-5} to 0.17 A/cm^2, at a fixed magnetic field (H=7.5 T). $\rho_c(T,\mathbf{H}\perp\mathbf{c})$ is independent of probing current density at temperatures close to T_c. However, as the temperature is lowered, $\rho_c(T,\mathbf{H}\perp\mathbf{c})$ displays an increasing dependence on the measuring current density. Smaller probing currents result in lower resistivity, with a subsequent narrowing of the resistive transition. A typical I-V characteristic is shown in the inset of Fig. 4.4, where *threshold* behavior can be observed, i.e. no dissipation is detected until the current exceeds a critical current. This threshold behavior

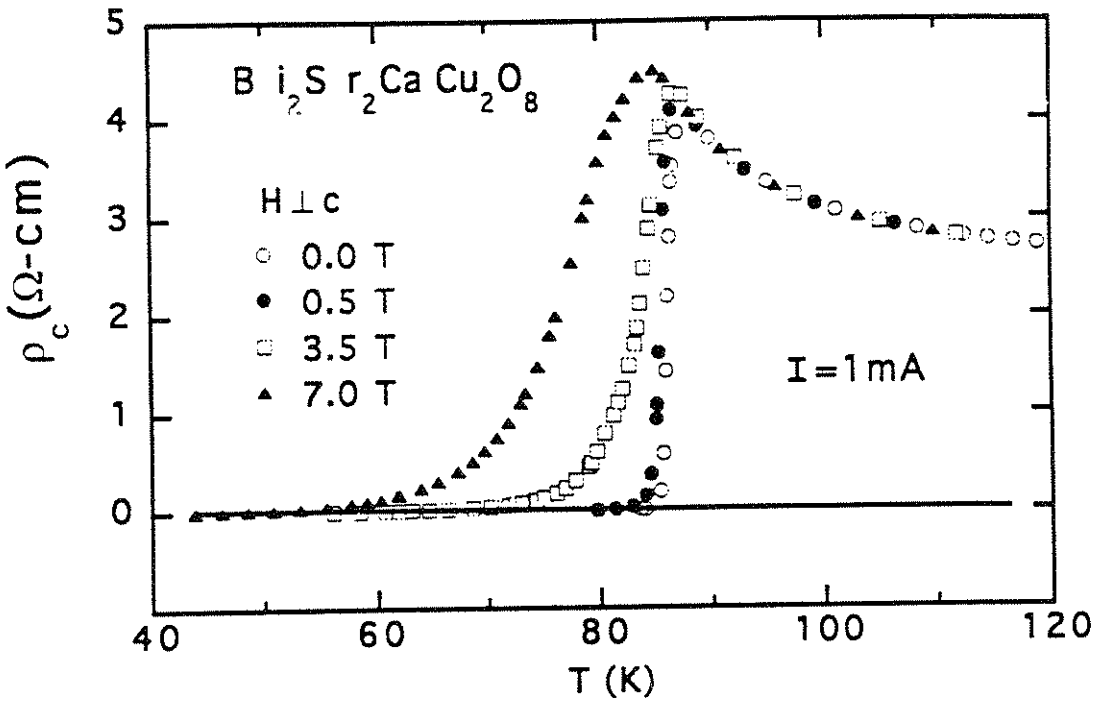

Figure 4.3 The resistive transition $\rho_c(T,\mathbf{H}\perp\mathbf{c})$ of $Bi_2Sr_2CaCu_2O_8$ for selected values of $\mathbf{H}\perp\mathbf{c}$, and current density 0.17 A/cm^2.

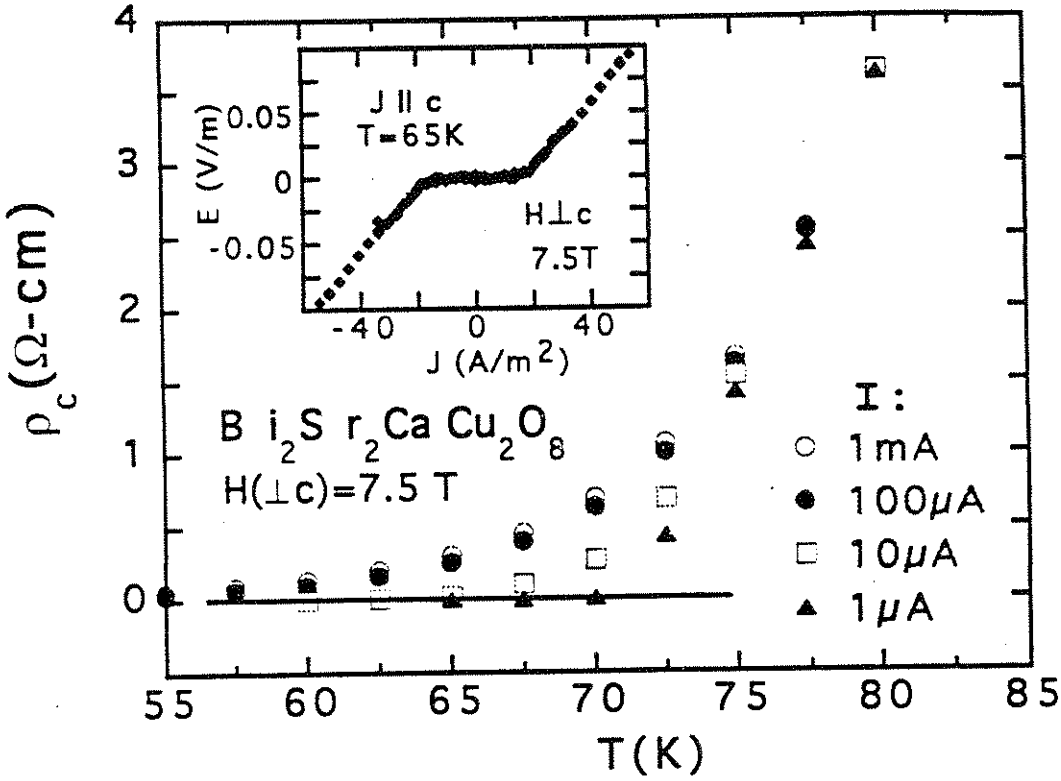

Figure 4.4 Dependence of $\rho_c(T,\mathbf{H}\perp\mathbf{c})$ on measuring current, for H=7.5T, solid lines are a guide to the eye. The current density is given by J=170×I A/cm^2. The inset shows a typical I-V for this configuration.

rules out the scaling, i.e. misalignment hypothesis, since **H**∥c yields only linear I-V characteristics (inset to Fig.4.1(a)).

Figures 4.5(a) and (b) show the normalized I-V characteristics, vertically offset for clarity, of the same sample shown in Fig. 4.3, with H=7.5T and 4.0T⊥c, respectively. While the I-V's all become linear at high currents and high temperature, the I-V's for T≤73K (T≤78K) show a nonzero critical current, J_c, for temperatures up to T~73K (T~78K) in a 7.5T (4.0T) magnetic field. We note that the threshold current decreases with increasing temperature and increasing magnetic field.

To account for $\rho_c(T,\mathbf{H}\perp\mathbf{c})$ and $\mathbf{J}_{threshold}$ we need to consider the presence of a finite Lorentz force. In such circumstances, an expression similar to Eq.(4.3) has been used to explain the broadening of the ab-plane resistive transition[24]. Flux creep models[7] have also been advanced. However, both are unable to account for the existence of a critical depinning current, since they both predict ohmic I-V characteristics in the low current regime. We also attempted to fit the $\rho_c(T,H)$ data to the original Bardeen-Stephen expression for flux flow resistivity[3] given by Eq. (4.1), where now $\rho_n(T)$ is the normal state resistivity obtained from Eq.(4.4). Eq.(4.1) yields a $\rho(T,\mathbf{H}\perp\mathbf{c})$ that has a positive slope with respect to temperature for $T\le T_c$. Experimentally, however, $\rho_c(T,\mathbf{H}\perp\mathbf{c})$ displays a negative slope near T_c for all $H\neq 0$. We also note that just below T_c the measured resistivity does not scale with H as expected from Eq.(4.1).

It is hard to reconcile the existence of a threshold current in the geometry **J**⊥**H** with the lack of one in the orientation **J**∥**H**. One possibility is to consider Abrikosov vortices to be more strongly pinned when **H**⊥**c** than when **H**∥c. However, Feinberg and Villard[25] have investigated theoretically the pinning properties of Abrikosov vortices in a layered superconductor. They find that, for **J**∥c, Abrikosov vortices with **H**⊥**c** are very weakly pinned with respect to motion parallel to the superconducting planes. The vortices lie between the planes, in a region where the superconducting order parameter is

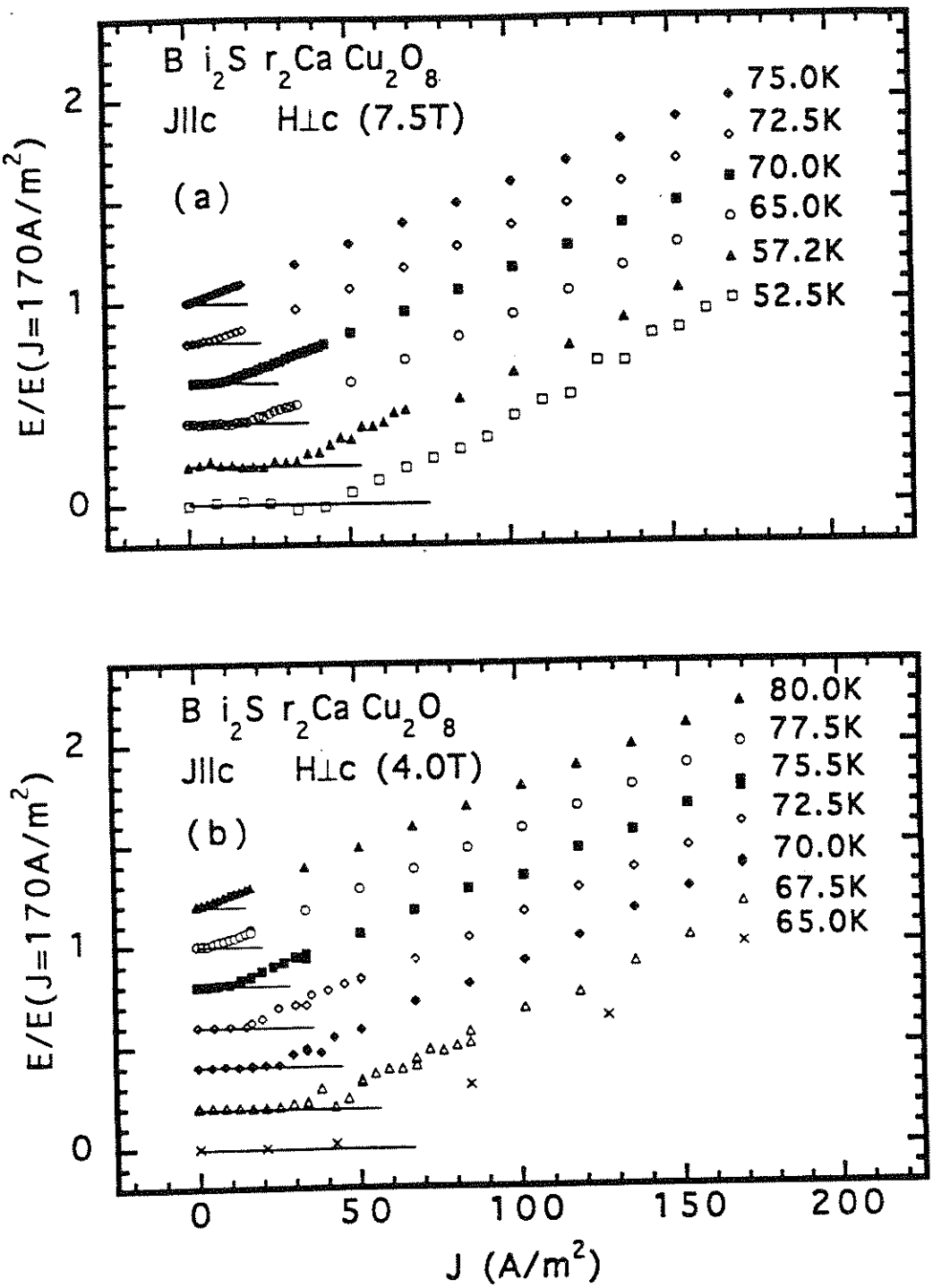

Figure 4.5 c-axis IV characteristics for H=7.5T (a) and 4.0T (b) applied perpendicular to **c**. solid lines represent zero voltage (see text).

depressed. For this reason, the core-pinning energy of the vortices is very low when they pin to defects between the planes. On the other hand, a vortex that pierces the planes (**H**||**c**) has a much higher core-pinning energy when it pins to a defect in the superconducting plane, where the superconducting order parameter is substantially greater than between the planes. Recent picovoltmetry measurements in $Bi_2Sr_2CaCu_2O_8$ (Ref. 26) with **J**⊥**c** and **H**||**c** (i.e. Abrikosov vortex motion parallel to the CuO planes) yielded only linear I-V characteristics. We interpret these results as evidence that Abrikosov vortex motion is not responsible for the observed threshold behavior.

Another possibility is the existence of Josephson vortices for **H**⊥**c**, and that the threshold currents observed in the I-V characteristics signal the onset of sliding of Josephson vortices along the ab-plane[27]. Kleiner *et al.*,[28] have recently shown that $Bi_2Sr_2CaCu_2O_8$ is a weakly-Josephson-coupled layered superconductor, and it has been shown theoretically that a Josephson vortex lattice (from the **H**⊥**c** component) and an Abrikosov vortex lattice (from the **H**||**c** component) coexist in such a superconductor[29]. In this scenario, each coreless Josephson vortex has a width=$\Phi_o/H_{||}d$, where d is the distance between superconducting layers and $H_{||}$ is the component of **H** parallel to the ab-plane. A Josephson vortex in a pinning potential remains pinned as current is increased until the Lorentz force on the vortex overcomes the defects pinning force[30] resulting in an I-V characteristic displaying threshold behavior. This threshold current is expected to decrease as a function of applied the magnetic field since a stiffer Josephson vortex lattice would allow the vortices to "ride" over pins with less difficulty, as observed experimentally in Fig. 4.5. This model deserves further testing.

Finally, we note that $\rho_c(T,\mathbf{H}\perp\mathbf{c})$ measurements similar to those described above for $Bi_2Sr_2CaCu_2O_8$ have been performed on $YBa_2Cu_3O_7$ (Ref. 31) in a restricted temperature range close to T_c. A melting line is identified. At temperatures above T_m, the dissipation is ohmic, while below T_m the normalized resistivity versus scaled temperature

follows a universal curve independent of H. From our $\rho_c(T,\mathbf{H}\perp\mathbf{c})$ measurements on $Bi_2Sr_2CaCu_2O_8$, such an interpretation could yield a melting temperature $T_m(H=7.5T)\approx 80K$ (Fig. 4.4). In Fig. 4.3, the $\rho_c(T,H=7.0T)$ data for $Bi_2Sr_2CaCu_2O_8$ show a small but noticeable kink near 80K, consistent with this identification. Whether an actual $T_m(H)$ phase boundary exists in $Bi_2Sr_2CaCu_2O_8$ is not clear at present, and its confirmation would necessitate a detailed investigation of $\rho_c(T,\mathbf{H}\perp\mathbf{c})$ near T_c in this material.

In summary, we have measured mixed state transport along the c-axis of $Bi_2Sr_2CaCu_2O_8$ for magnetic fields oriented both parallel and perpendicular to the c-direction. We see tremendous variation in the character of the c-axis transport depending upon magnetic field strength and orientation. The dissipative behavior of $Bi_2Sr_2CaCu_2O_8$ is complicated by a rich interplay of fluctuations and the possible coexistence of Abrikosov and Josephson vortices.

References:

1. M. Tinkham, *Introduction to superconductivity* (Robert E. Krieger Publishing Co., Malabar, Fl, 1980).
2. B. D. Josephson, Phys. Lett. **1**, 251 (1962).
3. J. Bardeen and M. J. Stephen, Phys. Rev. **140**, A1197 (1965).
4. P. W. Anderson, Phys. Rev. Lett. **9**, 309 (1962).
5. Y. B. Kim, C. F. Hempstead and A. R. Strnad, Phys. Rev. **131**, 2486 (1963).
6. R. B. v. Dover, L. F. Schneemeyer, E. M. Gyorgy, *et al.*, Phys. Rev. B **39**, 4800 (1989).
7. T. T. M. Palstra, B. Batlogg, R. B. v. Dover, *et al.*, Phys. Rev. B **41**, 6621 (1990).
8. M. Tinkham, Physica B **169**, 66 (1991).
9. Y. Iye, S. Nakamura and T. Tamegai, Physica C **159**, 433 (1989).
10. P. H. Kes, J. Aarts, V. M. Vinokur, *et al.*, Phys. Rev. Lett. **64**, 1063 (1990).
11. E. H. Brandt, Phys. Rev. Lett. **63**, 1106 (1989).
12. D. R. Nelson, Phys. Rev. Lett. **60**, 1973 (1988).
13. Y. Iye, T. Tamegai and S. Nakamura, Physica C **174**, 227 (1991).
14. D. H. Kim, K. E. Gray, R. T. Kampwirth, *et al.*, Phys. Rev. B **42**, 6249 (1990).
15. J.-M. Imer, F. Patthey, B. Dardel, *et al.*, Phys. Rev. Lett. **62**, 336 (1989).
16. G. Briceño, M. F. Crommie and A. Zettl, Phys. Rev. Lett. **66**, 2164 (1991).
17. M. F. Crommie and A. Zettl, Phys. Rev. B **43**, 408 (1991).

18. T. T. M. Palstra, B. Batlogg, L. F. Schneemeyer, *et al.*, Phys. Rev. B **38**, 5102 (1988).

19. V. Ambegaokar and B. I. Halperin, Phys. Rev. Lett. **22**, 1364 (1969).

20. B. D. Biggs, M. N. Kunchur, J. J. Lin, *et al.*, Phys. Rev. B **39**, 7309 (1989).

21. A. P. Malozemoff, L. Krusin-Elbaum and J. R. Clem, Physica C **162-164**, 353 (1989).

22. R. Ikeda, T. Ohmi and T. Tsuneto, Phys. Rev. Lett. **67**, 3874 (1991).

23. K. E. Gray and D. H. Kim, Phys. Rev. Lett. **70**, 1693 (1993).

24. M. Tinkham, Phys. Rev. Lett. **61**, 1658 (1988).

25. D. Feinberg and C. Villard, Phys. Rev. Lett. **65**, 919 (1990).

26. H. Safar, P. L. Gammel, D. J. Bishop, *et al.*, Phys. Rev. Lett. **68**, 2672 (1992).

27. M. F. Crommie, G. Briceño and A. Zettl, Phys. Rev. B **45**, 13148 (1992).

28. R. Kleiner, F. Steinmeyer, G. Kunkel, *et al.*, Phys. Rev. Lett. **68**, 2394 (1992).

29. S. Theodorakis, Phys. Rev. B **42**, 10172 (1990).

30. T. Yamashita and L. Rinderer, J. Low Temp. Phys. **21**, 153 (1975).

31. M. Charalambous, J. Chaussy and P. Lejay, Phys. Rev. B **45**, 5091 (1992).

Chapter 5

Thermal Magnetoconductivity

5.1 Introduction.

Since entropy can be carried by phonons and quasiparticles in a metal, the thermal conductivity κ is one of the few transport properties that has a nonzero value in both the normal and the superconducting states. Its measurement provides valuable information on the interaction of the charge carriers and phonons and their scattering by defects and impurities. If the phonon component of the thermal conductivity is negligible in the normal state, then below T_c the thermal conductivity of the material in the superconducting state is lower than in the normal state. This is due to the reduction of the quasiparticles density, which controls the electronic thermal conductivity. This is the case in some single element superconductors (e.g., Sn, Hg, In, Ta and Pb).[1,2] However, if the phonons provide a large fraction of the entropy transport in the normal state, as is the case in the alloy $Pb_{0.3}Bi_{0.7}$ (Ref. 2), then the thermal conductivity is higher in the superconducting state than in the normal state. The thermal conductivity of the high temperature superconductors has been extensively studied in the past few years,[3-6] and an anomalously large increase of the ab-plane heat conduction is invariably found as the temperature is lowered below T_c. However, no consensus has been reached on whether this phenomenon is due to the enhancement of the electron or the phonon contribution to the thermal conductivity below the transition temperature.

In a normal metal, the thermal conductivity is usually explained in the framework of the Bloch-Boltzmann transport theory. In this context, the thermal conductivity of the electrons given by

$$\kappa_e = \frac{1}{12\pi}\frac{\tau_{th,e} k_B^2 T}{\hbar}\int \frac{v_k\, v_k\, dS_F}{v_k} \quad , \tag{5.1}$$

where the integration is over the Fermi surface and the relaxation time $\tau_{th,e}$ is the average time an electron travels before transferring its entropy excess to the surrounding scatterers. In an isotropic material the Wiedemann-Franz law states that the ratio $\kappa_e/\sigma T$ is a constant, as can be seen from Eqns. (5.1) and (3.1), given by

$$\frac{\kappa_e}{\sigma T} = \frac{\pi^2}{3}\left(\frac{k_B}{e}\right)^2 = L_o \tag{5.2}$$

where it is assumed that $\tau_{el}=\tau_{th}$ and the ideal Lorenz number $L_o=2.45\ (10^{-8})$ W Ω/K^2.

In the case of a simple metal, where the electrons can be treated as a free-electron gas, Eq. (5.1) reduces to

$$\kappa_e = \frac{1}{3} v_F^2\, \tau_{th,e}\, C_e \tag{5.3}$$

where v_F is the Fermi velocity and $C_e = \frac{1}{2}\pi^2 n\, k_B^2\, T/E_F$ is electronic specific heat. Since in the free-electron gas model the electrical conductivity is given by $\sigma=nq^2\tau_{el}/m_e$, the Wiedemann-Franz law still holds with the condition $\tau_{el}=\tau_{th}$.

This requirement is fulfilled at high temperatures, $T>>\Theta_D$, when the dominant phonons have long wave-vector capable of changing the electron wave-vector in one collision by a the large amount needed to produce electrical resistance. The Wiedemann-Franz law is also valid at low temperatures, $T<<\Theta_D$, when elastic scattering from impurities dominate.

The phonon contribution to the thermal conductivity, in the context of the Bloch-Boltzmann theory, is given by

$$\kappa_p = \frac{1}{3} v^2 \int_0^{\Theta_D/T} \tau_p(x)\ C_p(x)\, dx \qquad (5.4)$$

where $x=\hbar\omega/k_BT$, the phonon velocities are assume to be the same for all polarizations, the Debye temperature Θ_D is chosen to include just 3N phonon modes, C_p is the phonon heat capacity, and τ_p is the phonon relaxation time for a specific scattering mechanism.

A method that has been used to explain experimentally measured thermal conductivities is to add the scattering rates $(\tau_{p,i})^{-1}$ for each mechanism i and obtain τ_p to insert in Eq. (5.4). This method is based on Matthiessen's rule[7], which states that the resistivities from each scattering mechanism are additive.

The total thermal conductivity of a normal metal is usually written as the sum of the electron and phonon contributions, $\kappa_T=\kappa_e+\kappa_p$.

In the next section I will describe the experimental technique used to measure the thermal conductivity of single crystal $Bi_2Sr_2CaCu_2O_8$, followed by the experimental results and conclusions.

5.2 Thermal conductivity of $Bi_2Sr_2CaCu_2O_8$ in the mixed state.

The thermal conductivity of a single crystal $Bi_2Sr_2CaCu_2O_8$ was measured using a steady-state comparative technique. This method was implemented is described in Ref.8, a resistor of 100Ω was used to generate the heat that passed through a 0.005 inch diameter constantan rod, used as a heat sensor, and the sample, which was thermally grounded to a heat sink. The temperature gradients across the heat sensor and the sample were measured with two 0.0005 inch diameter chromel-constantan differential thermocouples. The

sample was placed in a magnetic field generated by a superconducting solenoid from American Magnetics capable of producing fields up to 8 Tesla.

We here present measurements of $\kappa_{ab}(T,H)$, of single crystals of $Bi_2Sr_2CaCu_2O_8$ in magnetic fields up to 7.5T oriented parallel and perpendicular to the applied temperature gradient. As in previous studies[9,10] in high temperature superconductors (HTSC), we find that when the magnetic field is oriented perpendicular to ab-plane ($\mathbf{H}\|c$), the ab-plane thermal conductivity, $\kappa_{ab}(T,\mathbf{H}\|c)$, of $Bi_2Sr_2CaCu_2O_8$ exhibits a decrease in the anomaly at temperatures below $T_c(H=0)$. On the other hand, the ab-plane thermal conductivity for magnetic field oriented parallel to the ab-plane, $\kappa_{ab}(T,\mathbf{H}\perp c)$, exhibits only a small suppression of the anomaly below T_c.

High purity single crystals of $Bi_2Sr_2CaCu_2O_8$ were prepared by standard methods as described in section (1.2). The crystals were platelets of typical dimensions 2mm × 1mm × 0.01mm.

Figure 5.1 shows a typical ab-plane thermal conductivity and electric resistivity of the samples used in this study, in zero magnetic field. The electric resistivity exhibits a characteristic "metallic" behavior of the HTSC. The resistive transition is sharp with a midpoint T_c=85K and a width of ΔT_c<2K. The thermal conductivity decreases as temperature is decreased from room temperature down to ≈95K, where it shows a local minimum. On further cooling, κ_{ab} reaches a local maximum at T≈65K; below this temperature κ_{ab} decreases rapidly.

Two models have been proposed to explain the enhancement of the in-plane thermal conductivity below the transition temperature. First, a decrease in the phonon scattering due quasiparticle-condensation into Cooper pairs gives rise to an increase of the lattice thermal conductivity.[3,11] Second, a rapid decreased in the scattering of quasiparticles gives rise to an increase in the electronic thermal conductivity[5,6] producing a peak in the total thermal conductivity below T_c.

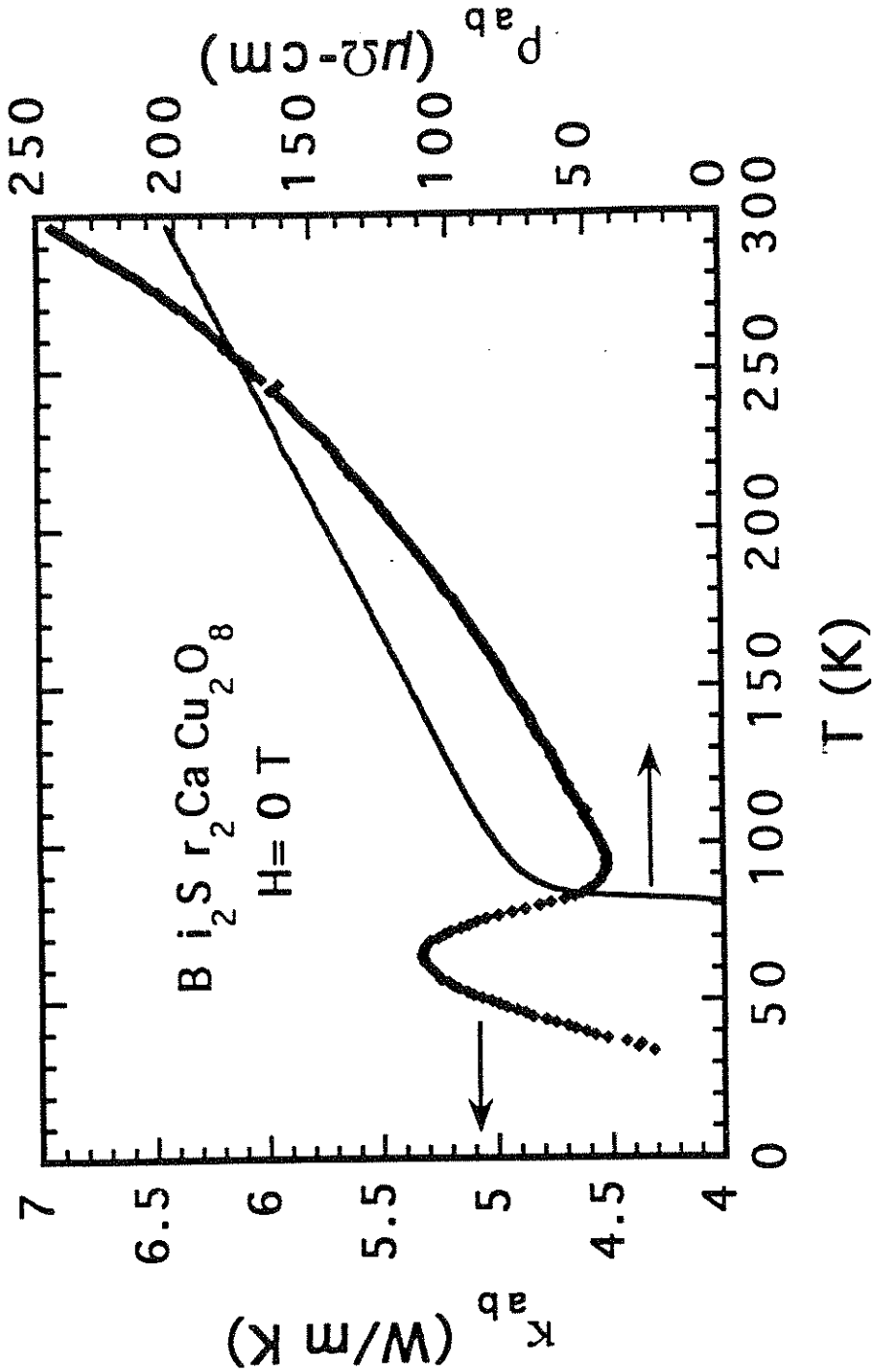

Figure 5.1 Thermal conductivity and electrical resistivity of single crystal $Bi_2Sr_2CaCu_2O_8$ in zero magnetic field.

We first apply the analysis used by S.D. Peacor *et al.*,[3] in the fitting their $YBa_2Cu_3O_7$ single crystal data. We assume the validity of the Wiedemann-Franz Law in the normal state and find that the electron contribution to the thermal conductivity above T_c is almost temperature independent, since $\sigma(T)\sim 1/T$. The κ_e contributes significantly ($\approx$65% at 100K) to the net thermal transport close to the transition temperature. Following Peacor's analysis, we can use the theory of Geĭlikman *et al.*,[12] and obtain the electron contribution to κ_{ab} in the superconducting state, allowing the extraction of the phonon thermal conductivity, $\kappa_p=\kappa_{ab}-\kappa_e$. To complete their analysis, we can essentially use the model of Teword and Wölkhausen[11] for s-wave pairing to fit the extracted lattice thermal conductivity, which according to the model is given by

$$\kappa_p = \frac{k_B}{2\pi^2 v}\left(\frac{k_B T}{\hbar}\right)^3 \int_0^{\Theta_D/T} dx \frac{x^4 e^x}{(e^x-1)^2} \int_0^1 d\zeta \frac{2}{3} \frac{(1-\zeta^2)}{\tau(T, x, \zeta)^{-1}} \qquad (5.5)$$

where $x=\hbar\omega/k_B T_c$, v is the sound velocity, Θ_D is the Debye temperature, and $\tau(T,x,\zeta)^{-1}$ is given by the expression

$$\tau(T, x, \zeta)^{-1} = B + D_p T^4 x^4 + D_{sf} T^2 x^2 + ETx\, g(x,y) + UT^4 x^2 \qquad (5.6)$$

where the coefficients represent the various phonon scattering mechanisms present in the layered superconductors:

B: Boundary scattering, =v/(smallest sample dimension),

D_p: Scattering by point defects,

D_{sf}: Scattering by stacking faults,

E: Scattering by electrons,

U: Phonon umklapp scattering,

and the function g(x, y) is the ratio of the phonon electron scattering times in the normal and the superconducting states, i.e., $g(x, y) = \tau_{n,pe}/\tau_{s,pe}$, and $y = \Delta(T)/K_BT$ is the reduced energy gap. Expressions for g(x, y) have been found by Bardeen, Rickayzen and Teword.[13] The integral over $\zeta=\cos\theta$, where θ is the polar angle with respect to the c-axis, is to take into account the anisotropy of the electron-phonon interaction and momentum conservation in the ab-plane.

A least squares fit program described in appendix A was used to fit the data of Fig. (5.1) with v=2850m/s and Θ_D=270K (Ref. 14, 15).

Such a fit is shown in Fig. 5.2 by a solid line. The value of the free parameters obtained from the best fit are:

$B=2.85\ (10^8)\ sec^{-1}$.

$D_p=2.30\ (10^4)\ K^{-4}sec^{-1}$.

$D_{sf}=1.03\ (10^5)\ K^{-2}sec^{-1}$.

$E=5.14\ (10^9)\ K^{-1}sec^{-1}$.

The parameter U was set equal to zero because it acquired negative values, which is unphysical. In an attempt to improve the fit, κ_e in the normal state and the ratio of the energy gap in the material to the BCS energy gap $\chi=(\Delta_{HTSC}/\Delta_{BCS})$, in the superconducting state, were also treated as free parameters. Their optimal values are:

$\kappa_e=3.67$ W/m K.

$\chi=1.57$.

Several discrepancies between the data and the fit are immediately obvious: (i) the fit hardly decreases in the normal state, while the data decreases by about 13% from 225K to 95K. (ii) The curvature of the data and the fit are of opposite sign in the normal state. (iii) Finally, the fit exhibits a sharp jump at the transition temperature, while the data

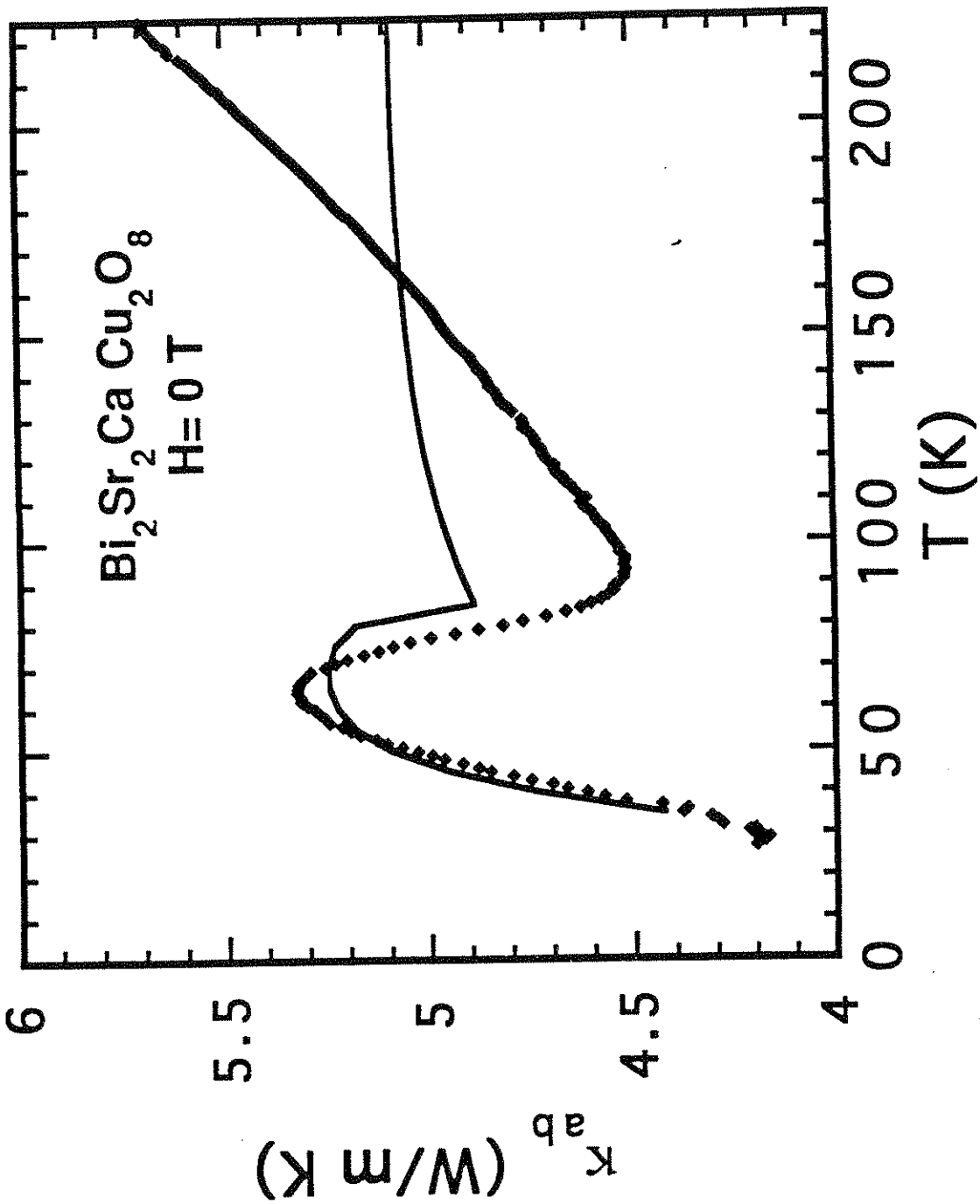

Figure 5.2 Thermal conductivity data from Fig. 5.1 in a reduced temperature range and the theoretical curve (solid line) from the model of Teword and Wölkhausen (see text).

smoothly turns up as the temperature is decreased. This model does not fit our data very well.

We now turn to the model proposed by R. C. Yu *et al.*[5]. They fit their normal state thermal conductivity along the a-axis data of a $YBa_2Cu_3O_7$ single crystal to the expression

$$\kappa_a^n = \kappa_{e,a}^n + 1/(W_o + \alpha T) \tag{5.7}$$

where they assume the validity of the Wiedemann-Franz law, i.e., the electron thermal conductivity is constant since $\sigma \sim 1/T$, and that the most significant scattering mechanism for the phonon thermal conductivity at high temperatures is the umklapp process for which $\tau_U^{-1} \sim T$ (Ref. 16). Unfortunately, Eq. (5.7) is a decreasing function of temperature and cannot fit our data, which is an increasing function of temperature.

Both of the two above analyses fail to provide a reliable method to interpret our data or to separate the electron and the phonon contributions to the total thermal conductivity of $Bi_2Sr_2CaCu_2O_8$.

An alternative approach to discern the κ_p from the total thermal conductivity is to introduce in a controlled manner a phonon scatterer which does not affect the electron part of κ_{ab}, or vice versa. The mean free path of the long wavelength phonons, which are mostly responsible for κ_p, is $l_{mfp,p} \sim 5\mu m$ (Ref. 17). We can estimate the mean free path of the electron by using $\tau_{e\text{-}ph} = 0.62\times10^{-12}(m^*/m)T^{-1}$ (sec·K) from section (3.3), and by assuming a half-filled conduction band we get $v_F \approx 4\times10^{-25}/m^*$ (Kg m/sec), which yields $l_{mfp,e} \approx 2.7\times10^{-7}/T$ (m °K), i.e., $l_{mfp,e} \approx 27$Å at 100K. Since the distance between vortices in the mixed state for a c-axis oriented magnetic field of 1Tesla is ≈450Å, larger than the in-plane $l_{mfp,e}$, we believe the vortices are strong phonon scatterers which leaves the electrons essentially unperturbed.

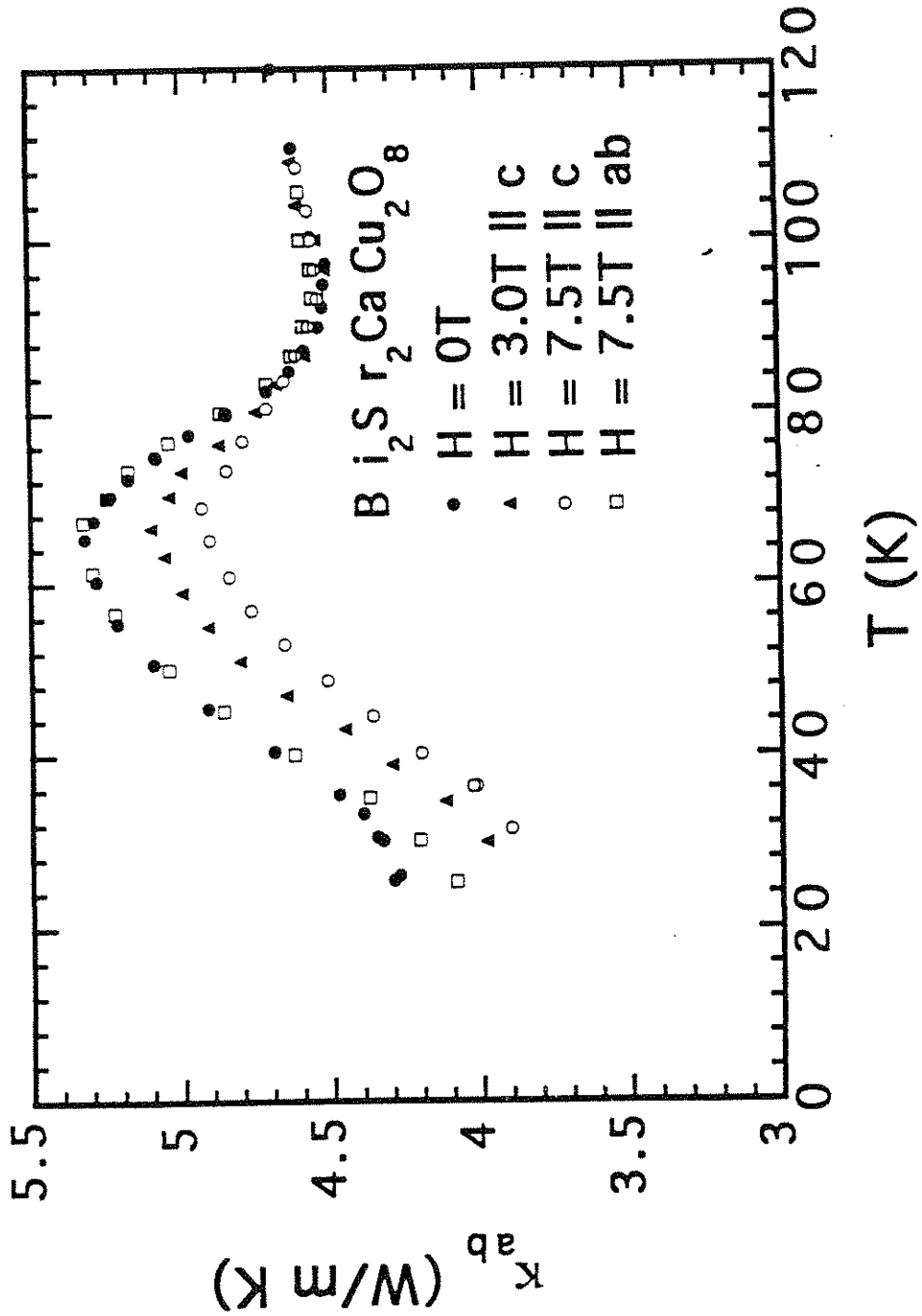

Figure 5.3 The ab-plane thermal conductivity of single crystal $Bi_2Sr_2CaCu_2O_8$ for three magnetic fields parallel to the c-axis (0, 3, and 7.5 T) and two magnetic fields perpendicular to the c-axis (0, 7.5T).

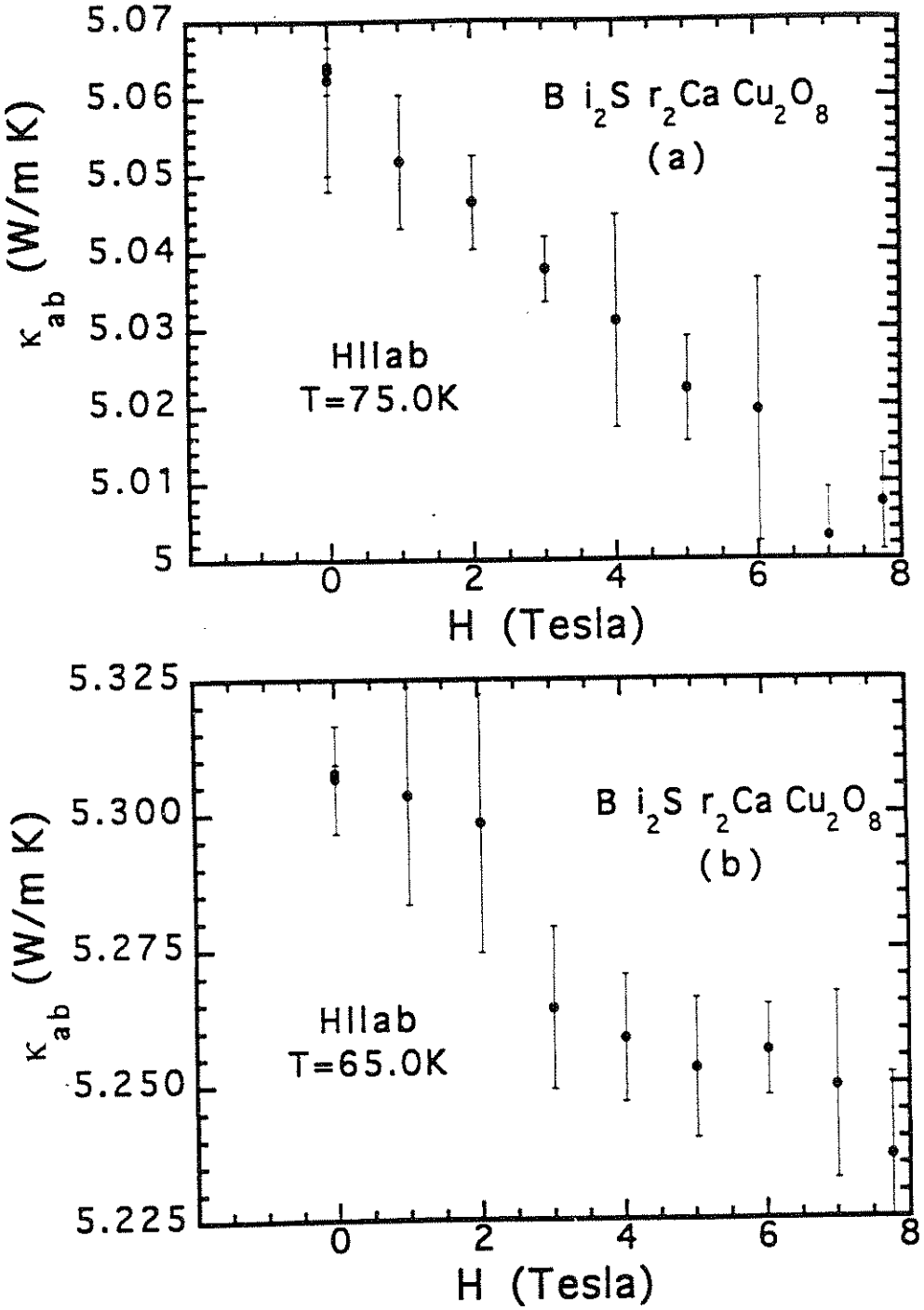

Figure 5.4 Field dependence of the ab-plane termal coductivity at two temperatures: (a) 75.0K, and (b) 65.0K. The magnetic field was oriented perpendicular to the c-axis.

In Fig. 5.3 we show $\kappa_{ab}(T,\mathbf{H})$ for a $Bi_2Sr_2CaCu_2O_8$ crystal for selected magnetic fields 0T, 3.T and 7.5T oriented parallel to the c-axis, and 7.5T oriented perpendicular to the c-axis. In the normal state the application of a magnetic field has no effect on $\kappa_{ab}=\kappa_{ab}(T>T_c, \mathbf{H=0})$. However, in the superconducting state the thermal conductivity peak is reduced by a ≈10% on the application of a 7.5T magnetic field parallel to the c-axis, but no apparent reduction is observed when the same magnetic field is applied perpendicular to the c-axis. Upon a more careful measurement at a fixed temperature $T<T_c$, a small reduction (≈1%) of the peak in κ_{ab} is observed for a 7.5T magnetic field $\mathbf{H}\|\mathbf{c}$, as shown in Fig. 5.4, smaller than the same effect in $YBa_2Cu_3O_7$ (≈6%, Ref. 10). This is qualitatively consistent with the suggestion of Theodorakis *et al.*,[18] that a magnetic field parallel to ab-plane produces Josephson vortices between the superconducting CuO_2 bilayers in $Bi_2Sr_2CaCu_2O_8$ with almost no effect on the in-plane transport properties.

Figure 5.5 shows $\kappa_{ab}(T,\mathbf{H})$ for selected fixed temperatures and $\mathbf{H}\perp\mathbf{c}$. The solid lines are fits to the expression:

$$\kappa_{ab}(H) = \kappa_1 + 1/[(1/\kappa_2) + A\,H] \qquad (5.8)$$

where κ_1, κ_2 and A are the free parameters to the fits, and we have assumed that κ_{ab} is the sum of only two components, one of them, $1/[(1/\kappa_2) + AH]$, having a magnetic field dependence with a thermal resistance that increases in proportion to the density of vortices. Equation (5.8) describes the data extremely well. The values extracted for the parameters at the different temperatures are given in Table 5.1, and plotted in Fig. 5.6.

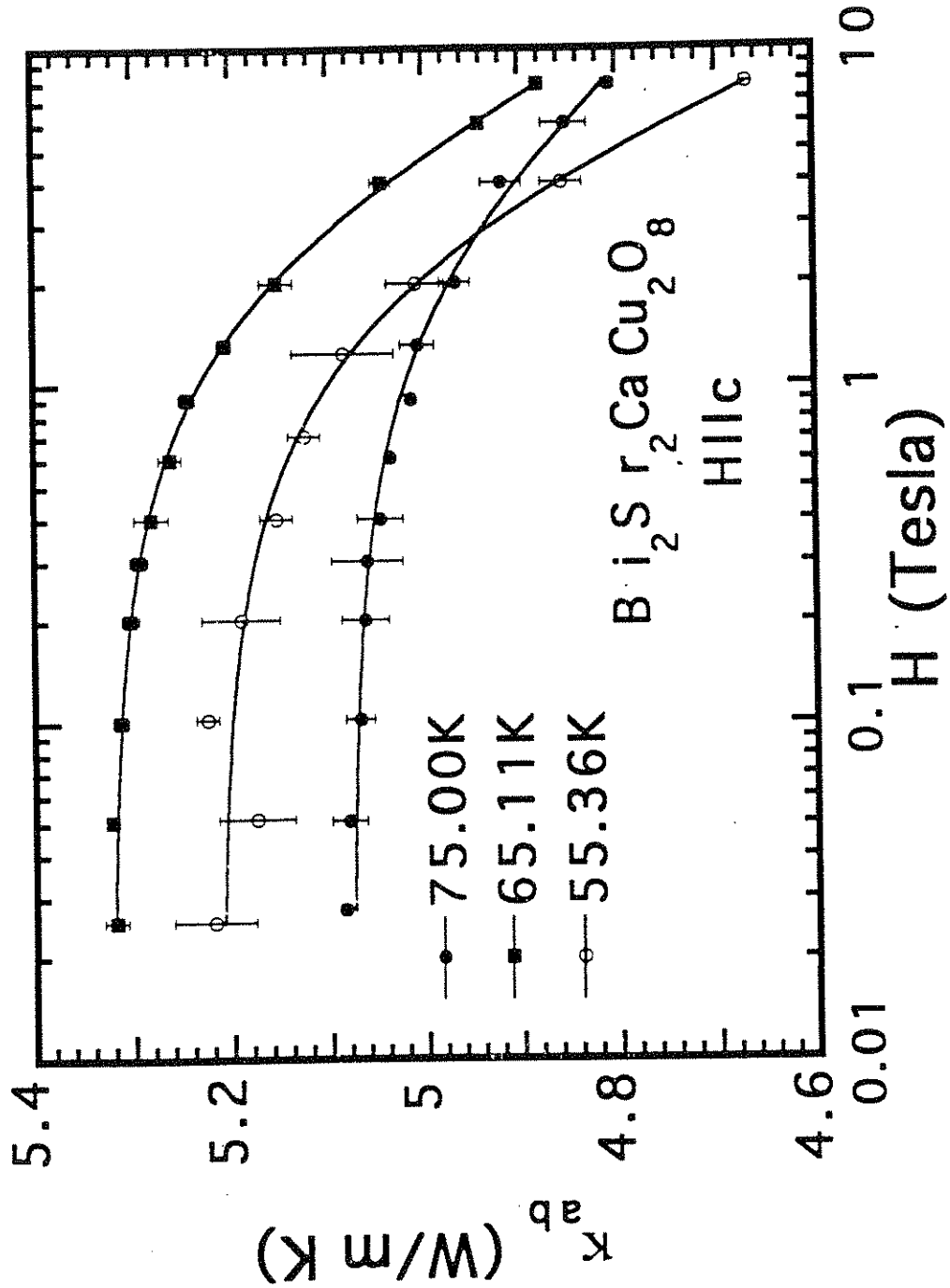

Figure 5.5 Thermal conductivity dependence on a magnetic field oriented parallel to the c-axis at three fixed temperatures. The solid lines are fits to Eq. (5.8) with the coefficients given in Table 5.1.

Temperature (K):	κ_1 (W/K m):	κ_2 (W/K m):	A (K m/W T):
75.00	4.52	0.56	20.2 (10^{-2})
65.11	4.28	1.04	9.11 (10^{-2})
55.36	3.95	1.25	7.75 (10^{-2})

Table 5.1. Coefficients of Eq. (5.8) used to fit the magnetic field dependence of the thermal conductivity, as shown in Fig. 5.5.

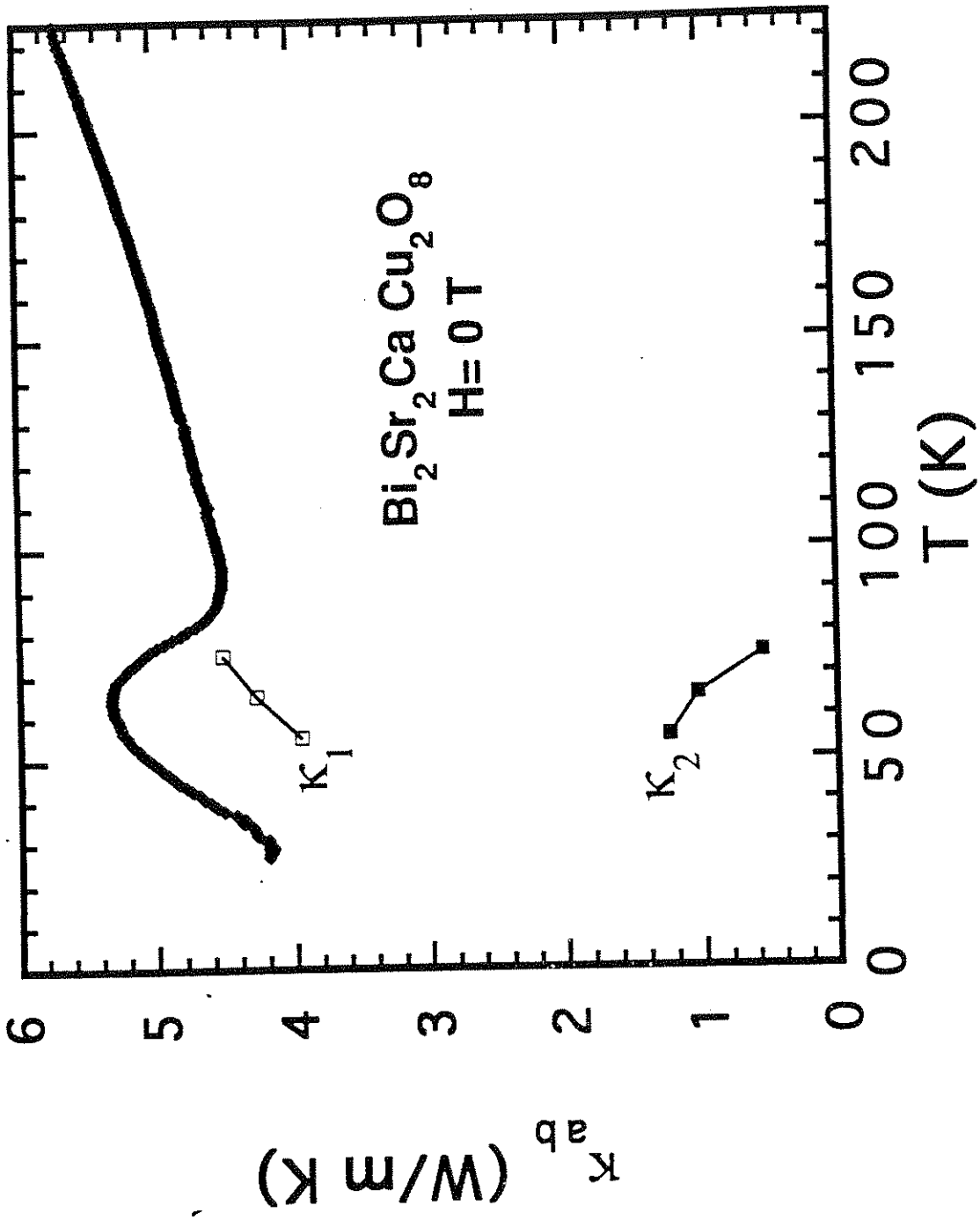

Figure 5.6 Thermal conductivity data from Fig. 5.2 and the parameters κ_1 and κ_2 from the fits of the data of Fig. 5.5 to Eq. (5.8). The solid lines are guides to the eye.

We now identify κ_1 and κ_2 with the electron and phonon components of κ_{ab} reapectively. The values of $\kappa_e=\kappa_1$ obtained for different temperatures indicate that it develops a maximum close to T_c (=85K) as the temperature is increased, since it is an increaisng function of temperature in the 55K<T<75K temperature range and $\kappa_e(75K)=\kappa_{ab}(95K, H=0)$, the local minimum of $\kappa_{ab}(H=0)$. This also suggests that the electrons probably dominate the heat conduction process in the normal state close to T_c, where the validity of the Wiedemann-Franz law is questionable since Θ_D=270K for $Bi_2Sr_2CaCu_2O_8$. The presence of a local maximum in κ_e below T_c is qualitatively consistent with the experimental observation that the quasiparticle scattering is rapidly suppressed below Tc [19,20] giving rise to an increase in κ_e.

However, the increase in $\kappa_p(H=0)=\kappa_2$ as the temperature is lowered also indicates that it reaches a maximum below the transition temperature, at some temperature T<55K, contributing to the peak in κ_{ab}. The sharp decrease in $\kappa_{ph}(H=0)$ as the transition temperature is approached from below can be interpreted as an almost null contribution of the phonons to the thermal conductivity of $Bi_2Sr_2CaCu_2O_8$ in the normal state.

In conclusion, we suggest that both the electron and the phonon abilities to carry entropy are responsible for the large anomaly in the ab-plane thermal conductivity of $Bi_2Sr_2CaCu_2O_8$, with the phonons as the dominant contributors. The phonon thermal conductivity exhibits a sharp increase, from a negligible contribution in the normal state, as the temperature is lowered below T_c, due to the quasiparticle condensation into Cooper pairs. While the electron thermal conductivity exhibits only a relatively small peak below T_c, in accord with a diminution of the quasiparticle scattering below the transition temperature.

References:

1. J. K. Hulm, Proc. Roy. Soc. (London) **A204**, 98 (1950).
2. J. L. Olsen, Proc. Phys. Soc. **A65**, 518 (1952).
3. S. D. Peacor, R. A. Richardson, F. Nori, *et al.*, Phys. Rev. B **44**, 9508 (1991).
4. M. F. Crommie and A. Zettl, Phys. Rev. B **41**, 10978 (1990).
5. R. C. Yu, M. B. Salomon, J. P. Lu, *et al.*, Phys. Rev. Letters **69**, 1431 (1992).
6. P. B. Allen, X. Du, L. Mihaly, *et al.*, (preprint) , (1994).
7. A. Matthiessen, Rep. Br. Ass. **32**, 144 (1862).
8. M. F. Crommie, Ph. D., U. C. Berkeley (1991).
9. N. V. Zavaritsky and e. al, Physica C **180**, 417 (1991).
10. S. D. Peacor, J. L. Cohn and C. Uher, Phys. Rev. B **43**, 8721 (1991).
11. L. Teword and T. Wölkhausen, Solid. State Comm. **75**, 515 (1990).
12. B. T. Geĭlikman, M. I. Dushenat and V. R. Chechetkin, Sov. Phys. JETP **46**, 1213 (1977).
13. J. Bardeen, G. Rickayzen and L. Teword, Phys. Rev. **113**, 982 (1959).
14. Y. He, J. Xiang, S. Jin, *et al.*, Physica B **165-166**, 1283 (1990).
15. H. Ledbetter, S. Kim and K. Togano, Physica C **185-189**, 935 (1991).
16. J. M. Ziman, *Electrons and Phonons* (Clarendon, Oxford, 1963).
17. C. Uher, *Phys. Properties of HTSC III*, D. M. Ginsberg, Eds. (World Scientific, Singapore, 1992), vol. III.
18. S. Theodorakis, Phys. Rev. B **42**, 10172 (1990).
19. D. B. Romero, C. D. Porter, D. B. Tanner, *et al.*, Phys. Rev. Letters **68**, 1590 (1992).

20. D. A. Bonn, P. Dosanjh, R. Liang, *et al.*, Phys. Rev. Letters **68**, 2390 (1992).

Appendix A

Thermal Conductivity Fitting Program

This appendix consists of the text of a program to fit the thermal conductivity data of $Bi_2Sr_2CaCu_2O_8$ from Fig. 5.1 to the model of Teword and Wölkhausen[1] used by Peacor *et al.*,[2] to fit their $YBa_2Cu_3O_7$ data. The program is written in ThinkPascal 4.0, for use on a Macintosh personal computer.

```
program ThermalKab;
  uses
    sane;
  label
    2;
  const
    CGOLD = 0.38196611;
    Tc = 85.0;
    N = 0;
    Xexp = 2;
    Texp = 4;

  var
    LOOPFLAG: BOOLEAN;
    gbsfile: TEXT;
    pr, aname, afile: Str255;
    X0, X1, X2, X3, AX, BX, CX, F0, F1, F2, F3: EXTENDED;
    X, Y, Z, Tt, TH, SZ, Vs, TD, B0, Bb, lambda: extended;
    ChiSqr, A0, A1, A2, A3, A4, A5, A6, Kab, Kba, TrD: extended;
    TSmpl, KBSCCO: array[1..40] of extended;
    V1, V2, DV1, nV1, V5: array[1..6] of extended;
    UGauss, WGauss: array[1..16] of extended;
```

```
    ICount: Integer;

  procedure Initialize;
  begin
{Initializing the array of the QGaussInt function}
    UGauss[1] := 0.0483076656877;
    UGauss[2] := 0.1444719615828;
    UGauss[3] := 0.2392873622521;
    UGauss[4] := 0.3318686022821;
    UGauss[5] := 0.4213512761306;
    UGauss[6] := 0.5068999089322;
    UGauss[7] := 0.5877157572408;
    UGauss[8] := 0.6630442669302;
    UGauss[9] := 0.7321821187403;
    UGauss[10] := 0.7944837959679;
    UGauss[11] := 0.8493676137326;
    UGauss[12] := 0.8963211557661;
    UGauss[13] := 0.9349060759377;
    UGauss[14] := 0.9647622555875;
    UGauss[15] := 0.9856115115453;
    UGauss[16] := 0.9972638618495;

    WGauss[1] := 0.0965400885147;
    WGauss[2] := 0.0956387200793;
    WGauss[3] := 0.0938443990808;
    WGauss[4] := 0.0911738786958;
    WGauss[5] := 0.0876520930044;
    WGauss[6] := 0.0833119242269;
    WGauss[7] := 0.0781938957871;
    WGauss[8] := 0.0723457941088;
    WGauss[9] := 0.0658222227764;
    WGauss[10] := 0.0586840934785;
    WGauss[11] := 0.0509980592624;
    WGauss[12] := 0.0428358980222;
```

```
WGauss[13] := 0.0342738629130;
WGauss[14] := 0.0253920653093;
WGauss[15] := 0.0162743947309;
WGauss[16] := 0.0070186100095;

{Initializing the array of datapoints}

TSmpl[1] := 230;
TSmpl[2] := 225;
TSmpl[3] := 220;
TSmpl[4] := 215;
TSmpl[5] := 210;
TSmpl[6] := 205;
TSmpl[7] := 200;
TSmpl[8] := 195;
TSmpl[9] := 190;
TSmpl[10] := 185;
TSmpl[11] := 180;
TSmpl[12] := 175;
TSmpl[13] := 170;
TSmpl[14] := 165;
TSmpl[15] := 160;
TSmpl[16] := 155;
TSmpl[17] := 150;
TSmpl[18] := 145;
TSmpl[19] := 140;
TSmpl[20] := 135;
TSmpl[21] := 130;
TSmpl[22] := 125;
TSmpl[23] := 120;
TSmpl[24] := 115;
TSmpl[25] := 110;
TSmpl[26] := 105;
TSmpl[27] := 100;
```

```
TSmpl[28] := 95;
TSmpl[29] := 90;
TSmpl[30] := 85;
TSmpl[31] := 80;
TSmpl[32] := 75;
TSmpl[33] := 70;
TSmpl[34] := 65;
TSmpl[35] := 60;
TSmpl[36] := 55;
TSmpl[37] := 50;
TSmpl[38] := 45;
TSmpl[39] := 40;
TSmpl[40] := 35;

KBSCCO[40] := 4.3516;
KBSCCO[39] := 4.6223;
KBSCCO[38] := 4.8544;
KBSCCO[37] := 5.0407;
KBSCCO[36] := 5.1987;
KBSCCO[35] := 5.2884;
KBSCCO[34] := 5.3215;
KBSCCO[33] := 5.2584;
KBSCCO[32] := 5.0843;
KBSCCO[31] := 4.8243;
KBSCCO[30] := 4.6062;
KBSCCO[29] := 4.5370;
KBSCCO[28] := 4.5215;
KBSCCO[27] := 4.5485;
KBSCCO[26] := 4.5863;
KBSCCO[25] := 4.6178;
KBSCCO[24] := 4.6672;
KBSCCO[23] := 4.7040;
KBSCCO[22] := 4.7397;
KBSCCO[21] := 4.7726;
```

```
    KBSCCO[20] := 4.8243;
    KBSCCO[19] := 4.8564;
    KBSCCO[18] := 4.8967;
    KBSCCO[17] := 4.9458;
    KBSCCO[16] := 4.9795;
    KBSCCO[15] := 5.0207;
    KBSCCO[14] := 5.0674;
    KBSCCO[13] := 5.1138;
    KBSCCO[12] := 5.1578;
    KBSCCO[11] := 5.2143;
    KBSCCO[10] := 5.2594;
    KBSCCO[9] := 5.3098;
    KBSCCO[8] := 5.3640;
    KBSCCO[7] := 5.4203;
    KBSCCO[6] := 5.4759;
    KBSCCO[5] := 5.5290;
    KBSCCO[4] := 5.5892;
    KBSCCO[3] := 5.6500;
    KBSCCO[2] := 5.6985;
    KBSCCO[1] := 5.7620;

end;{Initializing procedure}

function BessI0 (BessI0x: extended): extended;
    var
        BessI0i: integer;
        BessI0y, BessI0z, BessI0w: extended;
        BessI0P: array[1..7] of extended;
        BessI0Q: array[1..9] of extended;
begin
    BessI0P[1] := 1.0;
    BessI0P[2] := 3.5156229;
    BessI0P[3] := 3.0899424;
    BessI0P[4] := 1.2067492;
```

```
    BessI0P[5] := 0.2659732;
    BessI0P[6] := 0.360768E-1;
    BessI0P[7] := 0.45813E-2;
    BessI0Q[1] := 0.39894228;
    BessI0Q[2] := 0.1328592e-1;
    BessI0Q[3] := 0.225319e-2;
    BessI0Q[4] := -0.157565e-2;
    BessI0Q[5] := 0.916281e-2;
    BessI0Q[6] := -0.2057706e-1;
    BessI0Q[7] := 0.2635537e-1;
    BessI0Q[8] := -0.1647633e-1;
    BessI0Q[9] := 0.392377E-2;
    if abs(x) < 3.75 then
       begin
          BessI0y := BessI0x * BessI0x / (3.75 * 3.75);
          BessI0z := BessI0P[7];
          for BessI0i := 6 downto 1 do
             BessI0z := BessI0P[BessI0i] + BessI0y * BessI0z;
       end
    else
       begin
          BessI0z := ABS(BessI0x);
          BessI0y := 3.75 / BessI0z;
          BessI0w := BessI0Q[9];
          for BessI0i := 8 downto 1 do
             BessI0w := BessI0Q[BessI0i] + BessI0y * BessI0w;
          BessI0z := (EXP(BessI0z) / SQRT(BessI0z)) * BessI0w;
       end;
    BessI0 := BessI0z;
end;              {End of function BessI0}

function BessI1 (x: extended): extended;
    var
       i: integer;
```

```
        y, z, w: extended;
        P: array[1..7] of extended;
        Q: array[1..9] of extended;
begin
    P[1] := 0.5:
    P[2] := 0.87890594;
    P[3] := 0.51498869;
    P[4] := 0.15084934;
    P[5] := 0.2658733e-1;
    P[6] := 0.301532e-2;
    P[7] := 0.32411e-3;

    Q[1] := 0.39894228;
    Q[2] := -0.3988024e-1;
    Q[3] := -0.362018e-2;
    Q[4] := 0.163801e-2;
    Q[5] := -0.1031555e-1;
    Q[6] := 0.2282967e-1;
    Q[7] := -0.2895312e-1;
    Q[8] := 0.1787654e-1;
    Q[9] := -0.420059e-2;
    if abs(x) < 3.75 then
        begin
            y := x * x / (3.75 * 3.75);
            z := P[7];
            for i := 6 downto 1 do
                z := P[i] + y * z;
            z := z * x;
        end
    else
        begin
            z := ABS(x);
            y := 3.75 / z;
            w := Q[9];
```

```
            for i := 8 downto 1 do
                w := Q[i] + y * w;
            z := (EXP(z) / SQRT(z)) * w;
        end;
    Bessl1 := z;
    if x < 0 then
        Bessl1 := -z;
end;                {End of function Bessl1}

function BessK0 (x: extended): extended;
    var
        i: integer;
        y, z, w: extended;
        P: array[1..7] of extended;
        Q: array[1..7] of extended;
begin
    P[1] := -0.57721566;
    P[2] := 0.42278420;
    P[3] := 0.23069756;
    P[4] := 0.3488590e-1;
    P[5] := 0.262698e-2;
    P[6] := 0.10750e-3;
    P[7] := 0.74e-5;

    Q[1] := 1.25331414;
    Q[2] := -0.7832358e-1;
    Q[3] := 0.2189568e-1;
    Q[4] := -0.1062446e-1;
    Q[5] := 0.587872e-2;
    Q[6] := -0.251540e-2;
    Q[7] := 0.53208e-3;

    if abs(x) < 2.0 then
        begin
```

```
            y := x * x / 4.0;
            z := P[7];
            for i := 6 downto 1 do
                z := P[i] + y * z;
            z := -ln(x / 2.0) * Bessi0(x) + z;
        end
    else
        begin
            y := 2.0 / x;
            w := Q[7];
            for i := 6 downto 1 do
                w := Q[i] + y * w;
            z := (EXP(-x) / SQRT(x)) * w;
        end;
    BessK0 := z;
end;                {End of function BessK0}

function BessK1 (x: extended): extended;
    var
        i: integer;
        y, z, w: extended;
        P: array[1..7] of extended;
        Q: array[1..7] of extended;
begin
    P[1] := 0.9999999998;
    P[2] := 0.15443134078;
    P[3] := -0.6727845186;
    P[4] := -0.18157402054;
    P[5] := -0.19185581929e-1;
    P[6] := -0.11102404225e-2;
    P[7] := -0.4521524044e-4;

    Q[1] := 1.2533166858;
    Q[2] := 0.23494844745;
```

```
    Q[3] := -0.36344099165e-1;
    Q[4] := 0.14454586743e-1;
    Q[5] := -0.69446915607e-2;
    Q[6] := 0.26240997971e-2;
    Q[7] := -0.4980670495e-3;

    if x < 2.0 then
       begin
          y := x * x / 4.0;
          z := P[7];
          for i := 6 downto 1 do
             z := P[i] + y * z;
          z := (ln(x / 2.0) * Bessl1(x)) + (z / x);
       end
    else
       begin
          y := 2.0 / x;
          w := Q[7];
          for i := 6 downto 1 do
             w := Q[i] + y * w;
          z := (EXP(-x) / SQRT(x)) * w;
       end;
    BessK1 := z;
end;              {End of function BessK1}

function GAP (Z: extended): extended;
    var
       diff, width, tx, temp: extended;
       RDG: array[1..42] of extended;
       I: integer;
       P: array[0..10] of extended;
begin
    if Z >= 1.0 then
       begin
```

```
        GAP := 0.0;
        EXIT(GAP);
    end;
RDG[1] := 0.0;
RDG[2] := 0.2436;
RDG[3] := 0.3416;
RDG[4] := 0.4148;
RDG[5] := 0.4749;
RDG[6] := 0.5263;
RDG[7] := 0.5715;
RDG[8] := 0.6117;
RDG[9] := 0.648;
RDG[10] := 0.681;
RDG[11] := 0.711;
RDG[12] := 0.7386;
RDG[13] := 0.764;
RDG[14] := 0.7874;
RDG[15] := 0.8089;
RDG[16] := 0.8288;
RDG[17] := 0.8471;
RDG[18] := 0.864;
RDG[19] := 0.8796;
RDG[20] := 0.8939;
RDG[21] := 0.907;
RDG[22] := 0.919;
RDG[23] := 0.9299;
RDG[24] := 0.9399;
RDG[25] := 0.9488;
RDG[26] := 0.9569;
RDG[27] := 0.9641;
RDG[28] := 0.9704;
RDG[29] := 0.976;
RDG[30] := 0.9809;
RDG[31] := 0.985;
```

```
RDG[32] := 0.9885;
RDG[33] := 0.9915;
RDG[34] := 0.9938;
RDG[35] := 0.9957;
RDG[36] := 0.9971;
RDG[37] := 0.9982;
RDG[38] := 0.9989;
RDG[39] := 0.9994;
RDG[40] := 0.9997;
RDG[41] := 0.9999;
RDG[42] := 1.0;

P[0] := 151.20204;
P[1] := -1552.0409;
P[2] := 7032.04262;
P[3] := -16913.18153;
P[4] := 19879.75009;
P[5] := 1' 30.52161;
P[6] := -39626.35396;
P[7] := 61357.78193;
P[8] := -47421.88649;
P[9] := 19451.47402;
P[10] := -3389.07601;
temp := 0;
if Z <= 0.18 then
    GAP := 1.76 / z
else if (z >= 0.974) & (z < 1) then
    GAP := (3.06 / Z) * SQRT(1 - Z)
else if (z >= 0.5) & (z < 0.974) then
    begin
        TEMP := 0;
        for i := 0 to 10 do
            TEMP := TEMP + P[i] * Xpwrl(z, i);
        GAP := TEMP;
```

```
      end
   else if (z < 0.5) & (z > 0.18) then
      begin
         TX := (1.02 - Z) / 0.02;
         I := Trunc(TX);
         WIDTH := RDG[I + 1] - RDG[I];
         DIFF := Z - (1.02 - (I + 1) * 0.02);
         GAP := (RDG[I + 1] - DIFF * WIDTH / 0.02) * 1.76 / Z;
      end
end;              {End of function GAP}

function CEL (QQC, PP, AA, BB: extended): extended;
   label
      1;
   const
      CA = 0.0003;
      Pi2 = 1.57079632679489661923132169163 9;
   var
      a, b, p, e, em, q, qc, g, pi, f: extended;
begin
   QC := ABS(QQC);
   A := AA;
   B := BB;
   P := PP;
   E := QC;
   EM := 1.0;
   if P > 0 then
      begin
         P := sqrt(p);
         B := B / P;
      end
   else
      begin
         F := QC * QC;
```

```
            Q := 1 - F;
            G := 1 - P;
            F := F - P;
            Q := Q * (B - A * P);
            P := SQRT(F / G);
            A := (A - B) / G;
            B := -Q / (G * G * P) + A * P;
          end;
1:
        F := A;
        A := A + B / P;
        G := E / P;
        B := B + F * G;
        B := B + B;
        P := G + P;
        G := EM;
        EM := QC + EM;
        if (ABS(G - QC) > (G * CA)) then
           begin
              QC := SQRT(E);
              qc := qc + qc;
              E := QC * EM;
              goto 1;
    end;
        CEL := PI2 * (B + A * EM) / (EM * (EM + P));
     end;              {End of function CEL}


     function FERMI (X: extended): extended;
     begin
        Fermi := 1 / (EXP1(X) + 2);
     end;
```

```
function QGaussInt (A, B: extended; function afunc (anumber: extended):
extended; ACC: extended): extended;
    var
        M, K, J, I: integer;
        Q, Q2, A0, X, X0, X5, X6, SS, SS0, ERR: extended;
  begin
    M := 1;
    Q := (B - A) / M;
    Q2 := Q / 2;
    K := 0;
    M := M + M; {--------Evaluating  for M=2}
    Q := Q2;
    Q2 := Q / 2;
    repeat
      begin
        SS := 0;
        A0 := -Q2 + A;
        for I := 1 to M do
          begin
            X0 := Q * I;
            for J := 1 to 16 do
              begin
                X := Q2 * UGauss[J];
                X5 := A0 + X0 + X;
                X6 := A0 + X0 - X;
                SS := SS + WGauss[J] * (aFUNC(X5) + aFUNC(X6));
              end;
          end;
        SS := Q2 * SS;
        QGaussInt := SS;
        exit(QGaussInt);  {--Exiting QGauss without evaluating the error}

(* TEST ACCURACY OF INTEGRATION BY DOUBLING # SUBINTERVALS *)
                                    {OPTIONAL}
```

```
            if K >= 0 then
               begin
                  if K >= 4 then
                     leave;
                  ERR := ABS((SS - SS0) / SS);
                  if ERR < ACC then
                     leave;
                  K := K + 1;
                  SS0 := SS;
                  M := M + M;
                  Q := Q2;
                  Q2 := Q / 2;
               end;
         end;
      until false;
      QGaussInt := SS;
   end;                              {End of function QGaussInt}

   function TherCond (SZ, A1, A2, A3, A4, A5, A6, TT: extended): extended;
      const
         ACC = 1e-2;

      function Tegrand (X: extended): extended;
         var
            XX, SS: extended;

         function Gxy: extended; {-This is the begining of G(x=hv/kT,
y=Δ(T)/kT)}
            var
               A, P, EE, EP, F1, F2, B1: extended;;

            function GRAND1 (A: extended;): extended;;
            begin
```

```
            P := A + X;  {--X is the "u", A is the "E", and P is "E' " in the BRT
paper}
            EE := SQRT(A * A - Y * Y);
            EP := SQRT(P * P - Y * Y);
            GRAND1 := (EE / EP + A * X / (EE * EP)) * Fermi(A) * Fermi(-P);
         end;

         function GRAND2 (A: extended;): extended;;
         begin
            P := A + X;
            EE := SQRT(A * A - Y * Y);
            EP := SQRT(P * P - Y * Y);
            GRAND2 := ABS(A * P / (EE * EP)) * (1 - Y * Y / (A * P)) *
Fermi(A) * Fermi(-P);
         end;

         function FN1 (X: extended): extended;
            var
               R1, R2, R3: extended;
         begin
            R1 := 2 * Y / (X + 2 * Y);
            R2 := (3 * X + 4 * Y) * X / (8 * Y * (X + 2 * Y));
            R3 := X / 2;
            FN1 := EXP(-Y) * SQRT(R1) * R3 * EXP(R3) * (BESSK1(R3) +
R2 * (BESSK1(R3) - BESSK0(R3)));
         end;

         function FN2 (X: extended): extended;
            var
               R1, R2, R3: extended;
         begin
            R1 := (X - 2 * Y) / (X + 2 * Y);
            R2 := SQRT(1 - R1 * R1);
            R3 := 0.5 * X + Y;
```

```
            if X <= 2 * Y then
                FN2 := 0.0
            else
                FN2 := 2 * (R3 * CEL(R2, 1, 1, R2 * R2) - (X * Y / R3) *
CEL(R2, 1, 1, 1));
  end;

        begin {--------------------Gxy-----------------------}
          if TrD >= 1 then
            begin
              Gxy := 1.0;
              EXIT(Gxy);
            end;
          if Y > 10 then
            begin
              Gxy := ((1 - EXP(-X)) / X) * (2 * FN1(X) + FN2(X));
              exit(Gxy);
            end;
          if 10 < (2.5 * Y) then
            B1 := 2.5 * Y
          else
            B1 := 10;
          F1 := QGaussInt(Y, B1, GRAND1, 0.01);
          F2 := 0.0;
          if X > (2 * Y) then
            F2 := QGaussInt(-X + Y, -Y, GRAND2, 0.01);
          Gxy := ((1 - EXP(-X)) / X) * (2 * F1 + F2);
        end;{--------------END OF Gxy FUNCTION---------------}

        function ANISO (Z: extended). extended;
          var
            D, D1: extended;

        begin {--------------------Aniso-----------------------}
```

```
            if X = 0 then
               D := SZ
            else if Z = 1 then
               begin
                  ANISO := 0;
                  exit(aniso);
               end
            else
               D := SZ + A1 * Xpwrl(TT * X, 4) + A2 * TT * TT * X * X + A3 * TT
* X * (XX * (1 - N) + N) * (1 - Z * Z) * SQRT(1 - Z * Z) + A4 * Xpwrl(TT, TEXP) *
Xpwrl(X, XEXP) * EXP(-TH / (BB * TT));
               {if D <= 0 then writeln('X=', x, ' Y = ', y, ' 1 / Tau = ', D);}
            ANISO := 1.5 * (1 - Z * Z) / D;
         end;{----------END OF Aniso FUNCTION----------}

      begin {----------Tegrand----------}
         XX := Gxy;
         SS := QGaussInt(0, 1, Aniso, ACC);
         TEGRAND := Xpwrl(X, 4) * EXP(X) / (EXP1(X) * EXP1(X)) * SS;
      end; {----------END OF Tegrand FUNCTION----------}

   begin
      TherCond := 0.0;
      if TrD < 1 then
         begin
            Kab := 0;
            Kba := 0;
            A0 := 0;
            Y := A6 * GAP(TrD);
            B0 := 2 * Y;
            if B0 > TD / TT then
               B0 := TD / TT;
            Kba := 1.5694721e9 * Xpwrl(TT, 3) * QGaussInt(A0, B0, Tegrand,
ACC) / Vs;
```

```
            A0 := 2 * Y;
            B0 := TD / TT;
            if A0 < B0 then
               Kab := 1.5694721e9 * Xpwrl(TT, 3) * QGaussInt(A0, B0,
Tegrand, ACC) / Vs;
            TherCond := A5 * TRD + Kba + Kab;
         end
      else
         TherCond := A5 + 1.5694721e9 * Xpwrl(TT, 3) * QGaussInt(0, TD /
TT, Tegrand, ACC) / Vs;
   end;{---------END OF TherCond FUNCTION----------}
```

```
        TrD := TT / Tc;
        Z := THERCOND(SZ, V1[1], V1[2], V1[3], V1[4], V1[5], V1[6], TT);
        writeln(gbsfile, TT : 20 : 12, chr(9), Z : 20 : 12);
        writeln('T=', TT : 10 : 5, 'Kab=', Z : 10 : 7);
        ChiSqr := ChiSqr + (Z - KBSCCO[Icount]) * (Z - KBSCCO[Icount]);
    end;
writeln('ChiSqr =', ChiSqr : 20);
close(gbsfile);

for Icount := 1 to 40 do
    begin
        TT := TSmpl[ICount];
        TrD := TT / Tc;
        Z := THERCOND(SZ, V2[1], V1[2], V1[3], V1[4], V1[5], V1[6], TT);
        DV1[1] := DV1[1] + (Z - KBSCCO[Icount]) * (Z - KBSCCO[Icount]);
    end;

for Icount := 1 to 40 do
    begin
        TT := TSmpl[ICount];
        TrD := TT / Tc;
        Z := THERCOND(SZ, V1[1], V2[2], V1[3], V1[4], V1[5], V1[6], TT);
        DV1[2] := DV1[2] + (Z - KBSCCO[Icount]) * (Z - KBSCCO[Icount]);
    end;

for Icount := 1 to 40 do
    begin
        TT := TSmpl[ICount];
        TrD := TT / Tc;
        Z := THERCOND(SZ, V1[1], V1[2], V2[3], V1[4], V1[5], V1[6], TT);
        DV1[3] := DV1[3] + (Z - KBSCCO[Icount]) * (Z - KBSCCO[Icount]);
    end;

            {DV1[1] := ChiSqr;}
```

```
                {DV1[2] := ChiSqr;}
    DV1[4] := ChiSqr;
    DV1[5] := ChiSqr;              {Not changing DV1[4,5,6] in this run}
    DV1[6] := ChiSqr;

    for Icount := 1 to 6 do
        nV1[Icount] := 1000 * (DV1[Icount] - ChiSqr);
    loopflag := False;

    repeat
        writeln('Value of X');
        readln(x);
        for Icount := 1 to 6 do
            V5[Icount] := V1[Icount] + X * nV1[Icount];
        ChiSqr := 0.0;
        for Icount := 1 to 40 do
            begin
                TT := TSmpl[ICount];
                TrD := TT / Tc;
                Z := THERCOND(SZ, V5[1], V5[2], V5[3], V5[4], V5[5], V5[6], TT);
                ChiSqr := ChiSqr + (Z - KBSCCO[Icount]) * (Z - KBSCCO[Icount]);
            end;
{writeln('Value of loopflag');}
{readln(x);}
        if x = 0 then
            loopflag := True;
        writeln('ChiSqr =', ChiSqr : 20, ' Lambda=', X : 20);
    until loopflag;

{writeln('value of lambda?');}
{read(lambda);}
{writeln('Value of AX');}
{readln(Ax);}                      {OPTIONAL}
{writeln('Value of BX');}
```

```
{readln(Bx);}
{writeln('Value of CX');}
{readln(Cx);}

        {----------BEGINS THE GOLDEN SEARCH SECTION----------}
   X0 := AX;
   X3 := CX;
   if ABS(CX - BX) > ABS(BX - AX) then
      begin
         X1 := BX;
         X2 := BX + CGOLD * (CX - BX);
      end
   else
      begin
         X2 := BX;
         X1 := BX - CGOLD * (BX - AX);
      end;
   F1 := FCHISQR(X1);
   F2 := FCHISQR(X2);
2:
   if ABS(X3 - X0) > (0.01 * (ABS(X1) + ABS(X2))) then
      begin
         if F2 < F1 then
            begin
               X0 := X1;
               X1 := X2;
               X2 := (1 - CGOLD) * X1 + CGOLD * X3;
               F0 := F1;
               F1 := F2;
               F2 := FCHISQR(X2);
            end
         else
            begin
               X3 := X2;
```

```
                X2 := X1;
                X1 := (1 - CGOLD) * X2 + CGOLD * X0;
                F3 := F2;
                F2 := F1;
                F1 := FCHISQR(X1);
             end;
          goto 2;
       end;
       if F1 < F2 then
       begin
          CHISQR := F1;
          LAMBDA := X1;
       end
    else
       begin
          CHISQR := F2;
          LAMBDA := X2;
       end; {------------------END OF GOLDEN SECTION SEARCH----------------}

    for Icount := 1 to 4 do
       V5[Icount] := V1[Icount] + LAMBDA * nV1[Icount];

    writeln('ChiSqr =', ChiSqr : 20, ' Lambda=', lambda : 20);
    writeln('A1 =', V5[1] : 20, ' A2=', V5[2] : 20);
    writeln('A3 =', V5[3] : 20, ' A4=', V5[4] : 20);
    writeln('A5 =', V5[5] : 20, ' A6=', V5[6] : 20);
end.
```

References:

1. L. Teword and T. Wölkhausen, Solid. State Comm. **75**, 515 (1990).

2. S. D. Peacor, R. A. Richardson, F. Nori, *et al.*, Phys. Rev. B **44**, 9508 (1991).